AD-A186 619   INTERACTION OF A VORTEX PAIR WITH A FREE SURFACE(U)   1/2
   NAVAL POSTGRADUATE SCHOOL MONTEREY CA   J ELNITSKY
   SEP 87

UNCLASSIFIED   F/G 20/4   NL
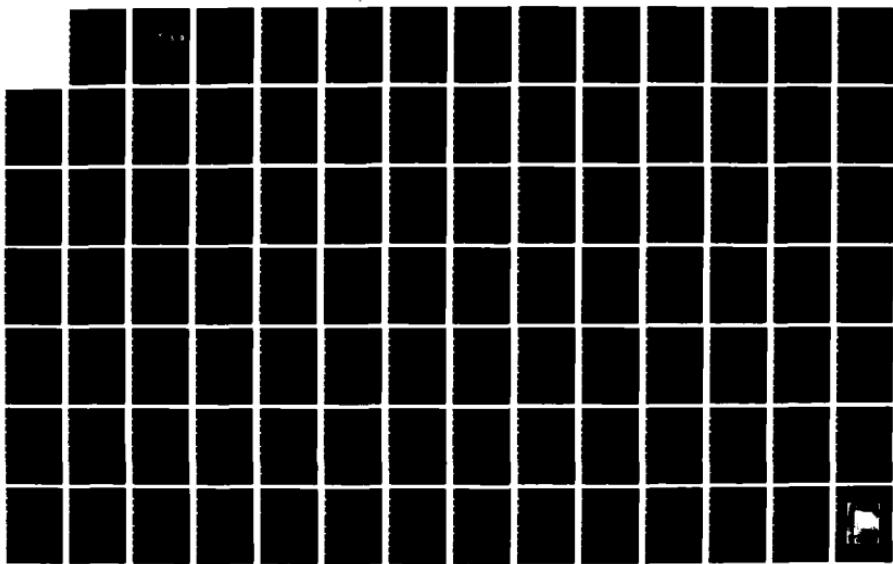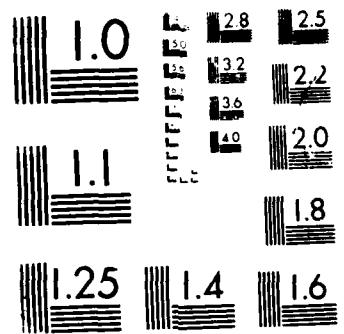
MICROCOPY RESOLUTION TEST CHART
NATIONAL BUREAU OF STANDARDS-1963

NAVAL POSTGRADUATE SCHOOL
Monterey, California

DTIC FILE COPY

DTIC
ELECTE
S DEC 0 9 1987
D

THESIS

INTERACTION OF A VORTEX PAIR
WITH A FREE SURFACE

by

John Elnitsky II

September 1987

Thesis Advisor: T. Sarpkaya

87 11 27 0

SECURITY CLASSIFICATION OF THIS PAGE

REPORT DOCUMENTATION PAGE

1a REPORT SECURITY CLASSIFICATION UNCLASSIFIED		1b RESTRICTIVE MARKINGS			
2a SECURITY CLASSIFICATION AUTHORITY		3 DISTRIBUTION / AVAILABILITY OF REPORT Approved for public release; distribution is unlimited.			
2b DECLASSIFICATION / DOWNGRADING SCHEDULE					
4 PERFORMING ORGANIZATION REPORT NUMBER(S)		5 MONITORING ORGANIZATION REPORT NUMBER(S)			
6a NAME OF PERFORMING ORGANIZATION Naval Postgraduate School	6b OFFICE SYMBOL (If applicable) 69	7a NAME OF MONITORING ORGANIZATION Naval Postgraduate School			
6c ADDRESS (City, State, and ZIP Code) Monterey, California 93943-5000		7b ADDRESS (City, State, and ZIP Code) Monterey, California 93943-5000			
8a NAME OF FUNDING / SPONSORING ORGANIZATION	8b OFFICE SYMBOL (If applicable)	9 PROCUREMENT INSTRUMENT IDENTIFICATION NUMBER			
8c ADDRESS (City, State, and ZIP Code)		10 SOURCE OF FUNDING NUMBERS			
		PROGRAM ELEMENT NO	PROJECT NO	TASK NO	WORK UNIT ACCESSION NO

11 TITLE (Include Security Classification)

INTERACTION OF A VORTEX PAIR WITH A FREE SURFACE

12 PERSONAL AUTHOR(S)
Elnitsky, John II

13a TYPE OF REPORT Master's Thesis	13b TIME COVERED FROM _____ TO _____	14 DATE OF REPORT (Year, Month, Day) 1987 September	15 PAGE COUNT 113

16 SUPPLEMENTARY NOTATION

17	COSATI CODES		18 SUBJECT TERMS (Continue on reverse if necessary and identify by block number) Vortex Convection, Free Surface Deformation
FIELD	GROUP	SUB-GROUP	

19 ABSTRACT (Continue on reverse if necessary and identify by block number)

The trailing vortices generated by the control planes of submarines give rise to surface signatures in the form of scars and striations.

Two counter-rotating vortices were generated in a novel experimental system and their interaction with the free surface was investigated. In addition, the governing equations have been solved through the use of the boundary-element method for a representative Froude number. The results have been expressed in terms of the depth of submergence of the vortices, their mutual induction velocity,

20 DISTRIBUTION / AVAILABILITY OF ABSTRACT ☒ UNCLASSIFIED/UNLIMITED ☐ SAME AS RPT ☐ DTIC USERS	21 ABSTRACT SECURITY CLASSIFICATION UNCLASSIFIED	
22a NAME OF RESPONSIBLE INDIVIDUAL T. Sarpkaya	22b TELEPHONE (Include Area Code) (408) 646-3425	22c OFFICE SYMBOL 69SL

DD FORM 1473, 84 MAR   83 APR edition may be used until exhausted   SECURITY CLASSIFICATION OF THIS PAGE
All other editions are obsolete

19. Abstract contd.

and the initial vortex separation. It has been shown that
the free surface begins to deform when the vortices are at
a distance of about one initial vortex separation from the
free surface. The height of the maximum deformation is
attained at a normalized time of about 0.1, when the vorti-
ces are at a distance of about $0.5b_o$ from the free surface.
The elevated part of the surface is bounded by two scars,
whose motion is slaved to that of the vortices.

A-1

Interaction of a Vortex Pair
With a Free Surface

by

John Elnitsky II
Lieutenant, United States Navy
B.S.M.E., United States Naval Academy, 1980

Submitted in partial fulfillment of the
requirements for the degree of

MASTER OF SCIENCE IN MECHANICAL ENGINEERING
and
MECHANICAL ENGINEER

from the

NAVAL POSTGRADUATE SCHOOL
September 1987

Author: _____
John Elnitsky II
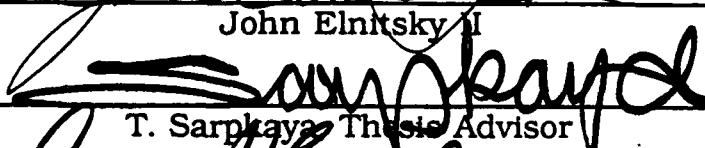
Approved by: _____
T. Sarpkaya, Thesis Advisor
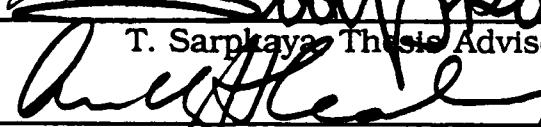
_____
Anthony J. Healy, Chairman
Department of Mechanical Engineering

_____
G. E. Schacher, Dean of
Science and Engineering

3

ABSTRACT

The trailing vortices generated by the control planes of submarines give rise to surface signatures in the form of scars and striations.

Two counter-rotating vortices were generated in a novel experimental system and their interaction with the free surface was investigated. In addition, the governing equations have been solved through the use of the boundary-element method for a representative Froude number. The results have been expressed in terms of the depth of submergence of the vortices, their mutual induction velocity, and the initial vortex separation. It has been shown that the free surface begins to deform when the vortices are at a distance of about one initial vortex separation from the free surface. The height of the maximum deformation is attained at a normalized time of about 0.1, when the vortices are at a distance of about 0.5 b_0 from the free surface. The elevated part of the surface is bounded by two scars, whose motion is slaved to that of the vortices.

4

TABLE OF CONTENTS

6

LIST OF FIGURES

TABLE OF SYMBOLS AND ABBREVIATIONS

b_o Initial vortex pair spacing

d_o Initial depth of the vortex pair

$F(t)$ Arbitrary function of time

F_v Froude number

g Gravitational acceleration

i $\sqrt{-1}$

L_c Characteristic length

L_{11} Integral scale of the turbulent field

n N_o^2/N_c^2

N_c Characteristic Brunt-Vaisala frequency

N_o Brunt-Vaisala frequency

P Pressure

P_a Ambient Pressure

q Scalar velocity $\sqrt{u^2 + v^2}$

q_m q/u_c

r_e Effective core radius of the vortex

R_e Reynolds number

r_m Nondimensional radial distance

R_1, R_2 Radii of curvature of the free surface

t Time

t_m Nondimensional time ($u_c t/L_c$ or tN_c)

u X-component of velocity

9

U_c Characteristic velocity

u_m u/U_c

v Y-component of velocity

v_m v/U_c

V_o Initial mutual induction velocity

$w(z)$ Complex velocity function

x Horizontal component of the coordinate axis (parallel to the line joining the vortex cores)

x_m x/L_c

y Vertical component of the coordinate axis

y_m y/L_c

x'_m, y'_m Position of vorticity

z_i Complex position of a vortex

z_o Complex position of the right-hand vortex in the vortex pair

$\bar{z}_i$ Complex conjugate of z_i

$\bar{z}_o$ Complex conjugate of z_o

$[B]$ Forcing function matrix

$[K]$ Coefficient matrix

$[U]$ Matrix of unknowns

ε Rate of decay of turbulent energy per unit mass

ε^* Nondimensional ε

Γ_m Circulation of a given distributed vortex

Γ_o Circulation of the vortex pair

η Position of the free surface

η_m η/L_c

ρ	Density of water
ρ_m	ρ/ρ_0
ρ_0	Reference density of water in stratified medium
$\bar{\rho}(y)$	Initial variation of density with y
$\rho'(x,y,t)$	Fluctuating part of density with time
$\varnothing$	Velocity potential
$\varnothing_m$	$\varnothing/\Gamma_0$
π	Geometric pie
ν	Kinematic viscosity of water
ζ	Vorticity
ζ_m	$\zeta L_c/U_c$
∇^2	Laplacian Operator $\left(\dfrac{\partial^2}{\partial x^2}+\dfrac{\partial^2}{\partial y^2}\right)$
∇_m^2	Nondimensional Laplacian operator $\left(\dfrac{\partial^2}{\partial x_m^2}+\dfrac{\partial^2}{\partial y_m^2}\right)$
σ	Surface tension

ACKNOWLEDGMENT

The author wishes to express his sincere thanks to Distinguished Professor T. Sarpkaya for his invaluable assistance, guidance, and patience throughout this investigation and especially during the many months of program development. I'm sure to him it seems more like years. It has been a true privilege to share some of this man's genius and understanding of nature. I consider this opportunity to be the hallmark of my experience at the Naval Postgraduate School.

Also, the author wishes to thank Mr. Jack McKay of the Mechanical Engineering Department Machine Shop for his hard work and unique craftsmanship in building and operating the experimental apparatus.

I. INTRODUCTION

Vortices and vortex wakes have become a major theme of aerodynamics research since the advent of the large aircraft and the understanding of their evolution required an examination of many of the fundamental problems in fluid mechanics. Much of the progress made during the past two decades was discussed at the Symposium on Aircraft Wake Turbulence and Its Detection [Ref. 1] and the Aircraft Wake Vortices Conference [Ref. 2]. Comprehensive reviews of the entire subject have been given by Donaldson and Bilanin [Ref. 3], Widnall [Ref. 4], and Hallock and Eberle [Ref. 5].

These studies, as well as numerous others carried out since 1977, have uncovered a number of complex problems which must be resolved in order to achieve a better understanding of the important features of trailing vortices in homogeneous and stratified media. The principal ones are as follows [Ref. 6]:

1. Roll-up process: The velocity and turbulence distribution at any station behind the wing depend on the wing section, wing-tip shape, Reynolds number, wing incidence, and the distance of the station from the wing [Ref. 7]. The distributions of the initial velocity and turbulence, which influence the roll-up and the decay process, cannot be changed independently. For example, a change in the tip shape changes the core size, as well as the velocity and turbulence distributions. High levels of turbulence result in an increased diffusion of vorticity, which in turn increase the core size.

2. Probe sensitivity of the vortices: Flow visualization studies suggest that trailing vortices are extremely sensitive to disturbances created by even very small probes or bubbles. This

13

forces one to use non–intrusive means of measurement such as a Laser Doppler Velocimeter. Even then, "vortex wandering" [Ref. 8], which makes the vortices appear larger than normal in time–averaged velocity measurements (for vortices generated by a wing in a wind tunnel), or the unsteady nature of the flow (for vortices generated by a wing in a tow basin) makes the mean velocity profiles in the vortices difficult to determine.

3. Large–scale instabilities: The vortices are seldom observed to decay away owing to viscous and turbulent dissipation, but are almost always destroyed by either mutual induction instability (Crow instability [Ref. 9]) and/or vortex breakdown. The Crow instability grows exponentially, and results either in linking of the vortex pair into a series of crude vortex rings or in a highly disorganized intermingling of the vortices.

   Vortex breakdown, whose mathematical details have not yet been adequately treated, rearranges the vortex structure and increases the core size, turbulence, and energy dissipation. Thus, it is very difficult to measure accurately the trajectories of the three–dimensional vortices from their creation to their ultimate demise.

4. Reynolds number: Even the highest Reynolds numbers, based on wing chord, reached in wind tunnels or towing basins, are an order of magnitude lower than what is possible for an aircraft. Thus, the scale effects are not easy to assess.

5. Ambient conditions such as turbulence and stratification play major roles in the evolution of vortices. The quantification of these effects requires numerical analysis and extremely careful experiments [Ref. 10].

6. Ground or free surface effects: The vortex pair may move toward a rigid boundary at which the no–slip condition must be satisfied or toward a free surface at which the zero–shear condition must be satisfied. In either case, the vortices come under the influence of their images and move accordingly.

The phenomenon is further complicated by several additional facts. When the vortices are propelled toward a rigid surface, vorticity of opposite sign is generated on the no–slip boundary and swept toward the vortex pair. The total vorticity diminishes very quickly as vorticity from the two regions diffuses, the wall region serving as a

14

strong sink for the vorticity associated with the original vortex [Ref. 11]. The development of a boundary layer along the rigid wall may give rise to flow separation for sufficiently high Reynolds numbers. With or without such a separation, however, the center of the vortex pair eventually moves away, or "rebounds," from the wall [Refs. 11–13].

For the case of a zero–stress boundary, the free surface still acts as a vorticity sink, but this is relatively weak due to the absence of intense oppositely signed vorticity. Thus, in the absence of other impending phenomena, one expects a mild interaction between the vortices and the free surface and a small rebound of the vortex pair from the free surface. However, the ability of the free surface to deform under the influence of strain fields leads to a strong interaction between the vortices and the free surface.

It is evident from the foregoing that the motion and the life–span of trailing vortices are governed by a number of nonlinearly dependent complex phenomena. A number a experimental and analytical studies have been carried out at the Naval Postgraduate School by Sarpkaya and his students [Refs. 6, 14–21] in order to investigate the effects of these parameters on the rise and demise of the trailing vortices in homogeneous and density stratified media. These studies have clearly identified the various demise mechanisms in both media and established basic relationships between the rise of vortices and the governing parameters in a finite as well as effectively infinite medium [Ref. 20], free from ambient turbulence.

15

The present investigation is a continuation and refinement of the previous studies. The intent is to analyze the rise and demise of a vortex pair in a medium with a deformable free surface. This problem is of interest both from the standpoint of determining the interaction effect of the free surface on the rise and demise of the vortex pair and from the standpoint of predicting the resulting free surface shape.-

16

II. PHYSICAL ANALYSIS

A. DIMENSIONAL ANALYSIS

The dependent parameter of major importance to the problem solution is the instantaneous position of the vortex pair (x, y). It may be expressed as a function of the following parameters [Ref. 22]:

$$x = f(t, V_0, d_0, \rho_0, d\rho/dy, \nu, b_0, g, r_e, \varepsilon, L_{11}) \qquad (1)$$

and

$$y = f(t, V_0, d_0, \rho_0, d\rho/dy, \nu, b_0, g, r_e, \varepsilon, L_{11}) \qquad (2)$$

in which the variable definitions are as follows:

t	time
V_0	initial mutual induction velocity of the vortices
d_0	initial depth of the vortex pair
ρ_0	reference density of the medium
$d\rho/dy$	linear density gradient
ν	kinematic viscosity of the medium
b_0	initial separation of the vortex pair
g	gravitational acceleration
r_e	effective core radius of the vortex
ε	rate of decay of the turbulent energy per unit mass
L_{11}	integral scale of the turbulent field

The height and width of the test section were not included in the foregoing because a detailed analysis, based on ideal vortices, has shown that the velocities induced by the bottom or sides were

17

negligible. Effects of surface tension on the instantaneous position of the vortex pair are deemed negligible and thus are not included as a parameter in equations (1) and (2).

A dimensional analysis of equations (1) and (2) yields:

$$x/b_0 = f(V_0t/b_0, d_0/b_0, N_0b_0/V_0, V_0^2/gb_0, V_0b_0/\nu, r_e/b_0, \varepsilon^*, L_{11}/b_0) \quad (3)$$

and

$$y/b_0 = f(V_0t/b_0, d_0/b_0, N_0b_0/V_0, V_0^2/gb_0, V_0b_0/\nu, r_e/b_0, \varepsilon^*, L_{11}/b_0) \quad (4)$$

in which

$$N_0 = \left(\frac{-g}{\rho_0} \frac{d\rho}{dy}\right)^{1/2} \quad (5)$$

is known as the Brunt-Vaisala Frequency.

All parameters in equations (3) and (4) may be changed independently except r_e/b_0, which is taken as nature provides it. The primary reason for this is that a century of theoretical and experimental aerodynamics research has been incapable of describing the details of the structure of the tip vortex to be used as the initial conditions in the viscous solution. It is surprising, but true, that until recently the importance of the generating surface shape and its influence upon both the initial tangential velocity profile and the initial turbulence in the vortex core had not been fully appreciated. Here the said influence has been characterized in terms of an effective core radius with full awareness of its shortcomings.

18

B. GOVERNING DIFFERENTIAL EQUATIONS AND BOUNDARY CONDITIONS

The generation of internal waves and the rise and demise of a vortex pair in a stratified medium may be analyzed through the use of the equations of motion for an incompressible fluid. These equations may be applied for both laminar and turbulent motions provided that a suitable turbulence closure model is used and the usual Boussinesq approximation (gravitational acceleration is much larger than fluid acceleration) is adopted. For the type of motion considered herein, the Boussinesq approximation is quite valid and has been used in the investigation of all types of internal waves in stratified fluids.

For a two-dimensional flow, with y vertical and x horizontal, the Navier-Stokes equations of motion are:

$$\frac{\partial u}{\partial t} + u\frac{\partial u}{\partial x} + v\frac{\partial u}{\partial y} = -\frac{1}{\rho}\frac{\partial P}{\partial x} + \nu\nabla^2 u \tag{6}$$

$$\frac{\partial v}{\partial t} + u\frac{\partial v}{\partial x} + v\frac{\partial v}{\partial y} = g - \frac{1}{\rho}\frac{\partial P}{\partial y} + \nu\nabla^2 v \tag{7}$$

Differentiating equations (6) and (7) with respect to y and x respectively yields

$$\frac{\partial^2 u}{\partial y\partial t} + \frac{\partial^2 u}{\partial x\partial y} + u\frac{\partial^2 u}{\partial x\partial y} + \frac{\partial v}{\partial y}\frac{\partial u}{\partial y} + v\frac{\partial^2 u}{\partial^2 y} = \frac{1}{\rho^2}\frac{\partial\rho}{\partial y}\frac{\partial P}{\partial x} - \frac{1}{\rho}\frac{\partial^2 P}{\partial x\partial y} + \nu\frac{\partial}{\partial y}(\nabla^2 u) \tag{8}$$

$$\frac{\partial^2 v}{\partial x\partial t} + \frac{\partial u}{\partial x}\frac{\partial v}{\partial x} + u\frac{\partial^2 v}{\partial x^2} + \frac{\partial^2 v}{\partial x\partial y} + v\frac{\partial^2 v}{\partial x\partial y} = \frac{1}{\rho^2}\frac{\partial\rho}{\partial x}\frac{\partial P}{\partial y} - \frac{1}{\rho}\frac{\partial^2 P}{\partial x\partial y} + \nu\frac{\partial}{\partial x}(\nabla^2 v) \tag{9}$$

Subtracting equation (9) from equation (8) yields

19

Subtracting equation (9) from equation (8) yields

$$\frac{\partial}{\partial t}\left(\frac{\partial u}{\partial y} - \frac{\partial v}{\partial x}\right) + \frac{\partial}{\partial x}\left[u\left(\frac{\partial u}{\partial y} - \frac{\partial v}{\partial x}\right)\right] + \frac{\partial}{\partial y}\left[v\left(\frac{\partial u}{\partial y} - \frac{\partial v}{\partial x}\right)\right] = \frac{1}{\rho^2}\frac{\partial \rho}{\partial y}\frac{\partial P}{\partial x} -$$

$$\frac{1}{\rho^2}\frac{\partial \rho}{\partial x}\frac{\partial P}{\partial y} + \nu\nabla^2\left(\frac{\partial u}{\partial y} - \frac{\partial v}{\partial x}\right) \qquad (10)$$

Solving equation (6) for $\frac{1}{\rho}\frac{\partial P}{\partial x}$ yields

$$\frac{1}{\rho}\frac{\partial P}{\partial x} = \nu\nabla^2 u - \frac{Du}{Dt} \qquad (11)$$

where

$$\frac{D(\ )}{Dt} = \frac{\partial(\ )}{\partial t} + u\frac{\partial(\ )}{\partial x} + v\frac{\partial(\ )}{\partial y}$$

Solving equation (7) for $\frac{1}{\rho}\frac{\partial P}{\partial y}$ yields

$$\frac{1}{\rho}\frac{\partial P}{\partial y} = g + \nu\nabla^2 v - \frac{Dv}{Dt} \qquad (12)$$

Substituting the results of equations (11) and (12) into equation (10) and defining vorticity as

$$\zeta = \left(\frac{\partial u}{\partial y} - \frac{\partial v}{\partial x}\right) \qquad (13)$$

20

results in the following expression:

$$\frac{\partial \zeta}{\partial t} + \frac{\partial (u\zeta)}{\partial x} + \frac{\partial (v\zeta)}{\partial y} = \nu \nabla^2 \zeta - \frac{g}{\rho}\frac{\partial P}{\partial x} + \left[\frac{1}{\rho}\frac{\partial \rho}{\partial y}\left(\nu \nabla^2 u - \frac{Du}{Dt} \right) - \right.$$

$$\left. \frac{1}{\rho}\frac{\partial \rho}{\partial y}\left(\nu \nabla^2 v - \frac{Dv}{Dt} \right) \right] \tag{14}$$

When the gravitational acceleration is several orders of magnitude larger than the fluid accelerations, the Boussinesq approximation is appropriately invoked and the terms in brackets in equation (14) may be neglected.

In order to deal with the case of a density stratified medium, the density is defined as

$$\rho = \rho_0 + \overline{\rho}(y) + \rho'(x,y,t) \tag{15}$$

where ρ_0 is the reference density, $\overline{\rho}(y)$ is the initial variation of density with y, and $\rho'(x,y,t)$ is the fluctuating part of the density with time. Then

$$\frac{\partial \rho}{\partial x} = \frac{\partial \rho'}{\partial x}$$

and equation (14), neglecting the bracketed terms, becomes

$$\frac{\partial \zeta}{\partial t} + \frac{\partial (u\zeta)}{\partial x} + \frac{\partial (v\zeta)}{\partial y} = \nu \nabla^2 \zeta - \frac{g}{\rho_0}\frac{\partial \rho'}{\partial x} \tag{16}$$

21

The last term above represents the effect of the density gradient and gives rise to oppositely signed vorticity in a nonhomogeneous fluid. The diffusion of density is given by

$$\frac{\partial \rho}{\partial t} + u\frac{\partial \rho}{\partial x} + v\frac{\partial \rho}{\partial y} = \nu\nabla^2\rho \tag{17}$$

Substituting equation (15) for density in the above equation yields

$$\frac{\partial \rho'}{\partial t} + u\frac{\partial \rho'}{\partial x} + v\left(\frac{\partial \overline{\rho}}{\partial y} + \frac{\partial \rho'}{\partial y}\right) = \nu\left(\frac{\partial^2 \rho'}{\partial x^2} + \frac{\partial^2 \overline{\rho}}{\partial y^2} + \frac{\partial^2 \rho'}{\partial y^2}\right) \tag{18}$$

The equation of continuity is

$$\frac{\partial u}{\partial x} + \frac{\partial v}{\partial y} = 0 \tag{19}$$

Adding equation (19) to the left side of equation (18) and simplifying results in

$$\frac{\partial \rho'}{\partial t} + \frac{\partial(u\rho)}{\partial x} + \frac{\partial(v\rho)}{\partial y} = -\nu\frac{\partial \overline{\rho}}{\partial y} + \nu\nabla^2\rho' + \nu\frac{\partial^2 \overline{\rho}}{\partial y^2} \tag{20}$$

Equations (16) and (20) are thus the governing differential equations for the motion of a vortex pair in a density stratified fluid.

For the development of boundary conditions, it is assumed at the outset that the influence of the sidewalls and bottom of the test section on the rise and demise of the vortex pair is negligible. The validity of this assumption, when used in conjunction with numerical computations, has been demonstrated by previous investigators [Refs. 18-20]. The fluid domain can thus be considered to be bounded only

22

by a free surface which can be described as a function of x and time as follows:

$$y = \eta(x,t)$$

where

$$\eta(x,o) = 0$$

describes the initial undisturbed location of the free surface.

The free surface requires both a kinematic and a dynamic boundary condition as described by Sarpkaya and Issacson [Ref. 22]. The kinematic condition states that any particle which lies on the free surface at any instant will never leave it. This leads to

$$\frac{D\eta}{Dt} = \frac{\partial \eta}{\partial t} + u\frac{\partial \eta}{\partial x} = v \ \ \text{at} \ \ y = \eta \tag{21}$$

The dynamic free surface condition requires that the pressure difference across the interface results in a force normal to the boundary which is due wholly to surface tension. This condition takes the form

$$P = P_a + \sigma\left(\frac{1}{R_1} + \frac{1}{R_2}\right) \tag{22}$$

where σ is the surface tension, $\frac{1}{R_1}$ and $\frac{1}{R_2}$ are the radii of curvature of the free surface in any two orthogonal directions, and $P - P_a$ is the pressure difference across the interface.

23

As noted previously, the effects of surface tension can be assumed to be negligible. This observation has been verified experimentally by Gray [Ref. 17]. Thus, if the flow is considered inviscid, the pressure P within the fluid can be described by the unsteady Bernoulli equation as follows:

$$\frac{\partial \varnothing}{\partial t} + \frac{q^2}{2} + g\eta + \frac{P}{\rho} = F(t) \tag{23}$$

where $\varnothing$ is the velocity potential such that

$$u = \frac{\partial \varnothing}{\partial x} \qquad v = \frac{\partial \varnothing}{\partial y} \tag{24}$$

and $q^2 = u^2 + v^2$. $F(t)$ is an arbitrary function of time only.

When the pressure just outside the liquid is constant (i.e., atmospheric), the free surface condition reduces to

$$\frac{\partial \varnothing}{\partial t} + \frac{q^2}{2} + g\eta = 0 \quad \text{at} \quad y = \eta \tag{25}$$

where $F(t)$ has been included as part of $\frac{\partial \varnothing}{\partial t}$.

C. DIMENSIONLESS PARAMETERS

It is convenient at this point to cast the governing equations, (15) and (20), in nondimensional forms, scaling each variable by a quantity characteristic of its expected magnitude. Two possible time scales exist. The dynamic time scale utilizes the time a characteristic length would be traversed by a fluid particle traveling at the characteristic velocity. The buoyant time scale is based on the natural buoyancy

24

frequency of the stratified flow, i.e., the Brunt-Vaisala frequency N_0 defined by equation (5). Each of these scales gives a slightly different form of the normalized governing equations.

1. Dynamic Scale

Introducing U_c and L_c as the characteristic velocity and length, one has the following nondimensionalized quantities:

$$\zeta_m = \zeta L_c/U_c \qquad t_m = U_c t/L_c \qquad u_m = u/U_c \qquad v_m = v/U_c$$

$$x_m = x/L_c \qquad y_m = y/L_c \qquad \rho_m = \rho/\rho_0 \qquad (26)$$

Substituting the above into equation (16) yields

$$\frac{U_c}{L_c} \frac{\partial}{\partial t_m}\left(\frac{\zeta_m U_c}{L_c}\right) + \frac{1}{L_c}\frac{\partial}{\partial x_m}\left(u_m U_c \frac{\zeta_m U_c}{L_c}\right) + \frac{1}{L_c}\frac{\partial}{\partial y_m}\left(v_m U_c \frac{\zeta_m U_c}{L_c}\right) =$$

$$\frac{1}{L_c^2} \nu \nabla_m^2 \left(\frac{\zeta_m U_c}{L_c}\right) + \frac{g}{L_c \rho_0}\frac{\partial}{\partial x_m}(\rho_0 \rho'_m) \qquad (27)$$

Simplifying

$$\frac{U_c^2}{L_c^2}\frac{\partial \zeta_m}{\partial t_m} + \frac{U_c^2}{L_c^2}\frac{\partial(u_m\zeta_m)}{\partial x_m} + \frac{U_c^2}{L_c^2}\frac{\partial(v_m\zeta_m)}{\partial y_m} = \frac{U_c}{L_c^3}\nu\nabla_m^2 \zeta_m + \frac{g}{L_c}\frac{\partial \rho'_m}{\partial x_m}$$

which becomes

$$\frac{\partial \zeta_m}{\partial t_m} + \frac{\partial(u_m\zeta_m)}{\partial x_m} + \frac{\partial(v_m\zeta_m)}{\partial y_m} = \frac{\nu}{U_c L_c}\nabla_m^2 \zeta_m + \frac{g L_c}{U_c^2}\frac{\partial \rho'_m}{\partial x_m} \qquad (28)$$

or

$$\frac{\partial \zeta_m}{\partial t_m} + \frac{\partial(u_m\zeta_m)}{\partial x_m} + \frac{\partial(v_m\zeta_m)}{\partial y_m} = \frac{1}{R_e}\nabla_m^2 \zeta_m + \frac{1}{F_v^2}\frac{\partial \rho'_m}{\partial x_m} \qquad (29)$$

25

where

$$R_e = U_c L_c / \nu \qquad \text{(characteristic Reynolds number)}$$

$$F_v = U_s / \sqrt{g L_c} \qquad \text{(characteristic Froude number)}$$

Similarly, the density diffusion equation may be expressed in nondimensional terms by making equivalent substitutions into equation (20) as follows:

$$\frac{\partial \rho'}{\partial t} + \frac{\partial (u\rho')}{\partial x} + \frac{\partial (v\rho')}{\partial y} = -v\frac{\partial \bar{\rho}}{\partial y} + \nu \nabla^2 \rho' + \nu \frac{\partial^2 \bar{\rho}}{\partial y^2}$$

This becomes

$$\frac{U_c}{L_c}\frac{\partial}{\partial t_m}(\rho_o\rho'_m) + \frac{1}{L_c}\frac{\partial}{\partial x_m}(U_c u_m \rho_o \rho'_m) + \frac{1}{L_c}\frac{\partial}{\partial y_m}(v_m U_c \rho_o \rho'_m) =$$

$$-\frac{U_c v_m}{L_c}\frac{\partial}{\partial y_m}(\rho_o\rho'_m) + \frac{\nu}{L_c^2}\nabla_m^2(\rho_o\rho'_m) + \frac{\nu}{L_c^2}\frac{\partial^2(\rho_o\rho'_m)}{\partial y_m^2}$$

Which upon simplification reduces to

$$\frac{U_c\rho_o}{L_c}\frac{\partial\rho'_m}{\partial t_m} + \frac{U_c\rho_o}{L_c}\frac{\partial(u_m\rho'_m)}{\partial x_m} + \frac{U_c\rho_o}{L_c}\frac{\partial(v_m\rho'_m)}{\partial y_m} =$$

$$-\frac{U_c\rho_o}{L_c}v_m\frac{\partial\bar{\rho}_m}{\partial y_m}\frac{\nu\rho_o}{L_c^2}\nabla_m^2\rho'_m + \frac{\nu\rho_o}{L_c^2}\frac{\partial^2\bar{\rho}_m}{\partial y_m^2}$$

Multiplying both sides by $L_c/\rho_o U_c$ yields

$$\frac{\partial\rho'_m}{\partial t_m} + \frac{\partial(u_m\rho'_m)}{\partial x_m} + \frac{\partial(v_m\rho'_m)}{\partial y_m} = -v_m\frac{\partial\bar{\rho}_m}{\partial y_m} + \frac{\nu}{U_c L_c}\left(\nabla_m^2\rho'_m + \frac{\partial^2\bar{\rho}_m}{\partial y_m^2}\right) \qquad (30)$$

26

Incorporating the characteristic Reynolds number, this equation becomes

$$\frac{\partial \rho'_m}{\partial t_m} + \frac{\partial (u_m \rho'_m)}{\partial x_m} + \frac{\partial (v_m \rho'_m)}{\partial y_m} = -v_m \frac{\partial \overline{\rho}_m}{\partial y_m} + \frac{1}{R_e}\left(\nabla_m^2 \rho'_m + \frac{\partial^2 \overline{\rho}_m}{\partial y_m^2}\right) \qquad (31)$$

The Brunt–Vaisala frequency given by equation (5) as

$$N_o = \left(\frac{-g}{\rho_o}\frac{\partial \overline{\rho}}{\partial y}\right)^{1/2}$$

may be written as

$$N_o^2 = \frac{-g}{\rho_o L_c}\frac{\partial (\rho_o \overline{\rho}_m)}{\partial y_m}$$

which becomes

$$\frac{N_o^2 L_c}{g} = -\frac{\partial \overline{\rho}_m}{\partial y_m}$$

To further simplify equation (31), the following definitions are made:

$$N_c^2 = g/L_c \qquad \text{(characteristic Brunt–Vaisala frequency squared)} \qquad (33)$$

and

$$n = \frac{N_o^2}{N_c^2} = \frac{N_o^2 L_c}{g} = -\frac{\partial \overline{\rho}_m}{\partial y_m} \qquad (34)$$

Substituting equation (34) into equation (31), the nondimensional form of the density diffusion equation in final form becomes

27

$$\frac{\partial \rho'_m}{\partial t_m} + \frac{\partial (u_m \rho'_m)}{\partial x_m} + \frac{\partial (v_m \rho'_m)}{\partial y_m} = n^2 v_m + \frac{1}{R_e}\left(\nabla^2_m \rho'_m + \frac{\partial^2 \bar{\rho}_m}{\partial y_m^2}\right) \tag{35}$$

2. Buoyant Scale

Again introducing U_c and L_c as the characteristic velocity and length, the following nondimensional quantities are defined:

$$u_m = \frac{u}{U_c} \qquad v_m = \frac{v}{U_c} \qquad x_m = \frac{x}{L_c} \qquad y_m = \frac{y}{L_c} \qquad \rho_m = \frac{\rho}{\rho_o}$$

In this case, however, time is nondimensionalized using the square of the characteristic Brunt-Vaisala frequency. Namely

$$N_c^2 = g/L_c$$

and then

$$t_m = t N_c$$

also

$$\zeta_m = \zeta/N_c$$

Substituting the above into the governing equation given by equation (16) yields

$$N_c \frac{\partial}{\partial t_m}(\zeta_m N_c) + \frac{1}{L_c}\frac{\partial}{\partial x_m}(u_m U_c \zeta_m N_c) + \frac{1}{L_c}\frac{\partial}{\partial y_m}(v_m U_c \zeta_m N_c) =$$

$$\frac{1}{L_c^2} \nu \nabla^2_m (\zeta_m N_c) + \frac{g}{L_c \rho_o}\frac{\partial}{\partial x_m}(\rho_o \rho'_m)$$

28

simplifying

$$N_c^2 \frac{\partial \zeta_m}{\partial t_m} + \frac{U_c N_c}{L_c} \frac{\partial}{\partial x_m}(u_m \zeta_m) + \frac{U_c N_c}{L_c} \frac{\partial}{\partial y_m}(v_m \zeta_m) = \frac{N_c}{L_c^2} \nu \nabla_m^2 \zeta_m + \frac{g}{L_c} \frac{\partial \rho'_m}{\partial x_m}$$

which becomes

$$\frac{\partial \zeta_m}{\partial t_m} + \frac{U_c}{L_c N_c} \frac{\partial(u_m \zeta_m)}{\partial x_m} + \frac{U_c}{L_c N_c} \frac{\partial(v_m \zeta_m)}{\partial y_m} = \frac{\nu}{N_c L_c^2} \nabla_m^2 \zeta_m + \frac{g}{N_c^2 L_c} \frac{\partial \rho'_m}{\partial x_m} \qquad (36)$$

but

$$\frac{g}{N_c^2 L_c} = \frac{N_c^2}{N_c^2} = 1$$

Thus equation (36) becomes

$$\frac{\partial \zeta_m}{\partial t_m} + \frac{U_c}{\sqrt{gL_c}} \left(\frac{\partial(u_m \zeta_m)}{\partial x_m} + \frac{\partial(v_m \zeta_m)}{\partial y_m} \right) = \frac{\nu}{\sqrt{gL_c}\, L_c} \frac{U_c}{U_c} \nabla_m^2 \zeta_m + \frac{\partial \rho'_m}{\partial x_m}$$

or

$$\frac{\partial \zeta_m}{\partial t_m} + F_v \left[\frac{\partial(u_m \zeta_m)}{\partial x_m} + \frac{\partial(v_m \zeta_m)}{\partial y_m} \right] = \frac{F_v}{R_e} \nabla_m^2 \zeta_m + \frac{\partial \rho'_m}{\partial x_m} \qquad (37)$$

where F_v and R_e are as defined above.

The density diffusion equation is similarly nondimensionalized as

$$\frac{\partial \rho'}{\partial t} + \frac{\partial(u\rho')}{\partial x} + \frac{\partial(v\rho')}{\partial y} = -v \frac{\partial \bar{\rho}}{\partial y} + \nu \nabla^2 \rho' + \nu \frac{\partial^2 \bar{\rho}}{\partial y^2}$$

29

which becomes

$$N_c \frac{\partial}{\partial t_m}(\rho_o \rho'_m) + \frac{1}{L_c} \frac{\partial}{\partial x_m}(u_m U_c \rho_o \rho'_m) + \frac{1}{L_c} \frac{\partial}{\partial y_m}(v_m U_c \rho_o \rho'_m) =$$

$$-\frac{U_c v_m}{L_c} \frac{\partial}{\partial y_m}(\rho_o \overline{\rho}_m) + \frac{\nu}{L_c^2} \nabla_m^2 (\rho_o \rho'_m) + \frac{\nu}{L_c^2} \frac{\partial^2}{\partial y_m^2}(\rho_o \overline{\rho}_m)$$

The above equation can be simplified to yield

$$\rho_o N_c \frac{\partial \rho'_m}{\partial t_m} + \frac{U_c \rho_o}{L_c} \frac{\partial}{\partial x_m}(u_m \rho'_m) + \frac{U_c \rho_o}{L_c} \frac{\partial}{\partial y_m}(v_m \rho'_m) =$$

$$\frac{-U_c \rho_o}{L_c} v_m \frac{\partial \overline{\rho}_m}{\partial y_m} + \frac{\rho_o \nu}{L_c^2} \nabla_m^2 \rho'_m + \frac{\nu \rho_o}{L_c^2} \frac{\partial^2 \overline{\rho}_m}{\partial y_m^2}$$

Introducing F_v and R_e as before and recalling that $N_c^2 = \frac{g}{L_c}$, one has

$$\frac{\partial \rho'_m}{\partial t_m} + F_v \left[\frac{\partial(u_m \rho'_m)}{\partial x_m} + \frac{\partial(v_m \rho'_m)}{\partial y_m} \right] = F_v v_m \frac{\partial \overline{\rho}_m}{\partial y_m} +$$

$$\frac{F_v}{R_e} \left(\nabla_m^2 \rho'_m + \frac{\partial^2 \overline{\rho}_m}{\partial_m^2} \right) \tag{38}$$

Now as developed above in equation (34)

$$n^2 = \frac{\partial \overline{\rho}_m}{\partial y_m} \quad \text{where} \quad n^2 = \frac{N_o^2}{N_c^2} = \frac{N_o^2 L_c}{g}$$

Substituting for $\frac{\partial \overline{\rho}_m}{\partial y_m}$ in equation (38) yields the nondimensionalized density diffusion equation

$$\frac{\partial \rho'_m}{\partial t_m} + F_v \left[\frac{\partial(u_m \rho'_m)}{\partial x_m} + \frac{\partial(v_m \rho'_m)}{\partial y_m} \right] = F_v n^2 v_m + \frac{F_v}{R_e} \left(\nabla_m^2 \rho'_m + \frac{\partial^2 \overline{\rho}_m}{\partial y_m^2} \right) \tag{39}$$

30

Equations (37) and (39) are valid when $F_v \ll 1$ and buoyancy dominates the flow. When F_v approaches zero, the equations that result from equations (37) and (39) describe the propagation of linear internal waves. The buoyant scaled forms of the governing equations are of interest to the present investigation because, for submerged bodies of naval interest, F_v is typically about 0.001 and thus significantly less than one.

Having established the buoyant scale as the form of interest, the boundary conditions can also be nondimensionalized using the same technique. From equation (21),

$$\frac{\partial \eta}{\partial t} + u\frac{\partial \eta}{\partial x} = v \text{ at } y = \eta$$

which becomes

$$N_c L_c \frac{\partial \eta_m}{\partial t_m} + \frac{U_c u_m}{L_c}\frac{\partial \eta_m}{\partial x_m} = U_c v_m$$

where

$$\eta_m = \eta/L_c$$

Simplifying the above yields

$$\frac{\partial \eta_m}{\partial t_m} + \frac{U_c}{N_c L_c} u_m \frac{\partial \eta_m}{\partial x_m} = \frac{U_c}{N_c L_c} v_m$$

Introducing F_v as before

$$\frac{\partial \eta_m}{\partial t_m} + F_v \, u_m \frac{\partial \eta_m}{\partial x_m} = F_v v_m \text{ at } y_m = \eta_m \tag{40}$$

and

$$\varnothing_m = \frac{\varnothing}{N_c L_c^2} \quad \text{(nondimensional velocity potential)}$$

Equation (25) can be nondimensionalized as follows:

$$\frac{\partial \varnothing}{\partial t} + \frac{q^2}{2} + g\eta = 0$$

becomes

$$N_c \frac{\partial(\varnothing_m N_c L_c^2)}{\partial t_m} + \frac{U_c^2 q_m^2}{2} + gL_c\eta_m = 0 \tag{41}$$

where

$$q_m^2 = u_m^2 + v_m^2$$

Further simplifying equation (41) yields

$$\frac{\partial \varnothing_m}{\partial t_m} + \frac{U_c^2}{N_c^2 L_c^2} \frac{q_m^2}{2} + \frac{g\eta_m}{N_c^2 L_c} = 0 \tag{42}$$

but

$$\frac{g}{N_c^2 L_c} = 1 \qquad \text{and} \qquad \frac{U_c^2}{N_c^2 L_c^2} = F_v^2$$

Thus equation (42) becomes

$$\frac{\partial \varnothing_m}{\partial t_m} + F_v^2 \frac{q_m^2}{2} + \eta_m = 0 \quad \text{at} \quad y_m = \eta_m$$

For the purposes of the present investigation, the flow will be assumed to be inviscid, i.e. the viscous diffusion will be ignored to a first order approximation. The nondimensionalized forms of the governing equations and boundary conditions are summarized in Figure 1.

III. NUMERICAL SOLUTION TECHNIQUES

A. INTRODUCTION

The significant difference between this study and the work of previous investigators is the introduction of a deformable free surface and the resulting complex interplay between kinetic and potential energies. The computational domain thus has an unknown boundary on which a double condition must be imposed as previously outlined. This complexity, as well as several other specific features of this problem, directly influences the ability of a numerical method to converge to an adequate solution.

The governing differential equations and boundary conditions are both nonlinear. Sarpkaya and Issacson [Ref. 23] note that for small amplitude waves (amplitude << wavelength), the boundary conditions at the free surface may be linearized. This approach, although possibly valid in the vicinity of surface striations, would not be valid for the scar front where observed light diffraction patterns [Ref. 17] indicate very small radii of curvature. Additionally, Haussling and Coleman [Ref. 24] have demonstrated numerically the importance of nonlinear terms in solving the free surface problem in the vicinity of the generation source. This is the case encountered in the region of the scar front.

The rate of change of the free surface deformations also tends to be slow. The scar pattern develops as the vortex pair rises to its maximum height and then the scar is trapped by and slaved to the

34

vortex beneath the surface. The scars and striations are thus not small amplitude surface waves propagating independently from their generator, but are in fact local disturbances whose generation, growth, and propagation are controlled by the vortices. This aspect, observed experimentally by Gray [Ref. 17], separates this problem from other research in the field of deformable free surfaces. Previous investigators, applying numerical methods to such surfaces, have dealt almost exclusively with surface waves generated by a moving body (surfaced or submerged) and propagating away independently.

The numerical methods reviewed for solution of this problem can be broadly categorized into Finite Differences, Finite Elements, Boundary Integral Equations, and Hybrid Methods which employ combinations of the others. For the purposes of this study, such categorization is based on the manner in which the governing equations are tackled in the computational domain. It is noted that all of the methods reviewed utilize some form of finite difference scheme with respect to time. The applicability of each method and the associated advantages and disadvantages are discussed and summarized at the end of this chapter.

B. FINITE DIFFERENCE TECHNIQUES

The use of Finite Difference techniques in solving partial differential equations has been well established and successfully implemented by several investigators. For the case of a nondeforming free surface, the governing equations are solved in the computational domain using

35

$$\frac{\partial \zeta}{\partial t} + \frac{\partial (u\zeta)}{\partial x} + \frac{\partial (v\zeta)}{\partial y} = \nu\nabla^2\zeta - \frac{g}{\rho_o}\frac{\partial \rho'}{\partial x} \qquad (30)$$

and

$$\frac{\partial \rho'}{\partial t} + \frac{\partial (u\rho)}{\partial x} + \frac{\partial (v\rho)}{\partial y} = -\frac{\nu\partial\overline{\rho}}{\partial y} + \nu\nabla^2\rho' + \nu\frac{\partial^2\overline{\rho}}{\partial y^2}$$

and the Biot–Savart integrals

$$u(x,y) = \int_A \frac{(y'-y)\,\zeta\,(x',\,y')\,dx'dy'}{2\pi r^2} \qquad (31)$$

$$v(x,y) = \int_A \frac{(x-x')\,\zeta\,(x',\,y')\,dx'dy'}{2\pi r^2} \qquad (32)$$

where

$r^2 = (x - x') + y - y')$

x', y': position of the vorticity

x, y: point where u and v are to be calculated

In nondimensional form, the buoyantly scaled forms of equations (31) and (32) become

$$u_m\,(x_m,y_m) = \int_A \frac{(y'_m - y_m)\,\zeta_m\,(x'_m,\,y'_m)\,dx'_m\,dy'_m}{2\pi r_m^2}\,\frac{L_c N_c}{U_c}$$

$$v_m\,(x_m,y_m) = \int_A \frac{(x_m - x'_m)\,\zeta_m\,(x'_m,\,y'_m)\,dx'_m\,dy'_m}{2\pi r_m^2}\,\frac{L_c N_c}{U_c}$$

Upon simplification, the equations become

$$F_v\,u_m\,(x_m,y_m) = \int_A \frac{(y'_m - y_m)\,\zeta_m\,(x'_m,\,y'_m)\,dx'_m\,dy'_m}{2\pi r_m^2} \tag{33}$$

$$F_v\,v_m\,(x_m,y_m) = \int_A \frac{(x_m - x'_m)\,\zeta_m\,(x'_m,\,y'_m)\,dx'_m\,dy'_m}{2\pi r_m^2} \tag{34}$$

where parameters are nondimensionalized as before.

The governing equations can then also be rewritten as

$$\frac{\partial \zeta_m}{\partial t_m} + \frac{\partial(F_v\,u_m\,\zeta_m)}{\partial x_m} + \frac{\partial(F_v\,v_m\,\zeta_m)}{\partial y_m} = \frac{F_v}{R_e}\,\nabla_m^2\,\zeta_m + \frac{\partial \rho'_m}{\partial x_m}$$

and

$$\frac{\partial \rho'_m}{\partial t_m} + \frac{\partial(F_v\,u_m\,\rho'_m)}{\partial x_m} + \frac{\partial(F_v\,v_m\,\rho'_m)}{\partial y_m} = F_v\,v_m\,n^2 + \frac{F_v}{R_e}\left(\nabla^2\rho'_m + \frac{\partial^2\overline{\rho}_m}{\partial y_m^2}\right)$$

where $F_v u_m$ and $F_v v_m$ are calculated directly using the nondimensionalized forms of the Biot-Savart Integrals equations (33) and (34).

37

The treatment of the governing differential equations in a stream function formulation is thus relatively straightforward. The complication is associated with the determination of the free surface location in conjunction with the solution of the governing equations, all preferably simultaneously, as noted by Yeung [Ref. 25].

Finite Difference methods are most suitable, or at least simplest to implement, for a boundary geometry that is rectilinear. The deformable free surface requires the use of "irregular stars" for difference schemes near the fluid boundary. These "irregular stars" are of an inferior accuracy when compared to the remainder of the grid. Thus, either the mesh must be refined or the difference formula changed to a higher order if accuracy is to be maintained near the free surface and especially in the vicinity of the scars. Yeung [Ref. 25] notes that, with the location of the free surface unknown a priori, we have the unfortunate situation that the regions that demand the greatest accuracy are precisely those where it is hardest to achieve. Also, since the shape of the free surface affects the migration of the vortex pair, a loss of accuracy in determining the free surface will be reflected in the determination of the location of the vortex pair. This complication is one not included in the investigations reviewed below where the generating body moves independently of the free surface location.

Conformal transformations can simplify one aspect of the problem by transforming the real geometry with a deformed free surface to a rectilinear mesh. The boundary conditions are thus simplified but the

38

resulting field equations are increased in complexity. Haussling and Coleman have successfully utilized transformation functions of this form to generate a time independent computational region in which nonlinear free surface boundary conditions are applied.

The Finite Difference method primarily benefits from the direct solution of the governing differential equations as opposed to the development of intermediate integral relations required in the integral boundary techniques. The cost of such an approach is in the computational intensity required to iteratively solve the finite difference forms over the computational domain. Haussling and Coleman have demonstrated the use of a successive over relaxation technique to solve steady state nonlinear free surface boundary condition problems as discussed above.

A modification of successive over relaxation, and one offering increased rates of convergence, has been demonstrated by Brandt, Dendy, and Ruppel [Ref. 26]. Their technique utilizes a multigrid solution which solves for low-frequency components of error on a course grid where the calculation is relatively inexpensive, and high-frequency components of error on a fine grid where successive over-relaxation is efficient.

Theodussiou and Sousa [Ref. 27] also utilized a modified grid system to speed convergence by staggering their grid structure such that pressure was defined at the center of the discretized control domain and velocity components were defined at the center of the control domain faces. This arrangement has the convenient feature that the

39

velocity components are stored at just the points at which they are required for the calculation of their advective contributions. The pressure gradients can be represented by central differences without inducing non-physical oscillations in the pressure distribution. Note, however, that both of these multigrid techniques add to the complexity of establishing a mesh which moves with the deforming free-surface. Both sets of authors suggest, however, that this added complexity is outweighed by the savings in ease of convergence.

Ohring [Ref. 28] and Ohring and Telste [Ref. 29] have also partially circumvented the computational intensity of an iterative technique by directly solving the finite difference equations resulting from the Laplace Equation. The technique employed utilizes a fourth-order solver to diagonally decompose the resulting coefficient matrix. Taylor series approximations are also suggested for application to the nonlinear free surface boundary conditions. It is suspected, however, that the computational benefits derived from such a technique will be lost when the coefficient matrix becomes nonlinear as would result from the governing equations in this problem.

For completeness, as noted previously, finite differencing in time is required for all the numerical methods reviewed. Sarpkaya and his students [Refs. 17-20] have successfully employed an upwind-differencing scheme in time and verified it with experimental results. Yeung notes that the free surface conditions, being first order in time, can be used to advance the solution of the elevation and velocity potential on the free boundary. However, the difference form utilized

can dramatically affect the stability and thus a modified Euler method is suggested since it is unconditionally stable. Haussling and Coleman successfully utilized this technique for advancing their solution in time.

C. FINITE ELEMENT METHODS

The Finite Element and Finite Difference methods share the common feature that both attempt to solve the governing differential equations directly, differing only in methodology. The Finite Element Method is one based on the method of weighted residuals. The usual procedure consists of first subdividing the domain of interest into a mesh of finite-sized subregions, within each of which the solution is represented by some convenient choice of trial functions, usually polynomials. The trial functions are determined by substituting them into the governing equations and requiring the integrated error or residual based on certain weighing functions to vanish. An integration by parts is normally preformed to reduce the interelement continuity requirements of the trial functions and to incorporate the nonhomogeneous boundary conditions. The weighing functions, also known as test functions, can be chosen in a variety of ways. A "weak formulation," such as the Galerkin Method, makes the space of the test functions identical to that of the trial functions. In contrast, a "strong formulation" is one based on the existence of a variational principle where a functional is made stationary. Specifics of finite element techniques may be found in Zienkiewicz [Ref. 30] and Dhalt and Touzot [Ref. 31].

The nonlinear aspects of this problem affect the Finite Element Method in much the same way as the Finite Difference Method. The coefficient matrix of a representation such as

[K] [U] = [B]

where

[K] = coefficient matrix

[U] = matrix of unknowns

[B] = forcing function matrix

is neither symmetric nor independent of [U], as in the case of a linear problem. An iterative technique is thus required to solve this problem at a given instance in time. As a result, much of the advantage of reduced storage and computation time inherent to finite element formulations is lost. The choice of iterative techniques does not differ from that available to Finite Difference Methods and, thus, once the computational domain is discretized, no significant difference in problem solution is involved.

The discretization of the computational domain is an area where the Finite Element Method does have distinct advantages. The introduction of curvilinear or isoparametric elements of higher order allows one to cope with any arbitrary boundary geometry with little loss of accuracy. Yeung notes that, although this particular advantage is reduced when Finite Difference Methods are used with conformal transformations, Finite Element Methods still retain superiority in flexibility, particularly in the case where varying size and shape elements are introduced to overcome local irregularities. Such

irregularities are exactly the problem involved in the vicinity of the deformable free surface. Curvilinear elements could be used to fit the free surface with finer elements incorporated in the vicinity of the scar front. This could be accomplished with little loss of accuracy and less complexity than that which results from the use of "irregular stars" in the Finite Difference Method. Note, however, that, since the scar front moves with time, an adaptive mesh refinement technique would be required to appropriately place the finer elements in the vicinity of the scar. Sarpkaya and Hiriart [Ref. 32] successfully utilized varying size elements in the vicinity of the free surface in conjunction with their moving net computation. Although the free surface in their case differed from that involved in this problem, the basic concept of a "flexible mesh" remains unchanged.

Admittedly, the basic problem of determining the location of the free surface in conjunction with solving the governing equations remains one of trial and error, regardless of the type of discretization employed. Larock and Taylor [Ref. 33] adjusted the free surface location to achieve tangency to the surface velocities calculated based on an assumed free surface position. The pressure boundary condition was then used as a check of this resulting location. Larock and Taylor note, however, that such a technique will not work well where high curvature or Froude numbers (F_v) less than one are involved, as is the case in the present investigation. As an alternative, Sarpkaya and Hiriart adjusted their free surface location to satisfy both the pressure and velocity boundary conditions simultaneously.

43

The Finite Element Method, when formulated using the variational techniques, also benefits from the fact that the boundary conditions may be included as an integral part of the functional rather than dealt with separately. Bai and Yeung [Ref. 34] and others have successfully employed variational techniques to directly incorporate boundary conditions in the solution of linear water wave problems.

D. BOUNDARY INTEGRAL EQUATION METHODS

The term "Boundary Integral Equation Method" can be applied to a large group of numerical techniques that include Green's Function formulations, Spectral Methods, and a boundary element application of the Finite Element Method. In all cases, the solution approach differs dramatically from that of Finite Differences and Finite Elements in that the governing equations are not attacked directly. Instead, the problem is solved by satisfying boundary conditions on a discretized boundary and thus reducing the spatial dimensions of the problem by one. Physical quantities such as wave height and fluid pressures are required and solved for only on the boundaries. Interior data, although available based on the boundary solution, is not specifically required. Boundary Integral Equation Methods thus have the distinct advantage that only the physical quantities specifically desired on the free surface are required for the solution.

Basically, there are two approaches to boundary integral formulations. Either an approximating function is chosen on the boundary that satisfies the governing equations in the domain and approximates

44

the boundary conditions, or vice versa. In both cases, the solution technique can be further divided into indirect and direct methods.

In indirect approaches, the fundamental solution is approximated on the boundary by a function with unknown coefficients. These coefficients are found by satisfying the boundary conditions. Distributed singularity methods, such as simple-source distributions, are an example of this approach. In this case, the fundamental solution is represented on a discretized boundary by distributed simple sources of unknown strength at known locations. The strength of each source is then determined based on the solution of the boundary conditions.

Direct methods find the fundamental solution through the use of Green's Function formulations, which directly incorporate the governing equations. The resulting Green's Function integrals are typically solved using quadrature or point kernel techniques. The main disadvantage in this approach is that, for the governing equations involved in this problem, there is no straightforward Green's Function formulation that leads to fundamental solution.

The main advantage of the Boundary Integral Equation Method is, then, the ability to directly discretize the free surface without a loss of accuracy. Information is thus obtained exactly where required. However, Brebbia [Ref. 35] notes that this is not without the sacrifice of a symmetric coefficient matrix such as that which is common to the Finite Element Method. Yeung notes that, in general, the great reduction in the size of the matrix outweighs the added complexity of solving a nonsymmetric system of equations.

The disadvantages of Boundary Integral Equation Methods are directly associated with errors that are the result of discretization. This discretization plays such a large role in the formulation of an efficient boundary integral equation that Brebbia refers to these techniques as "Boundary Element Methods." In all formulation techniques, elements of one type or another are formed over whieh a fundamental solution must be approximated either by distributed singularities, Green's Function integrals, or trial functions for finite elements.

Discretization errors result both from collocation errors and geometric surface errors. Collocation errors are primarily the result of leakage, as noted by Hunt [Ref. 36]. Since the boundary conditions are satisfied exactly only at discrete points, the remainder of the free surface is "porous" by comparison. Leakage errors are reduced by increasing the number of free surface elements and thus the number of discretization points. This, of course, is done at the expense of computational intensity. Geometric surface errors result from the approximation of a curved free surface by linear elements. This problem becomes particularly noticeable in areas of high curvature, such as scar fronts. Higgins and Cokelet [Ref. 37] noted that this problem can be partially circumvented by using a Lagrangian description of "marked" particles on the free surface. These particles tended to concentrate in the regions of highest curvature, thus giving improved accuracy exactly where needed.

46

Finite Element Method formulations using boundary elements only can also circumvent some of the errors associated with the collocation and geometric surface by using curvilinear or higher order parametric one-dimensional elements. The problem then is one of finding suitable fundamental solutions that satisfy both the governing equations and continuity requirements between elements.   -

Finally, Boundary Integral Equation Methods are complicated by the necessity to include nonlinear terms in the boundary condition for the free surface. As previously noted, this is necessary in order to maintain accuracy in the vicinity of the scar front where very small radii of curvature occur. Several researchers have successfully applied various forms of the Boundary Integral Equation Method to Laplace equations with linearized free surface conditions, but only a few have incorporated a nonlinear condition. Faltinsen [Ref. 38] incorporated nonlinear conditions by using the properties of the fluid particles on the free surface at one instance in time to establish a new free surface location and step the solution forward in time.

E. HYBRID METHODS

The use of a different technique in different portions of the computational domain results in a hybrid numerical formulation. This type of formulation attempts to maximize the benefits of any one particular method by employing it only in regions where its accuracy remains high. A secondary objective is to reduce the computational intensity of the overall routine by using a coarser, less time-intensive technique in areas where accuracy is not of particular concern. This is exactly the

case in the regions far removed from the free surface. The usual approach is to take advantage of the availability of analytical solutions in regions where the flow geometry is relatively simple. This approach allows the number of mesh points to be reduced with a resulting decrease in required storage and computational intensity. A further advantage is that the analytical solutions can be chosen to permit a simple solution of radiation type boundary conditions, as noted by Yeung [Ref. 25].

The disadvantages of Hybrid Methods are associated with the necessity to properly match the solutions of different subdomains in the overall computational domain. This matching may result in numerical perturbations to the solution technique if not properly employed. Additionally, the advantage of reduced total grid points is somewhat offset by the added computations required to match solutions at the common boundaries.

Yeung notes that "the more successful Hybrid methods have so far been restricted to linearized problems where analytical solutions in the exterior regions could be obtained without too much difficulty. In particular, treatment of steady flows in a uniform stream or time-harmonic flows with linearized boundary conditions have been quite well established." [Ref. 25]

Bai and Yeung [Ref. 34] utilized a finite element grid in the vicinity of the free surface and an eigenfunction solution in the exterior region to reduce the computational intensity of their routine. Chang and Pien [Ref. 39] used a source distribution to formulate a Boundary Integral

48

Equation Method near the free surface and a finite difference routine in the exterior regions to calculate the hydrodynamic forces on a body moving beneath a free surface. It should be noted, however, that both sets of investigators used a Laplace formulation with linearized boundary conditions to obtain their results.

For completeness, it is noted that Hybrid methods could be considered to include various numerical techniques that employ the same method throughout the computational domain but in different manners in each subdomain. Such is the case, for example, when a finite element method is employed with a varying grid and/or element type in various regions of the computational domain.

F. NUMERICAL METHODS, CONCLUSIONS, AND SELECTION

The synopsis of advantages and disadvantages for each numerical method listed in Table 1 provides a good source of information for making a wise choice of formulation to be used in this problem. The "best" method is one which will meet the goals of the investigation while maximizing the advantages in areas of particular concern.

In this case, accuracy in the vicinity of the free surface is of particular importance since ultimately it is the free surface shape which is desired. This accuracy must be obtained with full consideration of the necessity to include nonlinear boundary conditions while minimizing the computational intensity of an iterative process. Tuck, in a paper by Bai and Yeung, observed that "to a certain extent the 'best' method will always be that which appeals most to the person programming it, and hence that which gives him the greatest chance of

49

writing a successful program irrespective of efficiency. There is no less efficient program than one which does not work at all." [Ref. 34] Given that a successful program can be developed (a pretty big given), it is then necessary to maximize both efficiency and accuracy.

With full consideration of the concerns given above, the Boundary Integral Equation Method surfaces as the method of choice for the following reasons:

1. Computational intensity is minimized by reducing the spatial dimensions by one. This aspect is particularly noticeable when consideration is given to the iterative requirements of this problem. This substantial improvement directly incorporates any similar advantage that can be gained by using a varying Finite Element Method or Hybrid Method.

2. Accuracy is maintained at the free surface by incorporating the best aspects of Finite Element Methods and a Lagrangian description of marked particles. This direct discretization of the free surface provides both accuracy where needed most and an exact solution of boundary conditions at the marked points.

3. Storage requirements are drastically reduced since only physical quantities at the free surface are required or needed.

The implementation of the Boundary Integral Equation Method through the use of distributed vortices will be outlined in detail in the following section.

TABLE 1

COMPARISON OF NUMERICAL METHODS

Method	Advantages	Disadvantages
1. Finite Difference Methods	1. Well established and relatively straightforward formulation.	1. Requires the use of "irregular stars" or modified difference formulas in the vicinity of the free surface with a loss of accuracy.
	2. Method directly incorporates the governing differential equations.	2. Method is computationally intensive when employed with an iterative procedure, conformal transformations, or a multigrid structure.
	3. Can take advantage of conformal transformations to generate a rectilinear grid.	3. The boundary conditions are applied separately at discrete mesh points, potentially creating an additional loss of accuracy due to discretization.
2. Finite Element Methods	1. Direct incorporation of the governing differential equations.	1. The routine becomes computationally intensive when employed with an iterative procedure (nonlinear coefficient matrix.
	2. The boundary conditions can be included as an integral part of the formulation when employed with variational techniques.	

51

Method	Advantages	Disadvantages
2. Finite Element Methods (continued)	3. Method can deal with irregular boundary geometries with virtually no loss of accuracy and little or no discretization error if properly employed.	2. The coefficient matrix is non-symmetric, so may of the advantages of reduced storage and computational intensity common to finite element methods are lost.
		3. Adaptive mesh refinement would be required to maintain accuracy in the vicinity of the scar fronts.
3. Boundary Integral *Equation Methods*	1. The free surface can be directly discretized without a loss of accuracy, thus incorporating many of the advantages of Finite Element Methods in dealing with irregular geometries.	1. Fundamental solutions can be difficult or impossible to obtain when direct formulations are attempted.
	2. The spatial dimensions of the problem are reduced by one, resulting in reduced storage requirements and drastically reduced computational intensity.	2. The governing differential equations are not directly incorporated.
	3. Physical quantities are only required along the boundary where desired.	3. Discretization errors resulting from a "porous" free surface can reduce accuracy at the free surface if the discretization techniques are not properly employed.

52

Method	Advantages	Disadvantages
3. Boundary Integral Equation Methods (continued)	4. Lagrangian description of marked particles on the free surface tends to "automatically" adjust discretization to a finer grid in the regions of higher curvature where needed. Thus, adaptive mesh refinement occurs based on the physical problem development with no required operator intervention. 5. Boundary conditions can be solved exactly on a discretized free surface.	4. The incorporation of nonlinear free surface boundary conditions increases the computational intensity in a manner similar to that of Finite Element Methods and Finite Difference Methods.
4. Hybrid Methods	1. Can employ each method in regions where its inherent accuracy is the best. 2. The computational intensity can be reduced by using a coarser system in the regions where high accuracy is not required. 3. Analytical methods, when applicable, can simplify radiation-type boundary conditions.	1. Continuity between techniques is limited and can result in the generation of non-physical perturbations. 2. There has been only limited use by previous investigators studying nonlinear free surface flows. 3. Accuracy of a given technique may be reduced when employed in conjunction with other formulations.

53

IV. **DISTRIBUTED VORTEX MODEL**

A. INTRODUCTION

Discrete vortices, with or without a core, or vortex sheets have been used as boundary elements to simulate separated and unseparated flows. The method consists of the determination of the appropriate strength of the vortices at each time interval through the use of the governing equations. The vortices are then convected to their new positions and the process is repeated. In spite of its simplicity, the distributed vortex model presents several difficulties, all of which are related to discretization and the use of vortices. The evaluation of the governing integral equation cannot accurately be accomplished merely by applying a standard integration formula. A vortex sheet or a string of point vortices is unstable to small sinusoidal disturbances of any wavelength. This phenomenon of Helmholtz instability persists in curved nonuniform vortex sheets, at least for short waves, unless the sheet is rapidly stretching. In other words, the round-off and truncation errors are rapidly amplified to cause the chaotic motion which often ruins practical calculation. If it is granted that it is the growth of short waves which can ruin calculations with vortex sheets, it is sensible to consider ways of removing the instability. This is because the instability is introduced by the step of replacing a shear layer of small, but finite, thickness by a vortex sheet. One could give up the vortex sheet approximation and return to the computation of the evolution of

54

a thin layer. This is without doubt the most satisfactory procedure, but it involves much more computation.

An alternative approach is to modify the governing differential equation to allow for finite thickness but the resulting equation, while only a little more complicated than the original equation, has not proved amenable to computation.

Another possibility is to apply a linear smoothing formula, such as that introduced by Longuet-Higgins and Cokelet [Ref. 37] in their work on nonlinear water waves. The subsequent applications, including the one discussed herein, have shown that chaotic motion sets in sooner or later regardless of the smoothing. The repositioning technique introduced by Fink and Soh [Ref. 40] and used subsequently by Sarpkaya and Shoaff [Ref. 41] removes the most unstable mode and reduces the growth of the higher modes of Helmholtz instability. However, it does not prevent the growth of spurious waves along the vortex sheet. The disadvantage of the smoothing, either through the use of a numerical filter or through the repositioning of the vortices, is that it is not clear in general what the relationship is between the results achieved and the unknown exact solution. The problem may not possess a solution for all time, and in this case the use of smoothing could yield an acceptable-looking solution where none in fact exists. Alternatively, the solution arrived at through smoothing may not be even close to the exact solution.

B. APPLICATION OF THE DISTRIBUTED VORTEX METHOD

The liquid surface was represented by a number of point vortices. Their positions were symmetrical with respect to the x axis, situated on the free surface. However, the strength of a vortex at (x, y, normalized by b_0) was opposite to that of a vortex (image vortex) at (-x, y). From a mathematical point of view, one would like to have the vortices extend from $-\infty$ to $+\infty$ and the two trailing vortices originate at (1/2, $-\infty$) and at -1/2, $-\infty$). This is impossible from a numerical point of view. Observations have shown that the free surface rises in a relatively small region directly above the trailing vortices. The remainder of the free surface remains undisturbed. These observations and several sample calculations led to the conclusion that the free surface can be restricted to a region extending from x = -10 to x = +10. Furthermore, the trailing vortices are assumed to originate at a depth of y = -5.

The complex function representing the two trailing vortices below the free surface and the vortices on the free surface is given by

$$ w = - \frac{i\Gamma_o}{2\pi} \ln (z - z_0) + \frac{i\Gamma_o}{2\pi} \ln (z + \overline{z}_0) + \frac{i\Gamma_m}{2\pi} \ln (z - z_i) $$

$$ - \frac{i\Gamma_m}{2\pi} \ln (z + \overline{z}_i) $$

in which the strengths of the free-surface vortices are normalized by the strength of the trailing vortex. All coordinates are normalized by b_0. Then the velocities, normalized by $V_0 = (\Gamma_0/2\pi b_0)$ anywhere in the fluid medium is given by

$$u - iv = \frac{dw}{dt} = -\frac{i\rho_0}{2\pi}\frac{1}{(z-\bar{z}_0)} + \frac{i\rho_0}{2\pi}\frac{1}{(z+\bar{z}_0)} + \frac{i\Gamma_m}{2\pi}\frac{1}{(z-z_1)} - \frac{i\Gamma_m}{2\pi}\frac{1}{(z+\bar{z}_1)} \quad (35)$$

The normalized boundary condition at the free surface is given by

$$\frac{D\varnothing_m}{Dt_m} - \frac{q_m^2}{2} + \frac{\eta_m}{F_v^2} = 0 \quad (36)$$

Thus, at least theoretically speaking, one can calculate the potential function $\varnothing$ from the complex velocity potential w (the real part of w), the velocity of the vortices from equation (35), the elevation of the free surface from equation (36) for a given Froude number Fv (Fv = $V_0/\sqrt{gb_0}$), and trace the evolution of the free surface as a function of time. This relatively simple–sounding procedure is anything but simple, primarily because of the fact that the numerical instabilities eventually lead to large–scale instabilities, as noted in the introduction to this section. The use of various smoothing techniques was a viable option and, in fact, was tried at various stages of the calculations. The results have shown that the growth of the instabilities increases with decreasing Froude number. Neither the use of smoothing techniques (e.g., the Longuet–Higgins technique) nor the use of vortex sheets, vice discrete vortices, can eliminate the eventual development of a chaotic behavior on the free surface. It is because of this reason that the use of smoothing was ruled out and the calculations were restricted to a relatively high Froude number (Fv = 1.125).

The specific details of the numerical calculations are as follows: (1) assign the position of the vortices; (2) find the strength of the vortices and the velocity potential assuming the free surface to be rigid;

(3) advance the position of the trailing vortices for a time interval t (0.01 in the calculations); (4) recalculate the velocity of the surface vortices and advance them forward in time for a time interval t; (5) calculate the strength of the free surface vortices by iteration until the free surface condition is satisfied; (6) calculate the velocity of the surface and trailing vortices and advance their positions for a time interval t; and (7) repeat the calculations by returning to step (5).

The procedure described above is relatively simple and does not require excessive computer time (about 20 minutes on IBM 3033). However, the free surface eventually does become chaotic. Some of the instabilities can be alleviated without smoothing through a judicious selection of the initial position of the surface vortices. Numerous calculations have shown that the vortices near the y axis begin to slide sideways as the free surface (or the vortex sheet) stretches. Consequently, the thinly populated regions of the sheet do not yield a smooth free surface and the flow begins to leak between the vortices. Also, the regions where the free surface is depressed (where the scars develop) become overpopulated with vortices, leading to the growth of short-wavelength Helmholtz instability. This problem can easily be alleviated by packing the vortices more densely near the y axis at the start of the calculations so that the entire surface becomes more or less uniformly represented at later times. This simple technique has been used in the results presented herein. An exponential function was employed to assign the initial vortex spacings so that near the

y axis the vortices were separated by a distance of about 0.03 and by a distance of about 0.25 towards the end of the vortex sheet.

C. RESULTS OF THE NUMERICAL CALCULATIONS

The evolution of the free surface with time is shown in Figures 2.1 through 2.27 for Fv = 1.125. The normalized time in these plots is given by $T = (V_0 t/b_0 - d_0/b_0)$ where d_0 is the initial depth of the trailing vortices. The time $T = 0$ corresponds to that at which the trailing vortices would have reached the undisturbed free surface had they continued to move with their initial mutual induction velocity. The use of other normalized times is not suitable since they tend to depend on the initial position of the trailing vortices.

Figures 2.1 through 2.27 show that the free surface directly above the vortices rises rapidly while the adjacent portions of the surface depress and form two strong scars. Unlike the rigid surface case, where the trailing vortices continue to move towards right and left at a depth of about y = −0.5, the trailing vortices below the deforming surface almost come to rest at a point slightly above the free surface. Furthermore, their initial spacing remains nearly constant. This suggests that the Kelvin oval formed by the trailing vortices pushes the free surface up as if it were rigid during its upward migration. Evidently, this finding is based on the assumption that the trailing vortices are point vortices and are not subjected to viscous and turbulent diffusion. In reality, the vortices quickly become turbulent, their core radius increases, and the vorticity is diffused over an ever-increasing area with the passage of time. The amount of diffusion depends on the

initial position of the trailing vortices. Consequently, the trailing vortices emanating from large depths diffuse over a larger area relative to those emanating from smaller depths. There is at present no suitable mathematical means to deal with the turbulent diffusion of such vortices. The best one can do is to generate the trailing vortices at depths sufficiently close to the free surface to prevent excessive diffusion and yet sufficiently far so that the free surface remains undeformed at the start of the motion. Extensive calculations and experimental observations have shown that the free surface does not begin to deform until the trailing vortices reach a depth of about $y = -1$. Thus, it is perfectly safe to place the trailing vortices at $y = -3$ at the start of the calculations.

V. EXPERIMENTS

A. EXPERIMENTAL APPARATUS AND PROCEDURES

Experiments were conducted in a water basin. It consisted of a 12-foot-long, 3-foot-wide tank with aluminum bottom and plexiglass walls (see Figure 3). Additional equipment consisted of plumbing for the filling and emptying of the tank, a collimated light source, and the dye system for flow visualization.

The two-dimensional trailing vortices were generated through the use of two counter-rotating plates (see Figure 3). The mechanism rotating the plates was located at the bottom of the tank and below a plexiglass plate spanning the entire tank. In other words, the motion of the driving system did not disturb the flow above the plexiglass. The mechanism was actuated by releasing a weight attached to the common driving shaft. Fluorescent dye was introduced slowly into the region between the plates through the use of two holes connected to two dye reservoirs. The reason for the use of two reservoirs was that different colors of dye can be used to visualize each trailing vortex.

B. PROCEDURES

Experiments were initiated by filling the tank to a suitable level, removing any air bubbles, bringing the plates to their full open positions, waiting for a sufficient period of time for the fluid to come to rest, introducing the neutrally buoyant dye, actuating the light source

and the video system, and initiating the rotation of the plates by suddenly releasing the load attached to the driving shaft. The plates rotated smoothly and then came to rest on the plexiglass. In other words, the plates generating the vortices literally "disappeared." Thus, no other vortices were generated. It is a well-known fact that this is not the case with piston-generated vortices. When the piston stops, two additional vortices (from a two-dimensional piston) or another vortex ring (from an axisymmetric piston) are generated. The mechanism used in the present investigation effectively prevents the generation of secondary vortices by simply disappearing.

The trailing vortices rise under their mutual induction velocity, quickly give rise to a Kelvin oval, and smoothly approach the free surface. When the vortices are at a distance of about 1.0 from the free surface, the free surface begins to rise and forms a smooth hump, bordered by two scars. For the Froude numbers achievable (maximum 0.35), the trailing vortices turn quickly to right and left (as if they were approaching a rigid surface), the scar front moves in the respective directions ahead of the vortex, and the hump between the vortices begins to recede. During the later stages of the motion, the scars are slaved to the vortices and continue to move ahead and in the direction of the vortices.

Figures 4.1 through 4.12 show the evolution of the free surface at various times T for a Froude number of Fv = 0.35. The vortex centers are clearly visible in these pictures because of the additional assistance provided by the dissolved air bubbles to the flow visualization efforts.

VI. DISCUSSION OF RESULTS

The computer code based on the boundary element methods through the use of the discrete vortices has been used to carry out calculations for various Froude numbers in order to predict the evolution of the free surface deformation. The type of the vortex distribution. time increment. and the iteration techniques have been varied within limits to explore the differences in the motion of the free surface. The results have shown that the calculations are fairly stable at relatively high Froude numbers. However. at relatively small Froude numbers. the Kelvin–Helmholtz instability sets in quickly and the free surface exhibits highly irregular shapes. It appears that either the integration procedures have to be refined or more sophisticated vortex sheets have to be used to calculate the small deformation of the free surface at small Froude numbers.

The results obtained with a Froude number of $F_V = 1.125$ are shown in Figures 2.1 through 2.27. The most striking feature of these results is that the free surface rises rapidly to a height of about 1.25 above the mean water level and captures the vortex pair. It has not been possible to carry out the calculations to larger times. The fact should be kept in mind that the point vortices used in the numerical calculations may have very little resemblance to the real vortices by the time they rise to the mean water level. In fact. the experiments

show that the vortices become quickly turbulent. There is at present no possibility of incorporating into a numerical analysis the motion of a turbulent vortex.

Experiments were carried out at a maximum Froude number of 0.35. The evolution of the free surface is shown in Figures 4.1 through 4.12. The shape of the free surface at the time of maximum rise is plotted in Figure 5. Figures 4 and 5 show that the free surface rises to a maximum height of about 0.25, develops two strong scars, and then subsides as the vortices begin to move parallel to the free surface. The scar front is slightly ahead of the vortex center and reduces to a small depression at larger times. The results presented in Figures 4 and 5 should form the basis of comparison for future numerical efforts at the corresponding Froude numbers. Additional calculations are underway with more sophisticated vortex sheets. The results presented herein are extremely encouraging and are expected to lead to a better understanding of this extremely complex and challenging phenomenon.

VII. CONCLUSIONS

The investigation reported herein warranted the following conclusions:

1. The basic equations governing the motion of vortices in homogeneous and density-stratified media have been developed and expressed in terms of dynamic and buoyant scaling laws;

2. A novel experimental technique has been devised to generate a nearly two-dimensional vortex pair rising toward a free surface;

3. Migration of a vortex pair toward a free surface gives rise to a bulge and two scars;

4. The maximum rise at the free surface occurs when the vortex pair is at a depth of about 0.5;

5. In the range of Froude numbers encountered in the experiments, the rise of the free surface is always followed by a fall as the vortices begin to move parallel to the free surface at large times;

6. The numerical analysis of the free surface deformation through the use of discrete vortices leads to instabilities at low Froude numbers. These instabilities could have been removed with a suitable numerical filter or smoothing technique. However, the use of a relatively subjective smoothing procedure has been ruled out. The calculations at a Froude number of 1.125 have yielded fairly stable solutions and provided the basis for comparison with future experiments.

$$\frac{\partial \eta_m}{\partial t_m} + F_v \, u_m \frac{\partial \eta_m}{\partial x_m} = F_v v_m \quad \text{at} \quad y_m = \eta_m$$

$$\frac{\partial \varnothing_m}{\partial t_m} + F_v^2 \, \frac{q_m^2}{2} + \eta_m = 0 \quad \text{at} \quad y_m = \eta_m$$
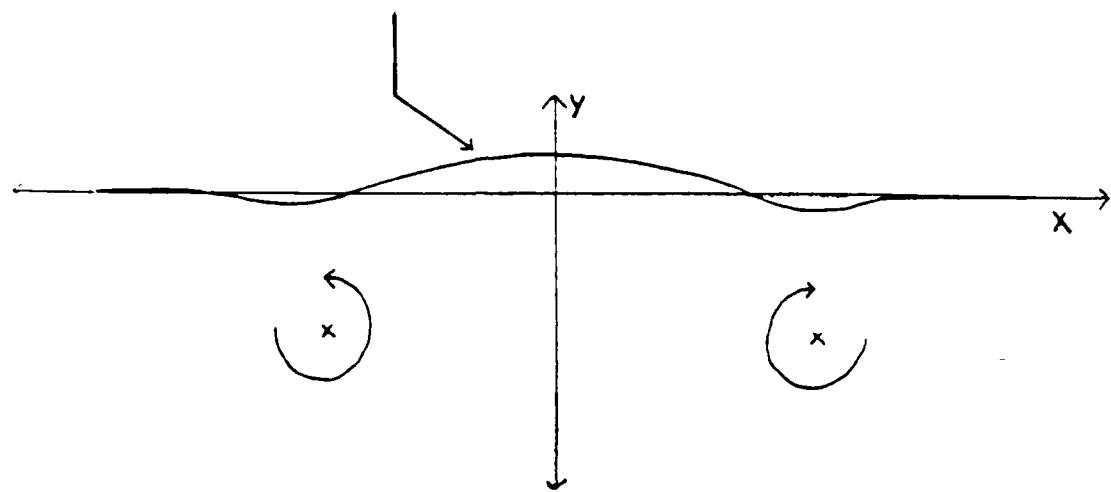
$$\frac{\partial \zeta_m}{\partial t_m} + F_v \left[\frac{\partial(u_m \zeta_m)}{\partial x_m} + \frac{\partial(v_m \zeta_m)}{\partial y_m} \right] = \frac{F_v}{R_e} \nabla^2_m \zeta_m + \frac{\partial \rho'_m}{\partial x_m}$$

$$\frac{\partial \rho'_m}{\partial t_m} + F_v \left[\frac{\partial(u_m \rho'_m)}{\partial x_m} + \frac{\partial(v_m \rho'_m)}{\partial y_m} \right] = F_v n^2 v_m + \frac{F_v}{R_e} \left(\nabla^2_m \rho'_m + \frac{\partial^2 \bar{\rho}_m}{\partial y_m^2} \right)$$

Figure 1.   Computational Domain, Governing Equations, and Boundary Conditions

66

$$T^{*} = -2.40000$$
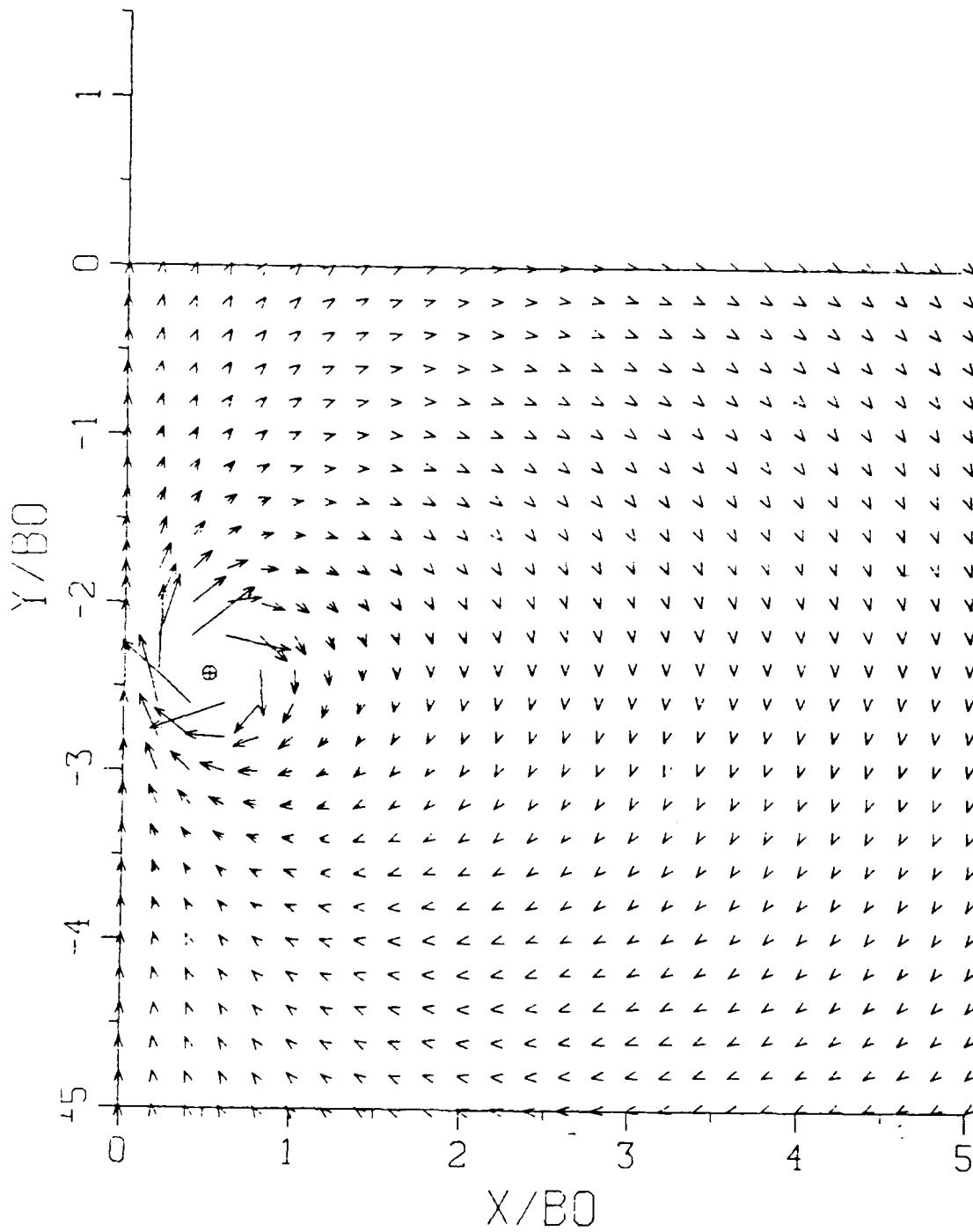
Figure 2.1   Velocity Field for T^{*} = -2.40

67

$$T^* = -2.30000$$
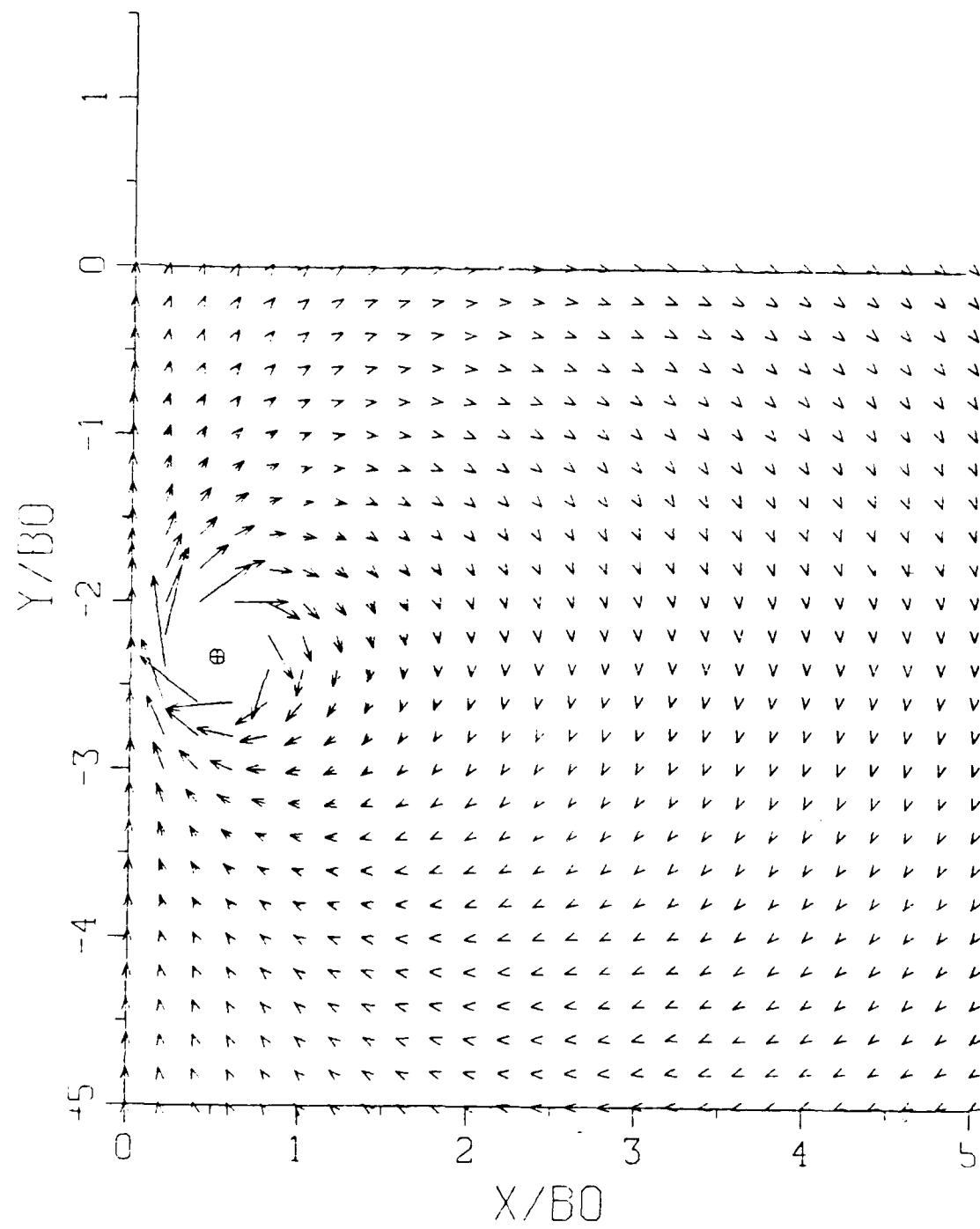
Figure 2.2   Velocity Field for $T^* = -2.30$

$$T^{\times}= -2.20000$$
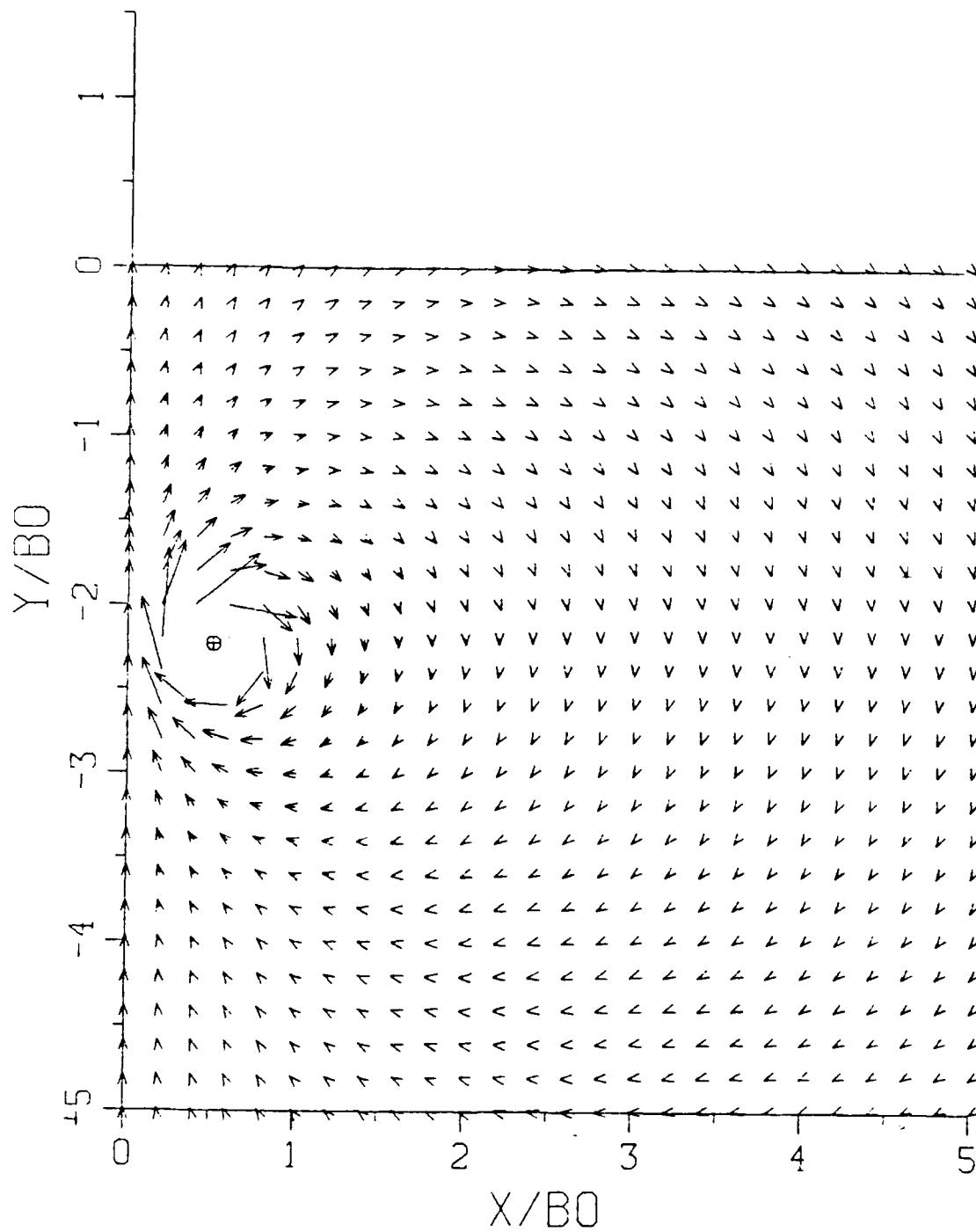
Figure 2.3   Velocity Field for T* = -2.20

69

$$T^* = -2.10000$$
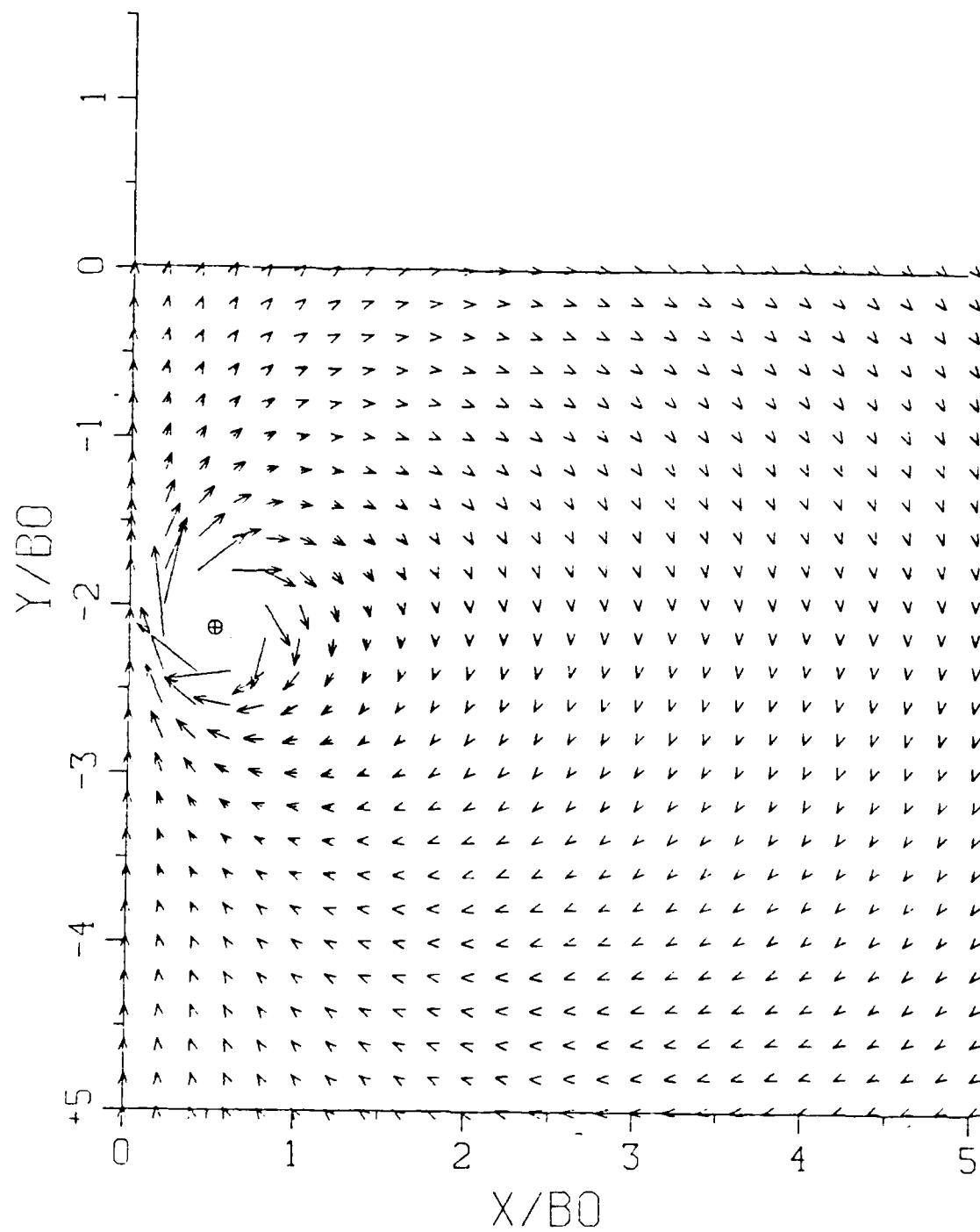
Figure 2.4   Velocity Field for $T^* = -2.10$

$$T^{*} = -2.00000$$
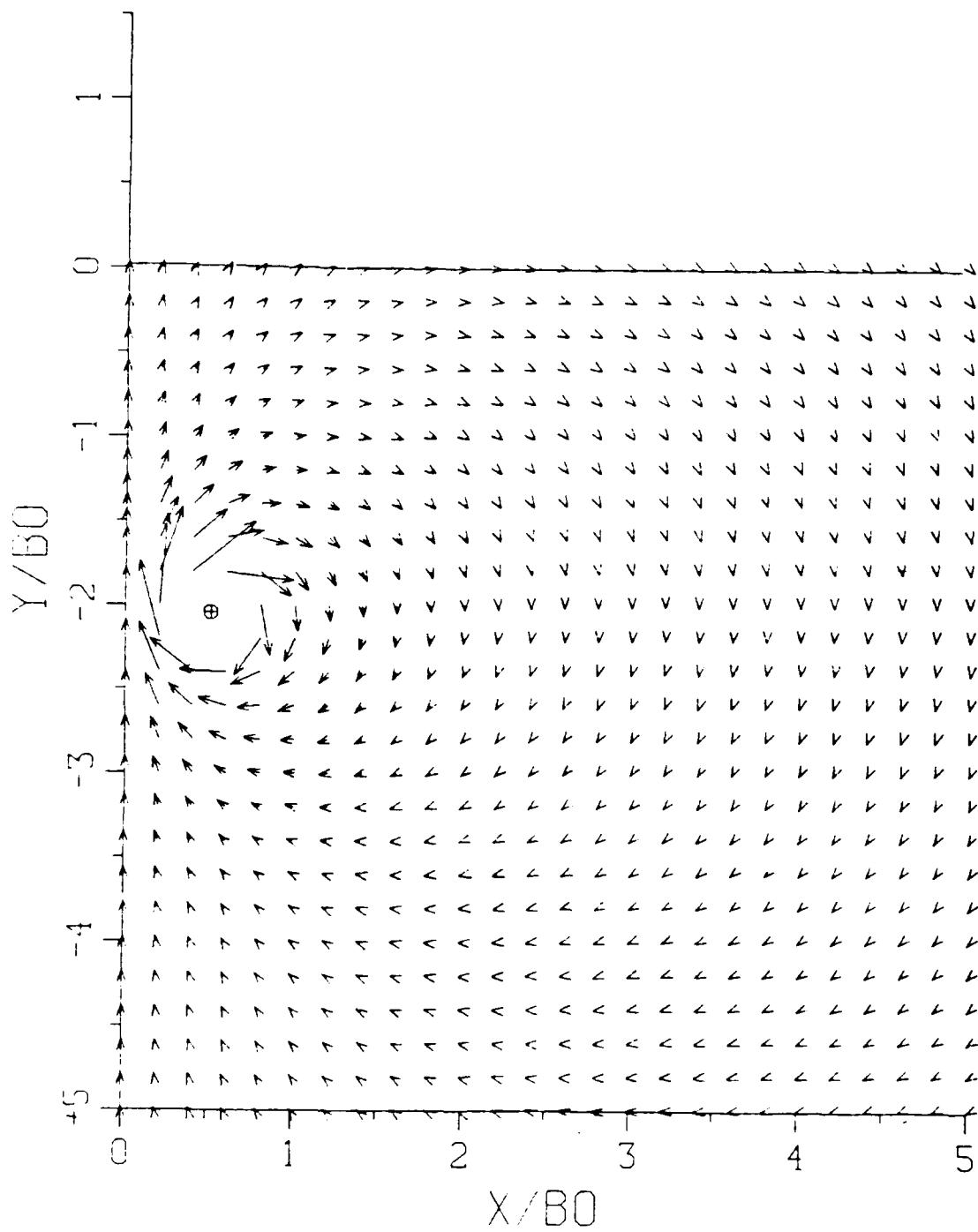

Figure 2.5   Velocity Field for $T^{*} = -2.00$

71

$$T^{\times} = -1.90000$$
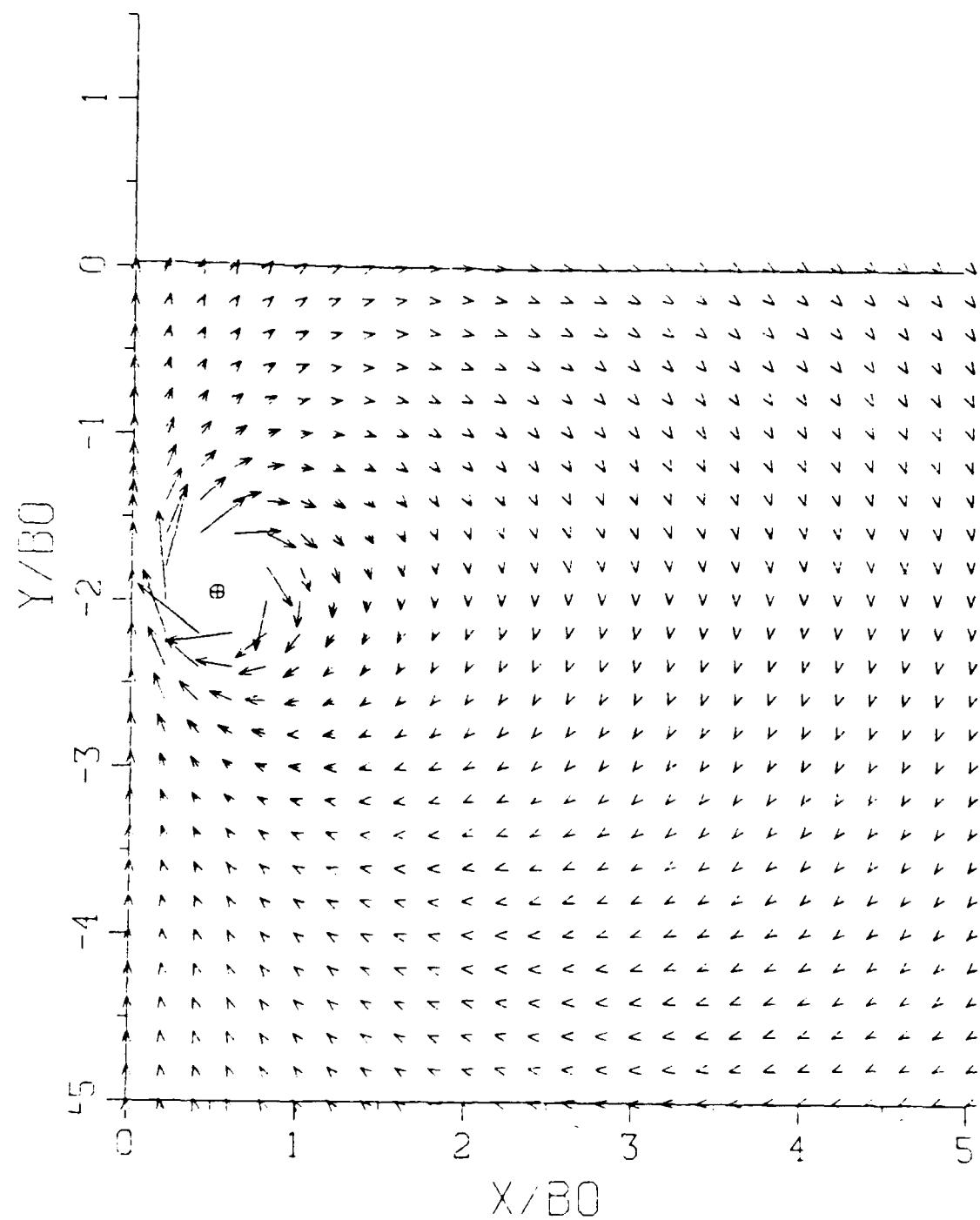
Figure 2.6   Velocity Field for T* = -1.90

$$T^* = -1.80000$$
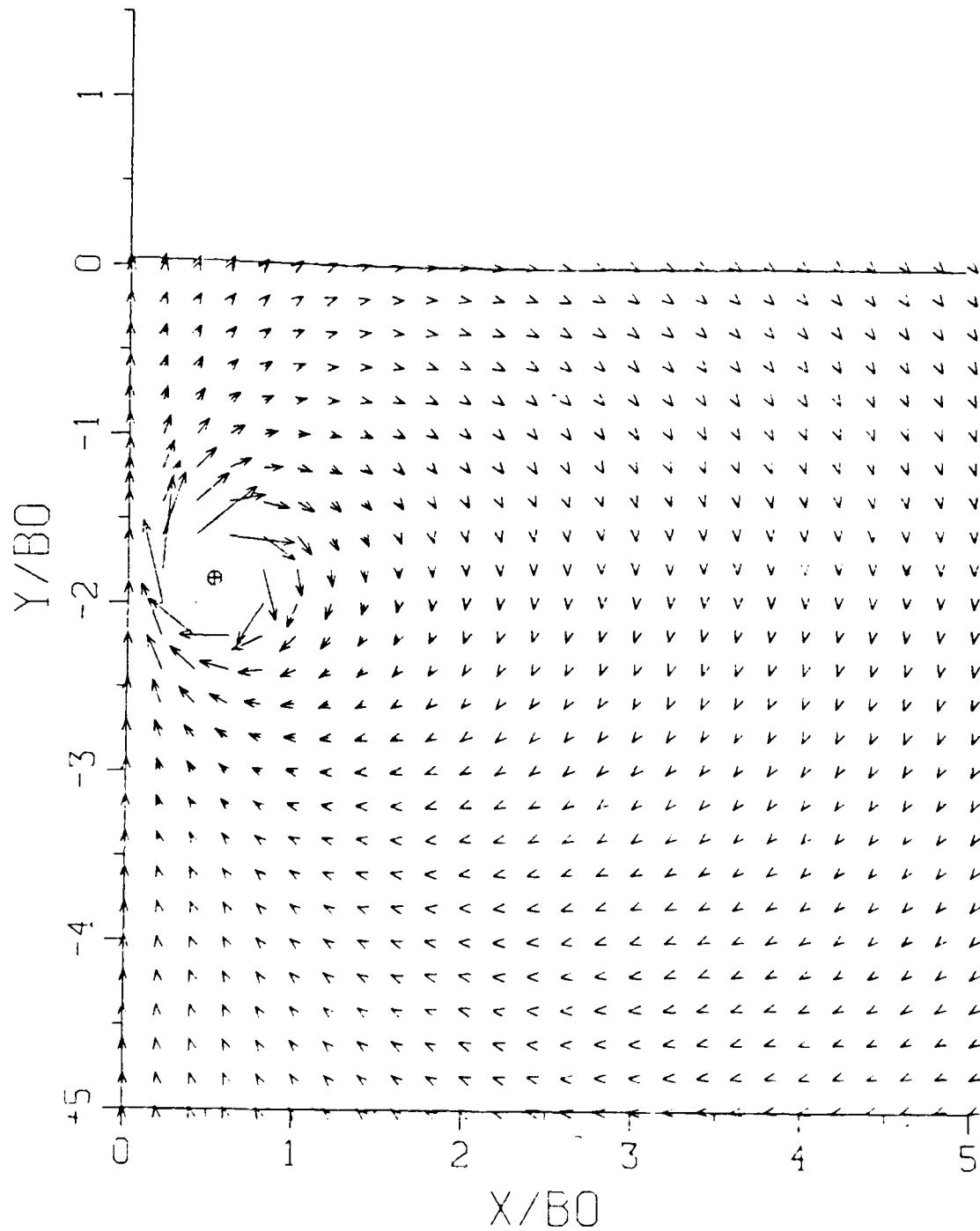
Figure 2.7   Velocity Field for $T^* = -1.80$

73

$$T^* = -1.70000$$
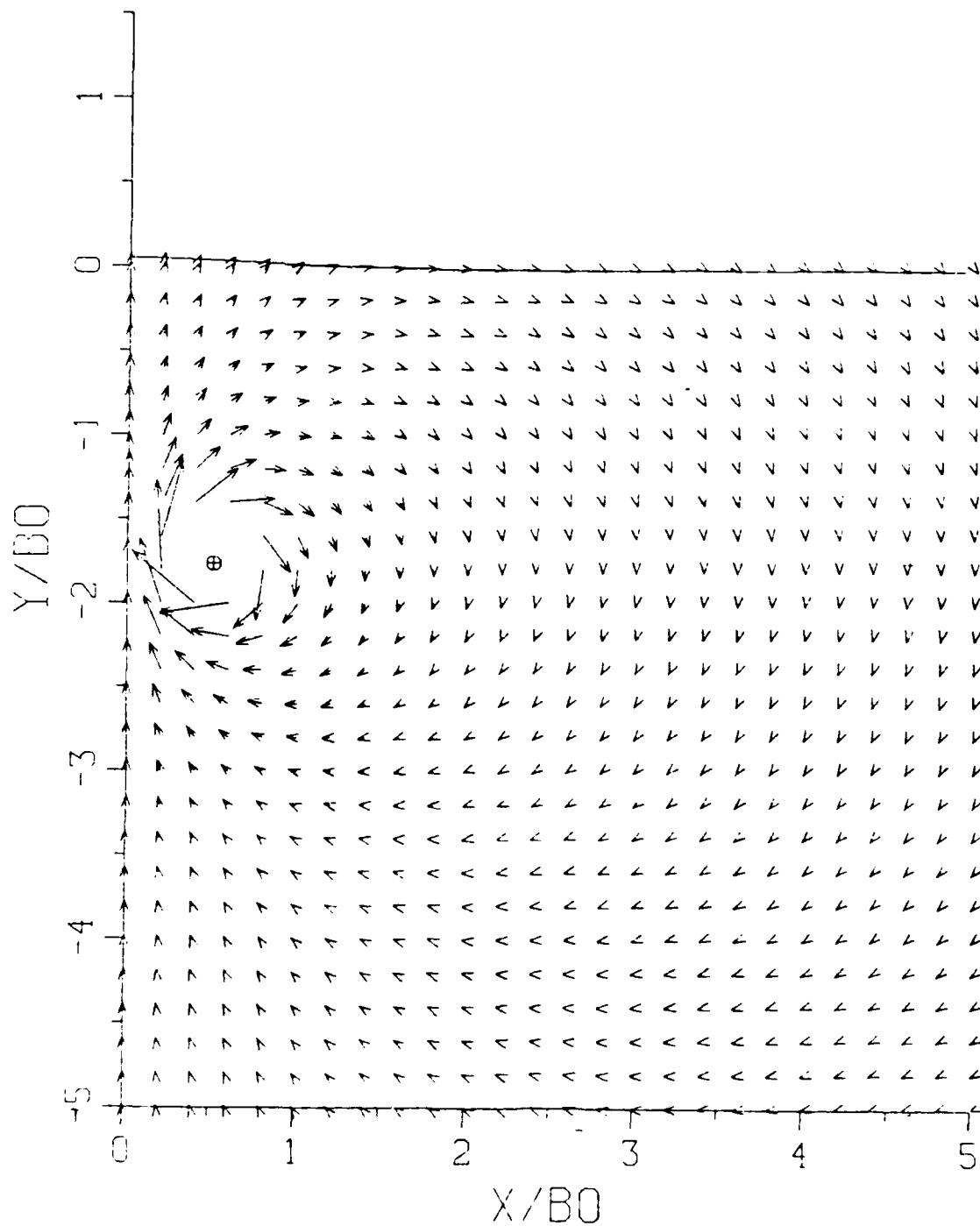
Figure 2.8   Velocity Field for $T^* = -1.70$

74

$$T^* = -1.60000$$
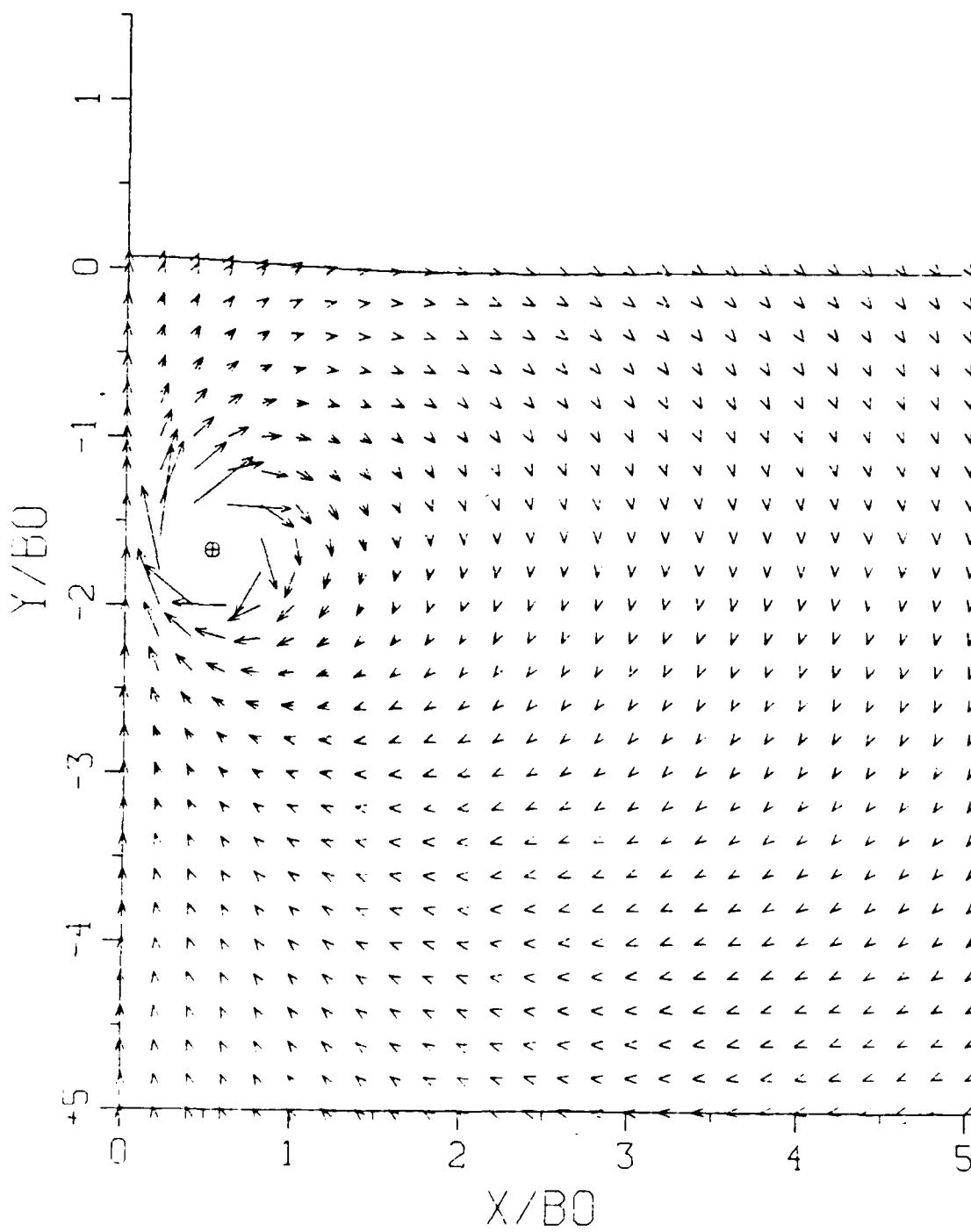
Figure 2.9 Velocity Field for $T^* = -1.60$

$$T^* = -1.50000$$
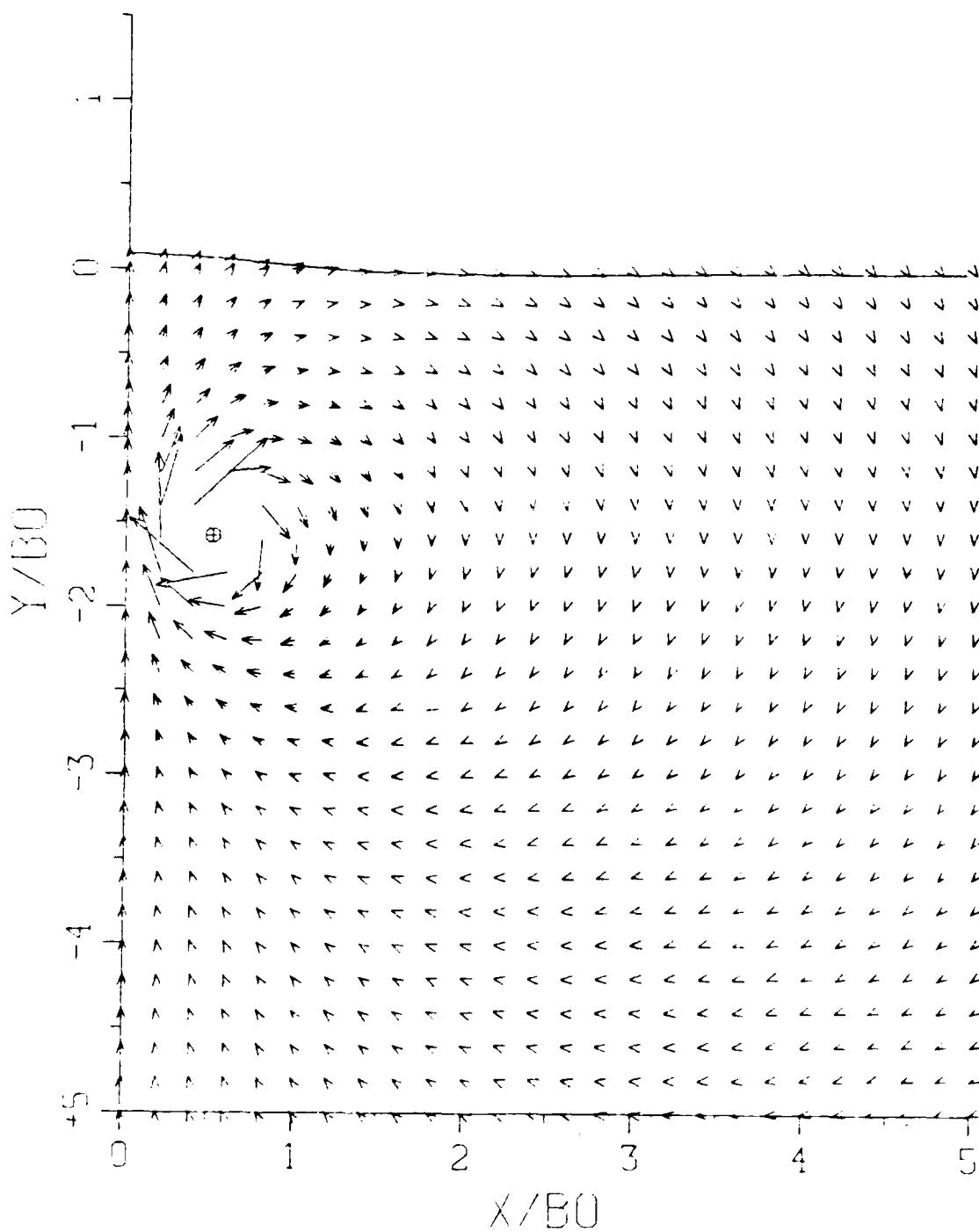
Figure 2.10 Velocity Field for $T^* = -1.50$

$$T^* = -1.40000$$
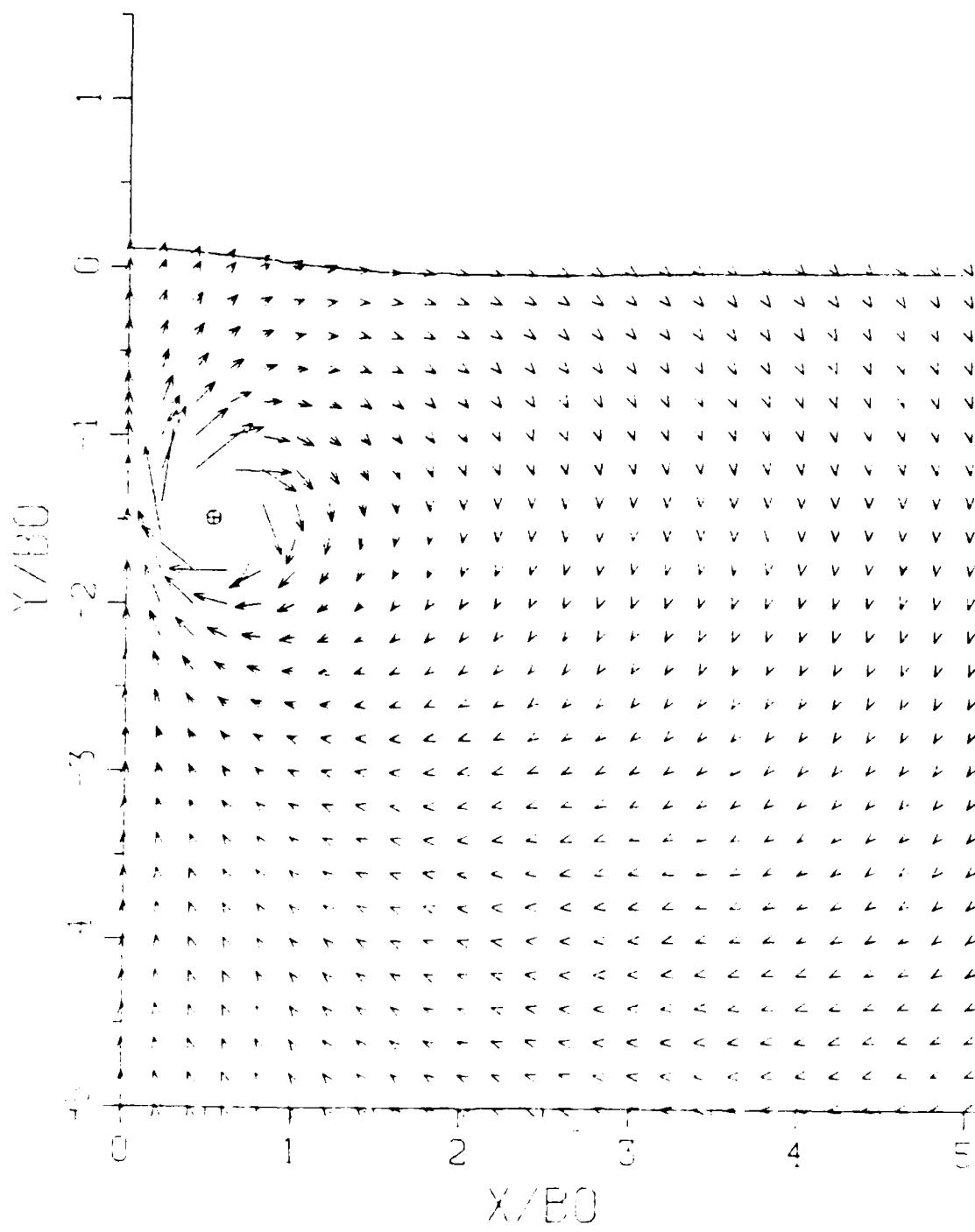
Figure 2.11 Velocity Field for $T^* = -1.40$

$$T^* = -1.30000$$
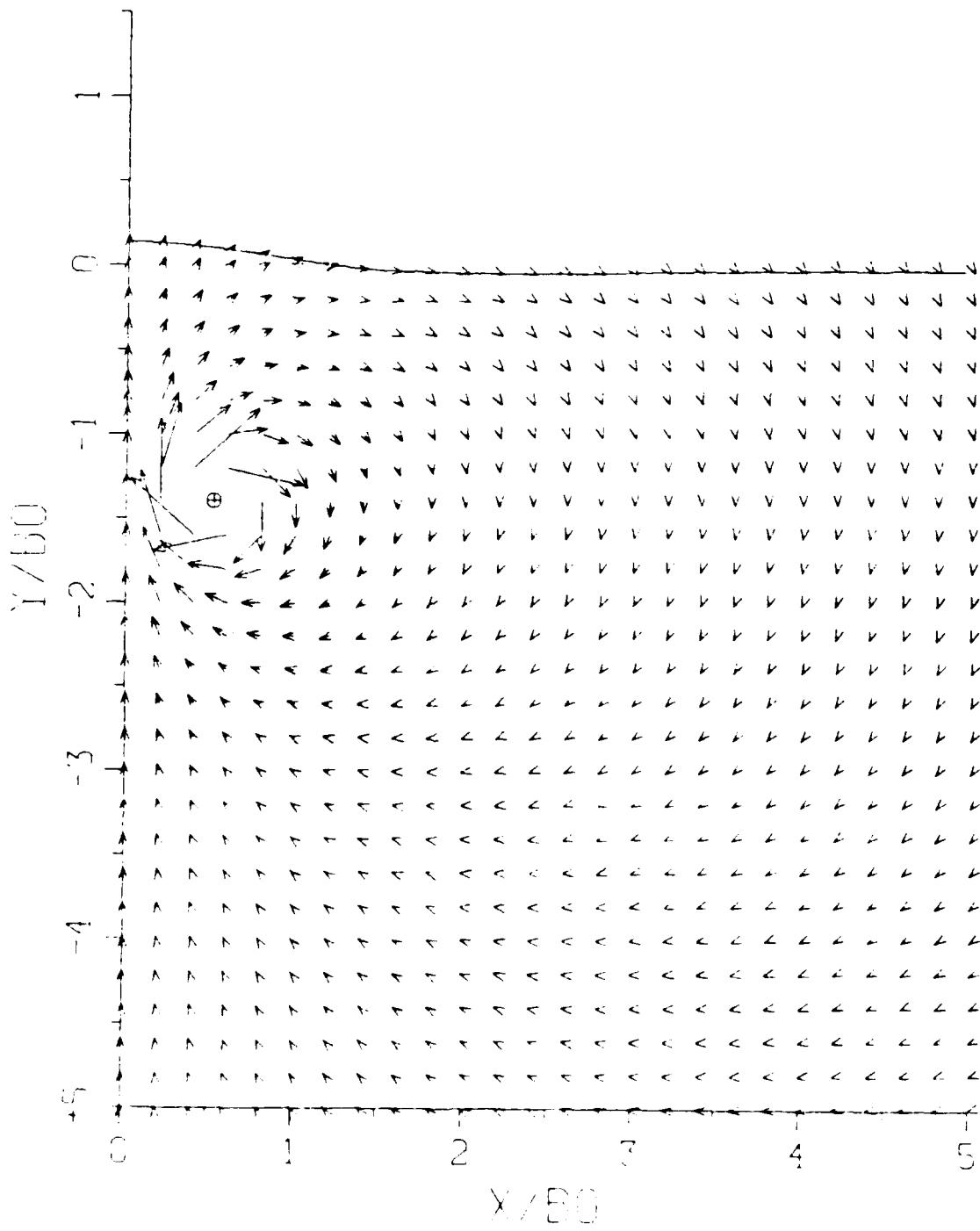
Figure 2.12 Velocity Field for T* = -1.30

$T^* = -1.20000$
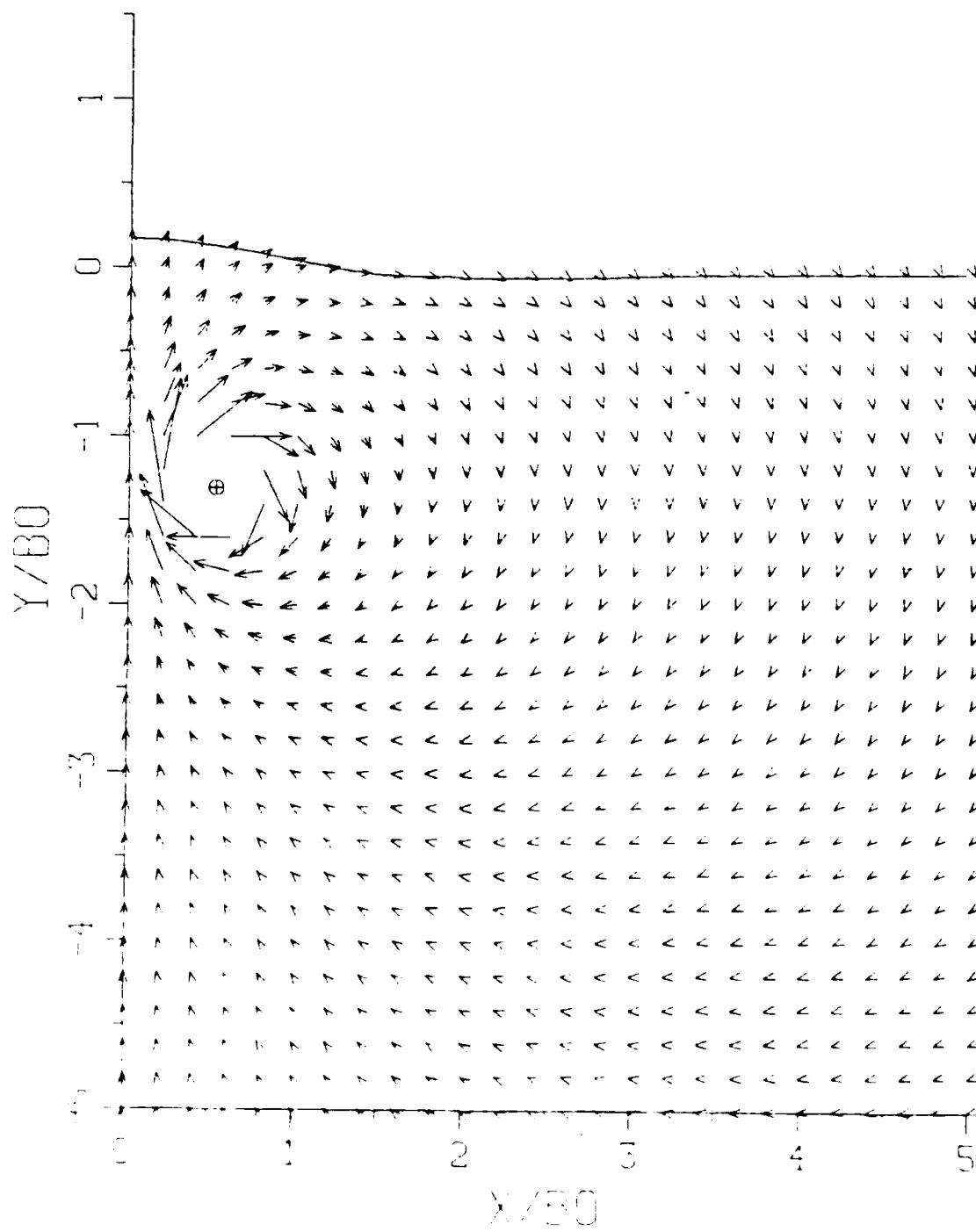
Figure 2.13 Velocity Field for $T^* = -1.20$

$$T^* = -1.10000$$
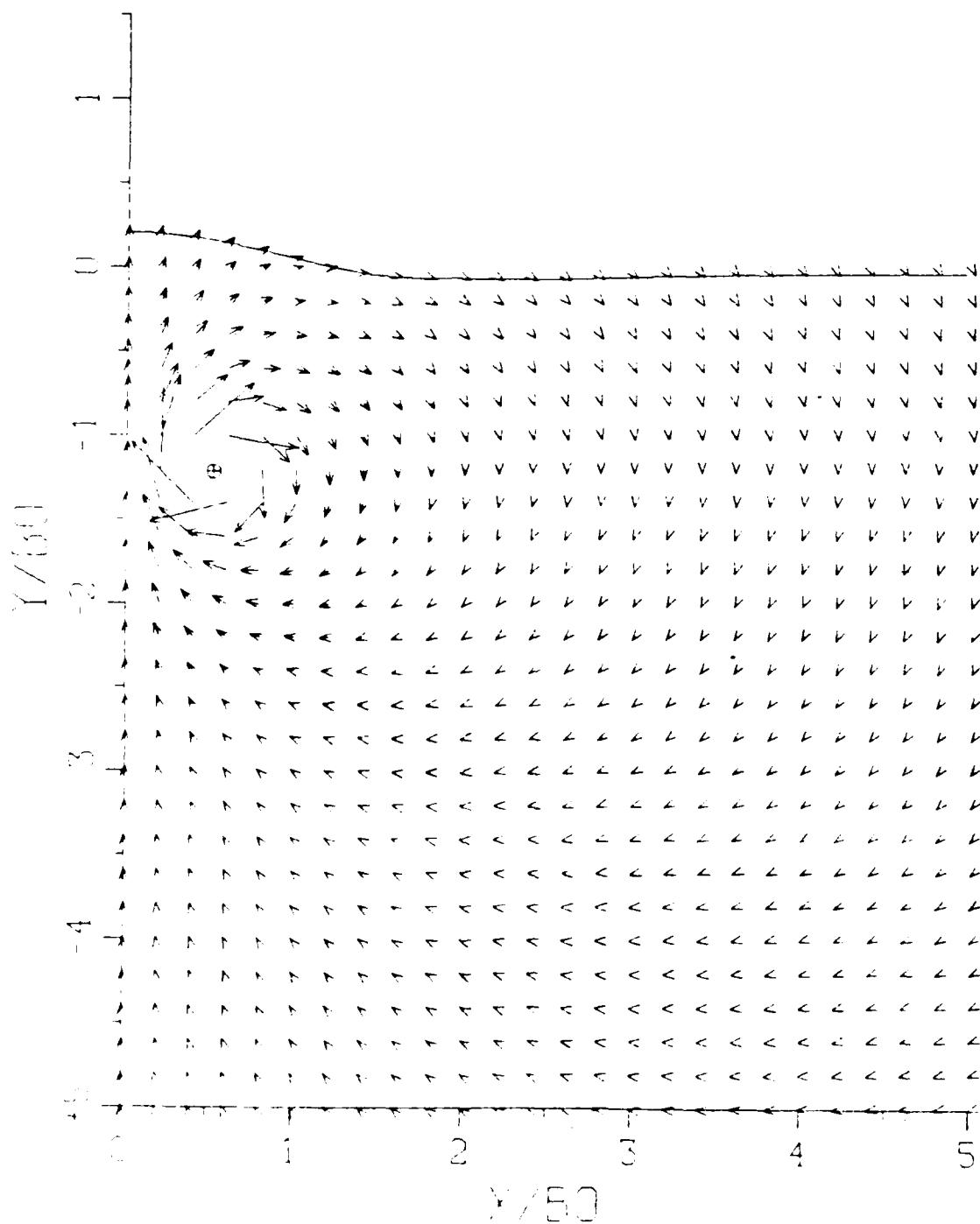
Figure 2.14 Velocity Field for T* = -1.10

$$T^* = -1.00000$$
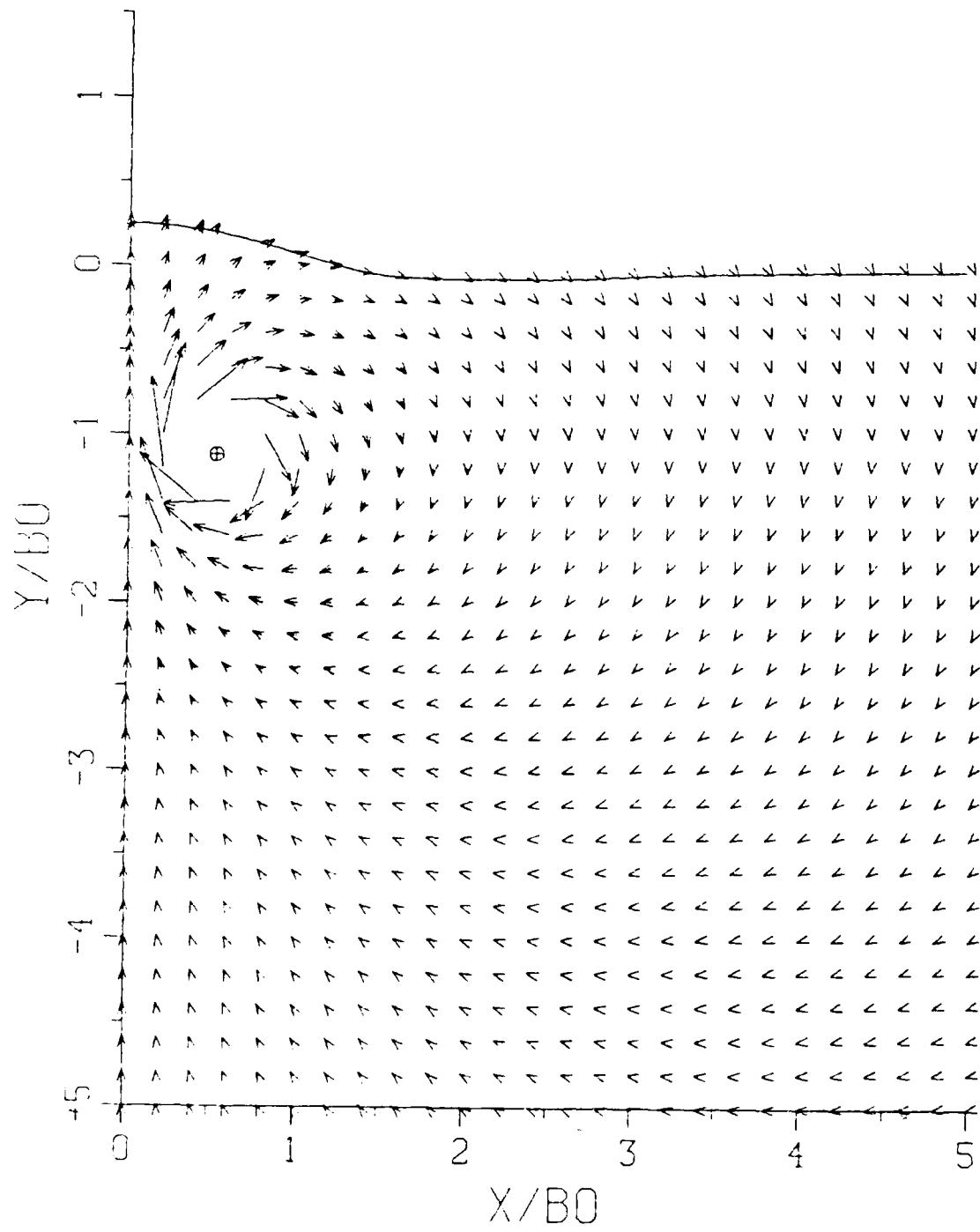
Figure 2.15 Velocity Field for T* = -1.00

$$T^* = -0.90000$$
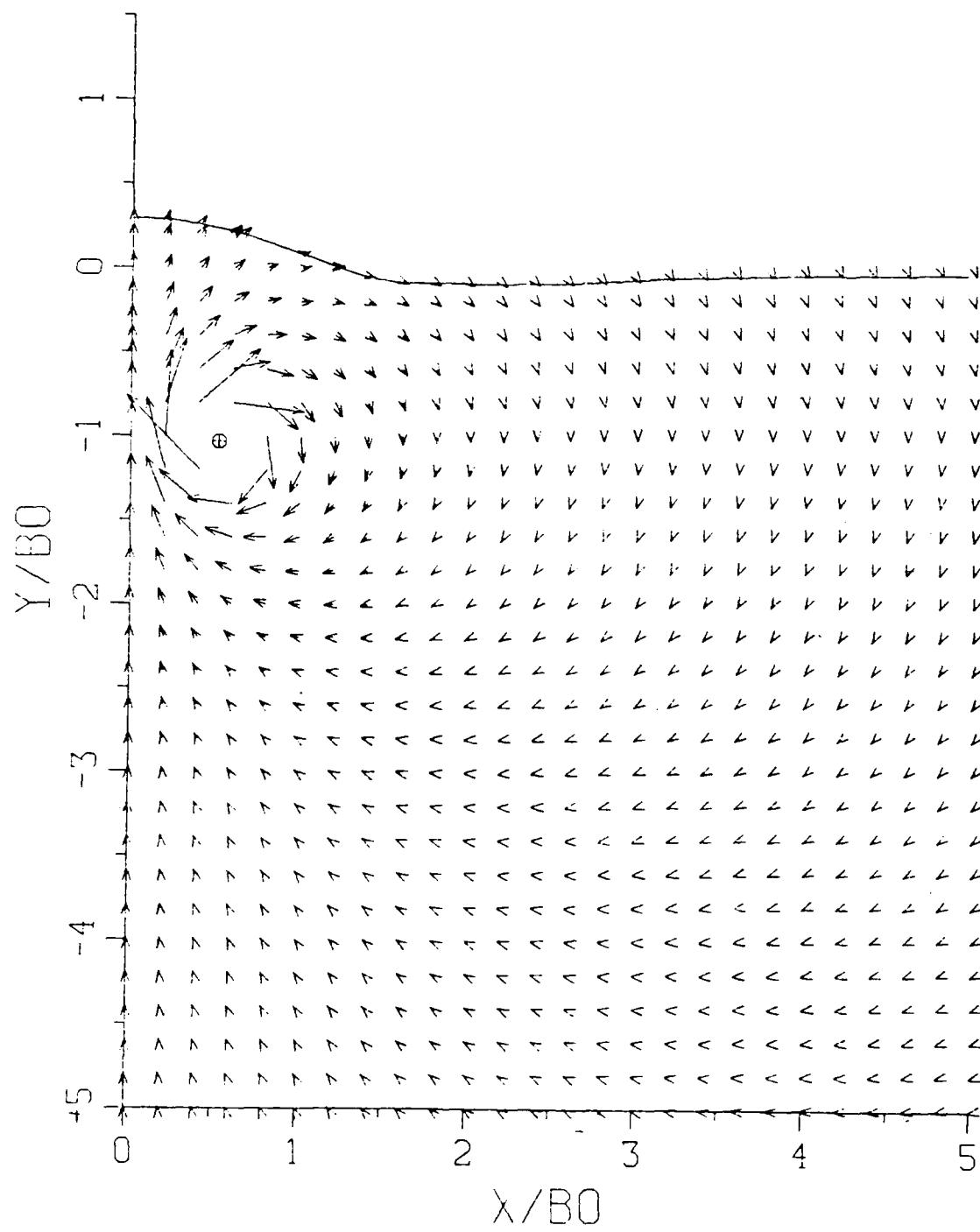
Figure 2.16 Velocity Field for T* = -0.90

$$T^* = -0.80000$$
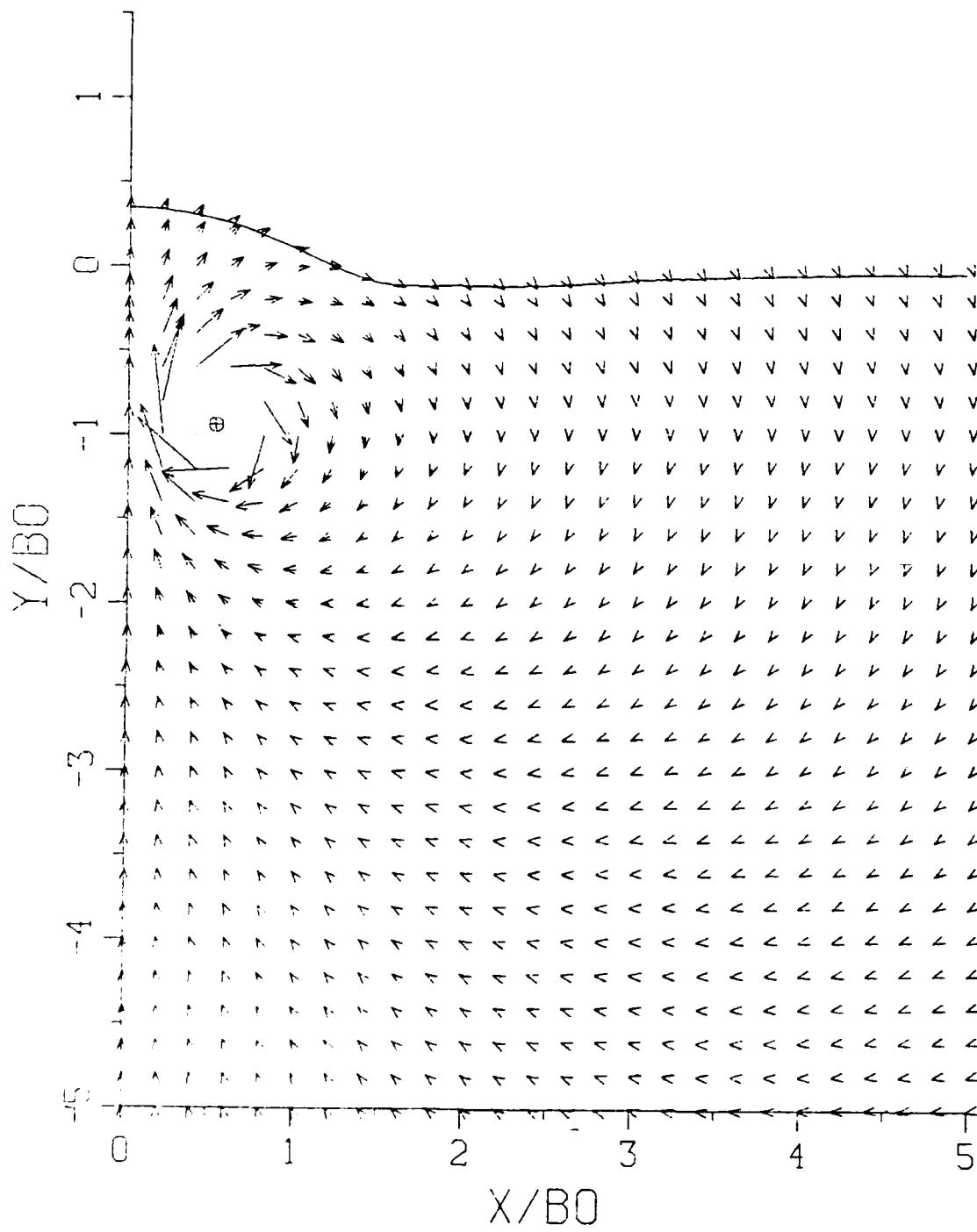
Figure 2.17 Velocity Field for T* = -0.80

$$T^* = -0.70000$$
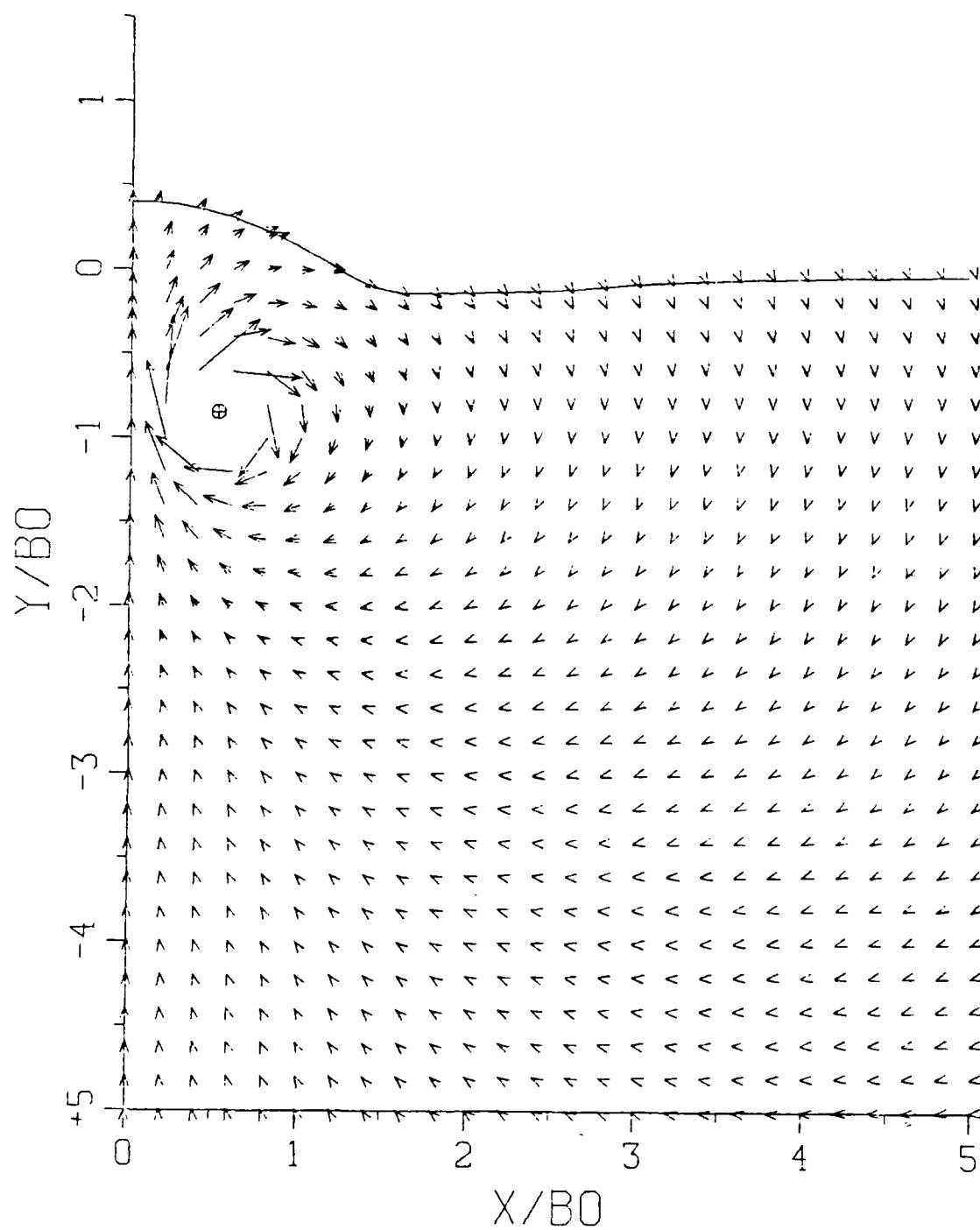
Figure 2.18 Velocity Field for T* = -0.70

84

$$T^* = -0.60000$$
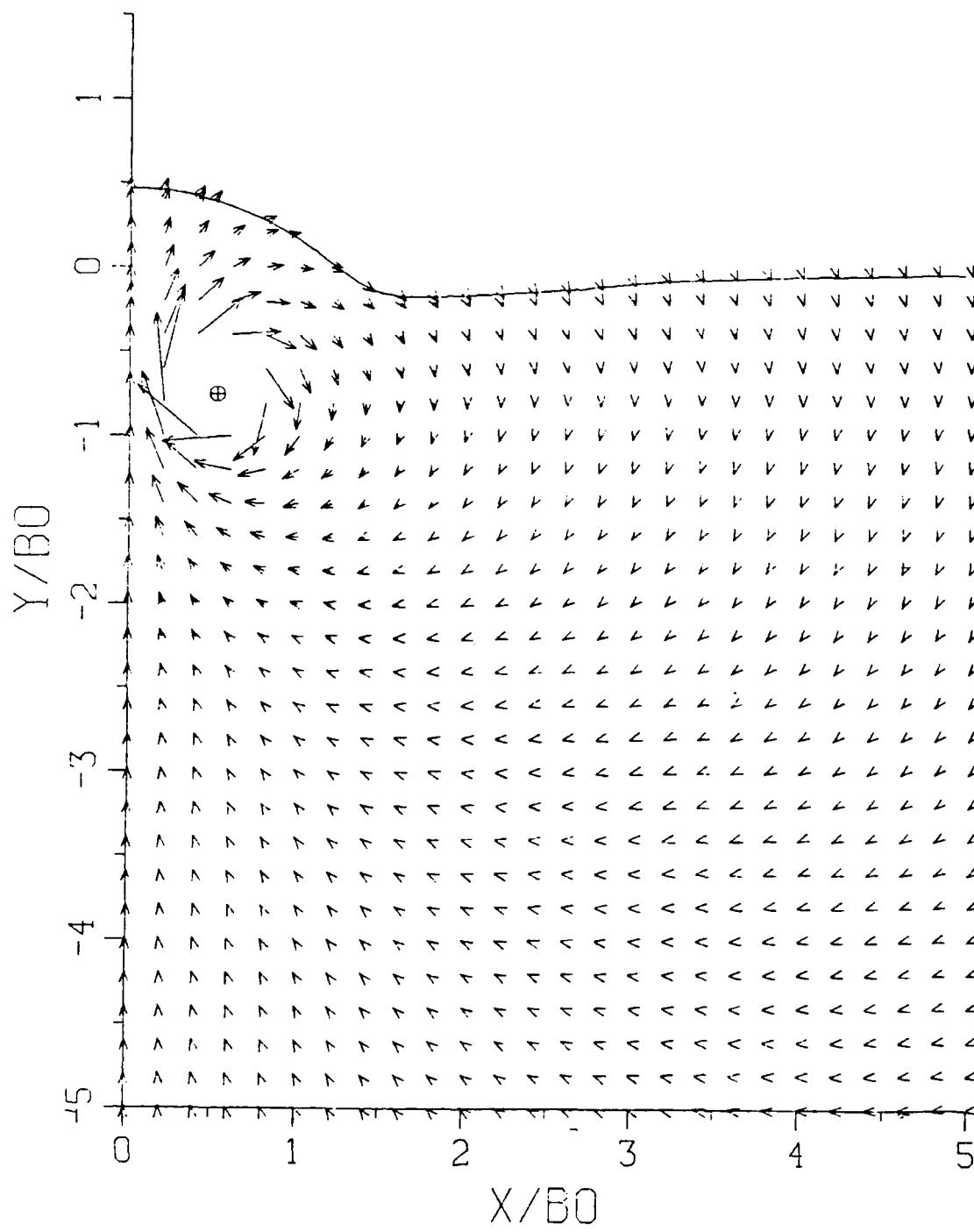
Figure 2.19 Velocity Field for T* = -0.60

$$T^* = -0.50000$$
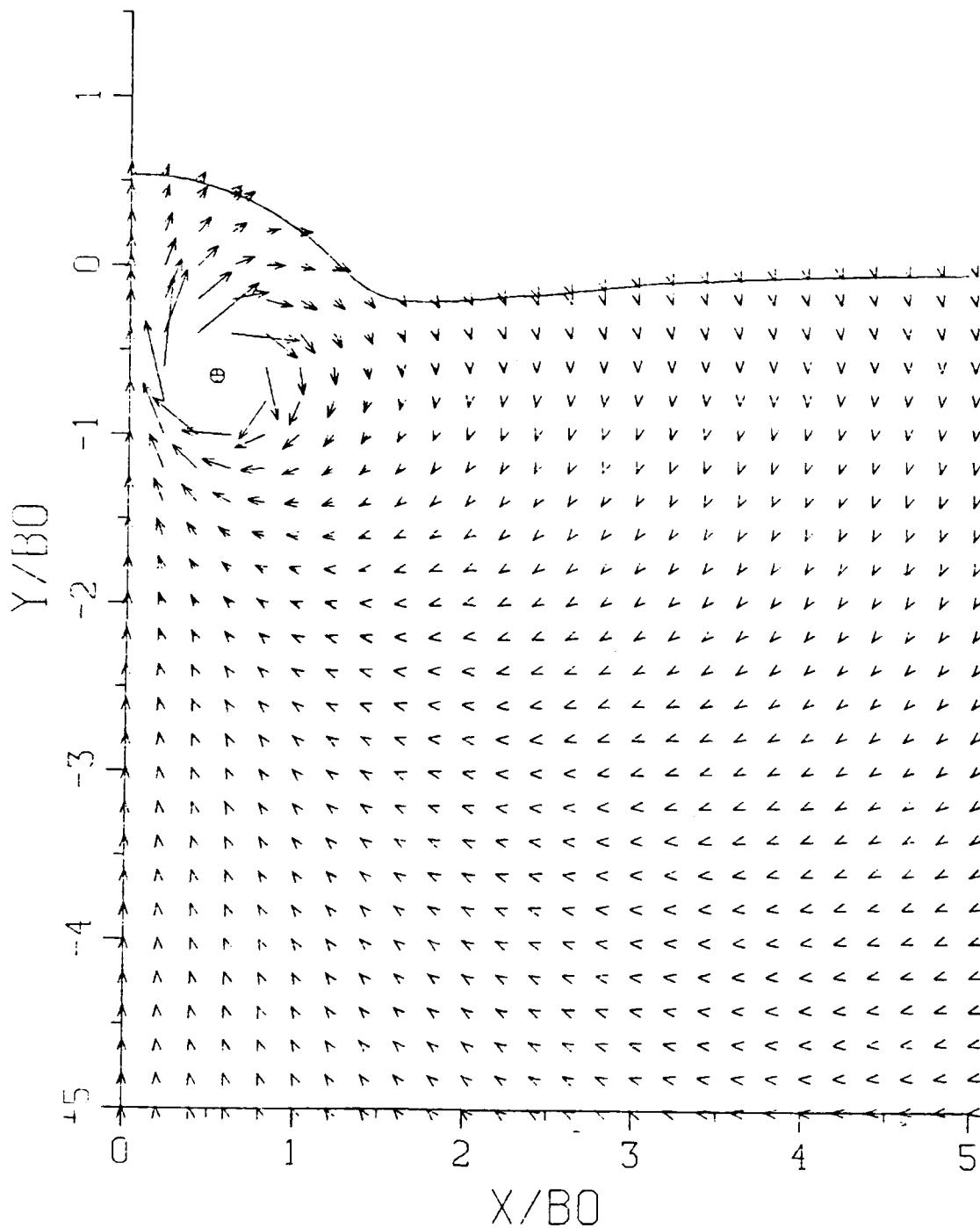
Figure 2.20 Velocity Field for T* = -0.50

$$T^{*} = -0.40000$$
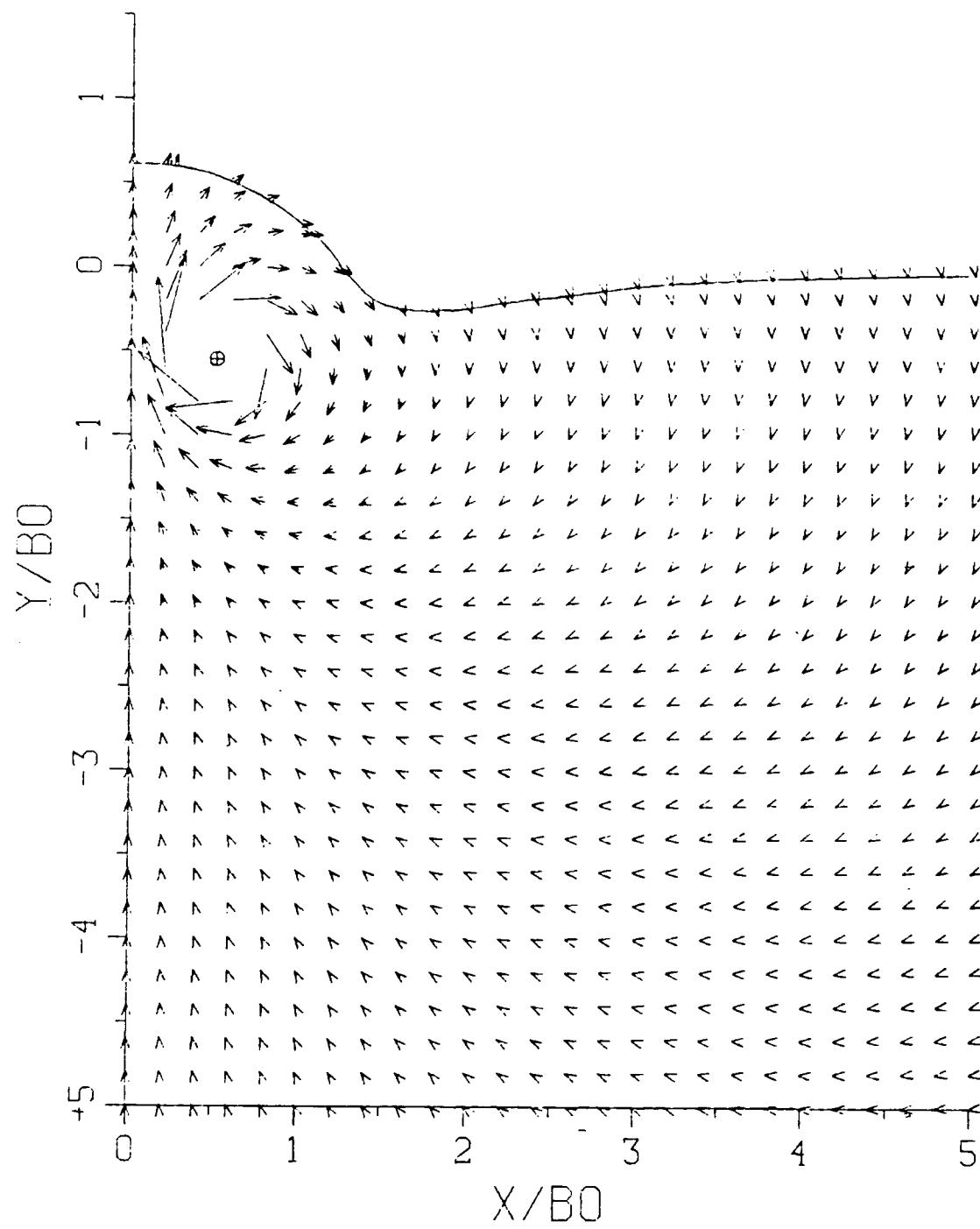
Figure 2.21 Velocity Field for T^{*} = -0.40

$$T^* = -0.30000$$
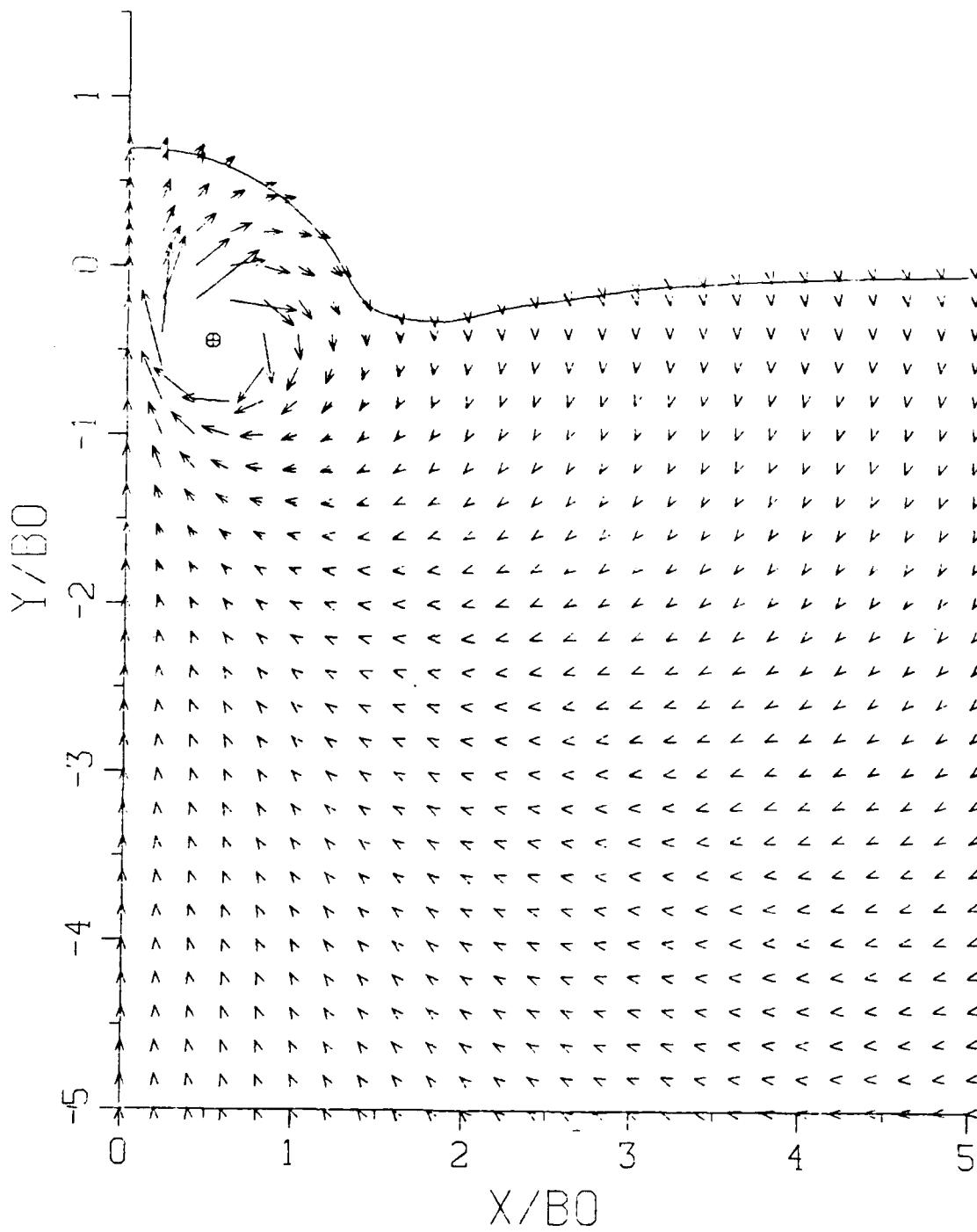
Figure 2.22 Velocity Field for $T^* = -0.30$

88
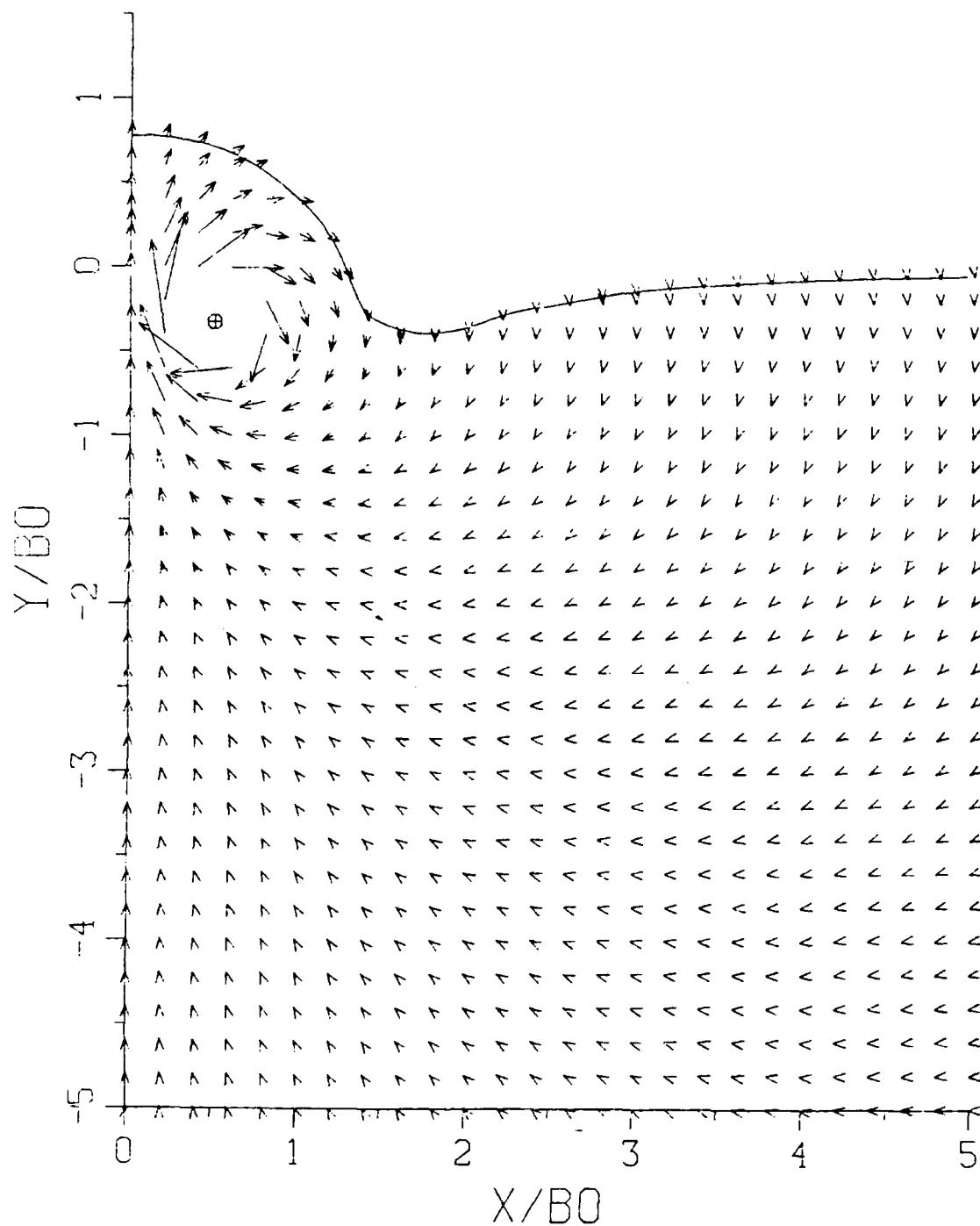
$$T^* = -0.20000$$

Figure 2.23 Velocity Field for $T^* = -0.20$

$$T^* = -0.10000$$
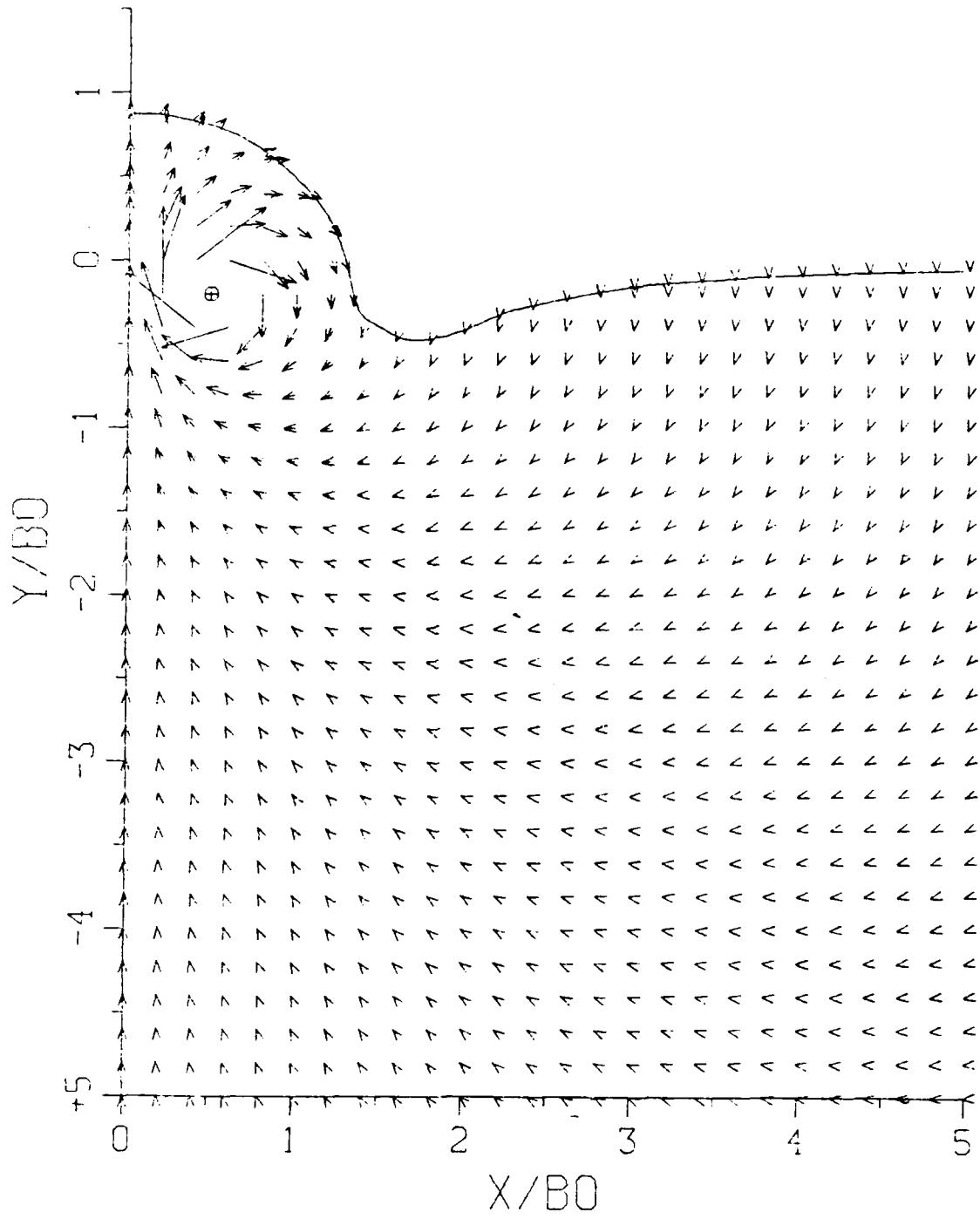
Figure 2.24 Velocity Field for $T^* = -0.10$

90

$$T^* = \quad 0.00000$$
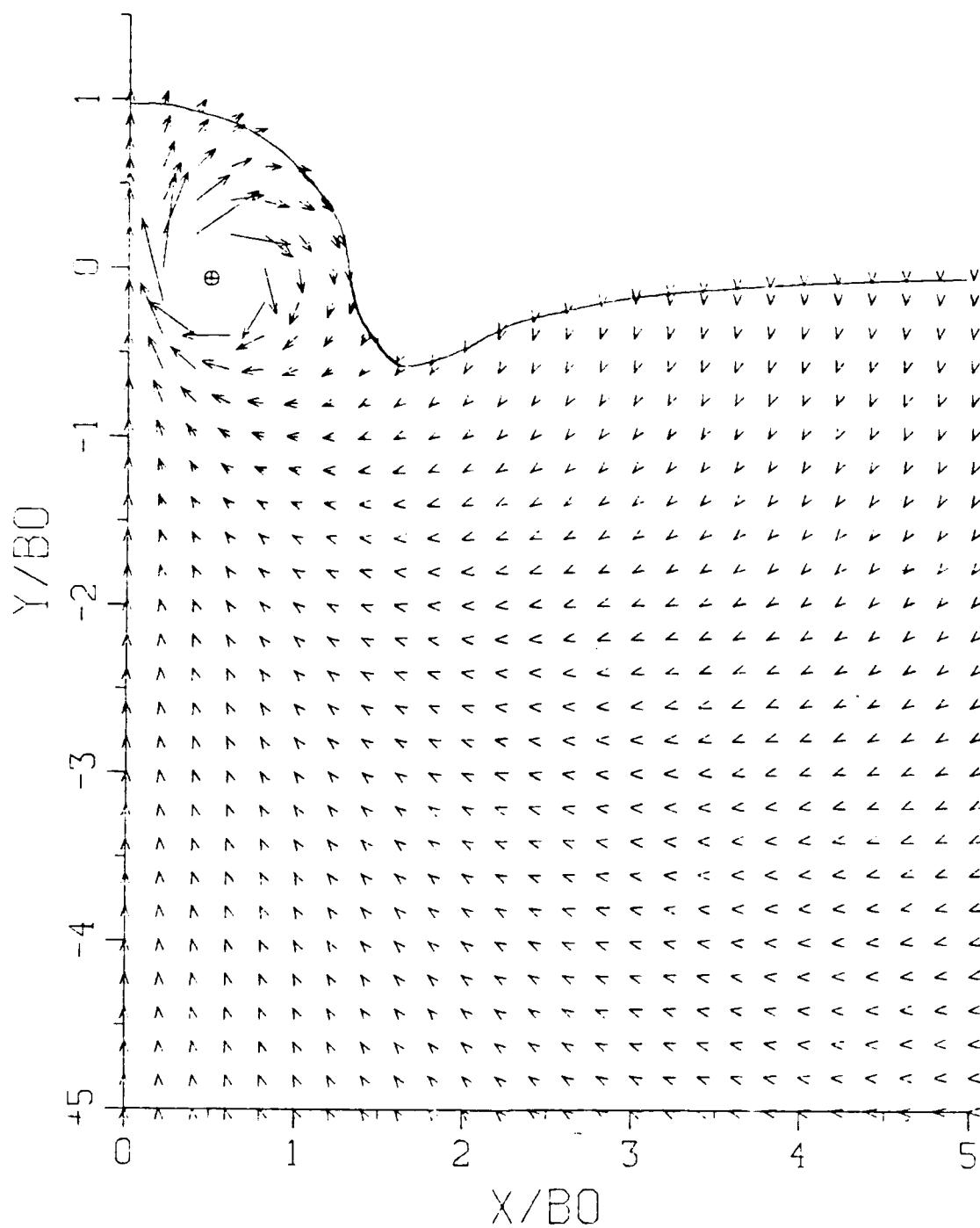
Figure 2.25 Velocity Field for T* = 0.00

91

$$T^* = \quad 0.10000$$
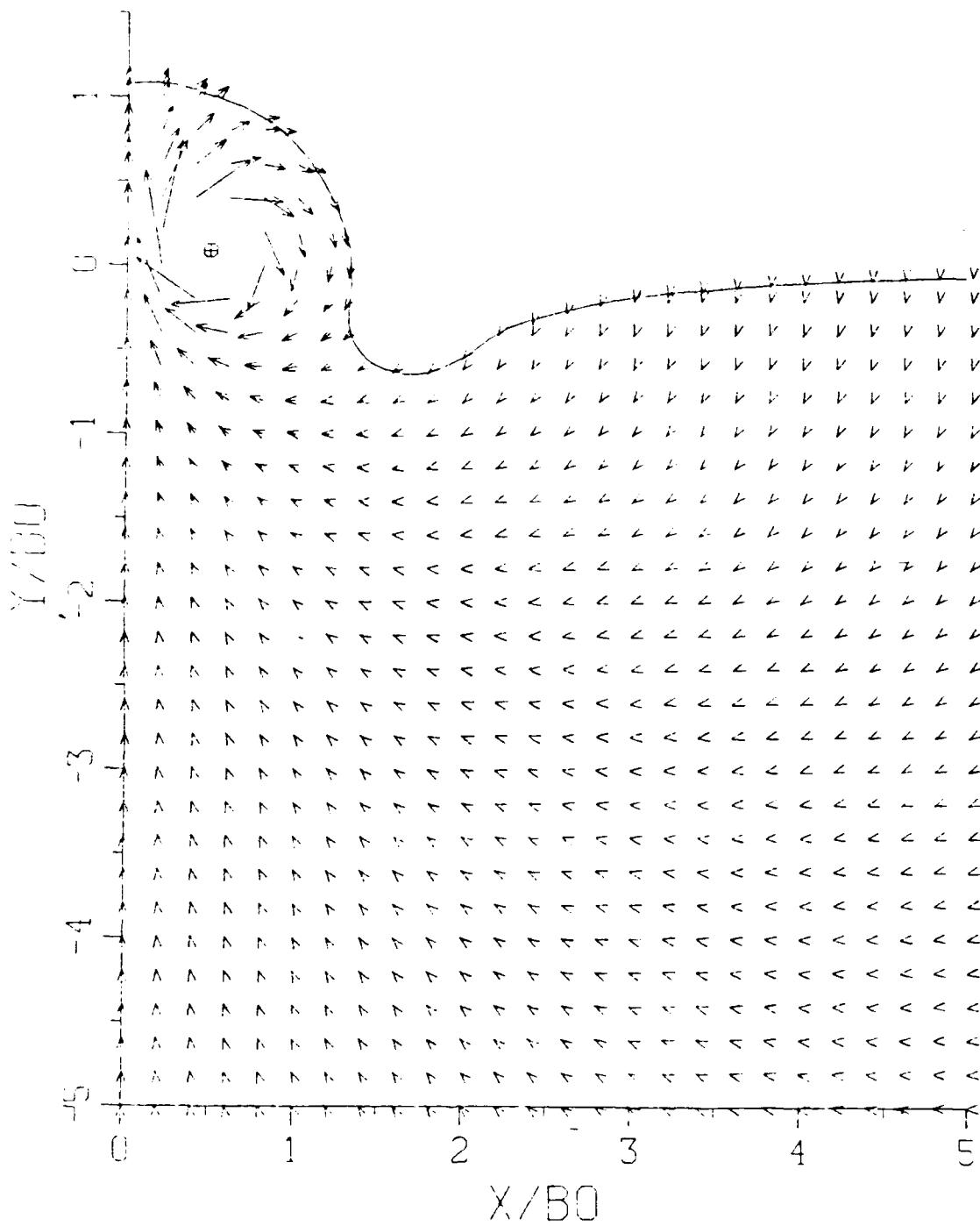
Figure 2.26   Velocity Field for $T^* = 0.10$

92
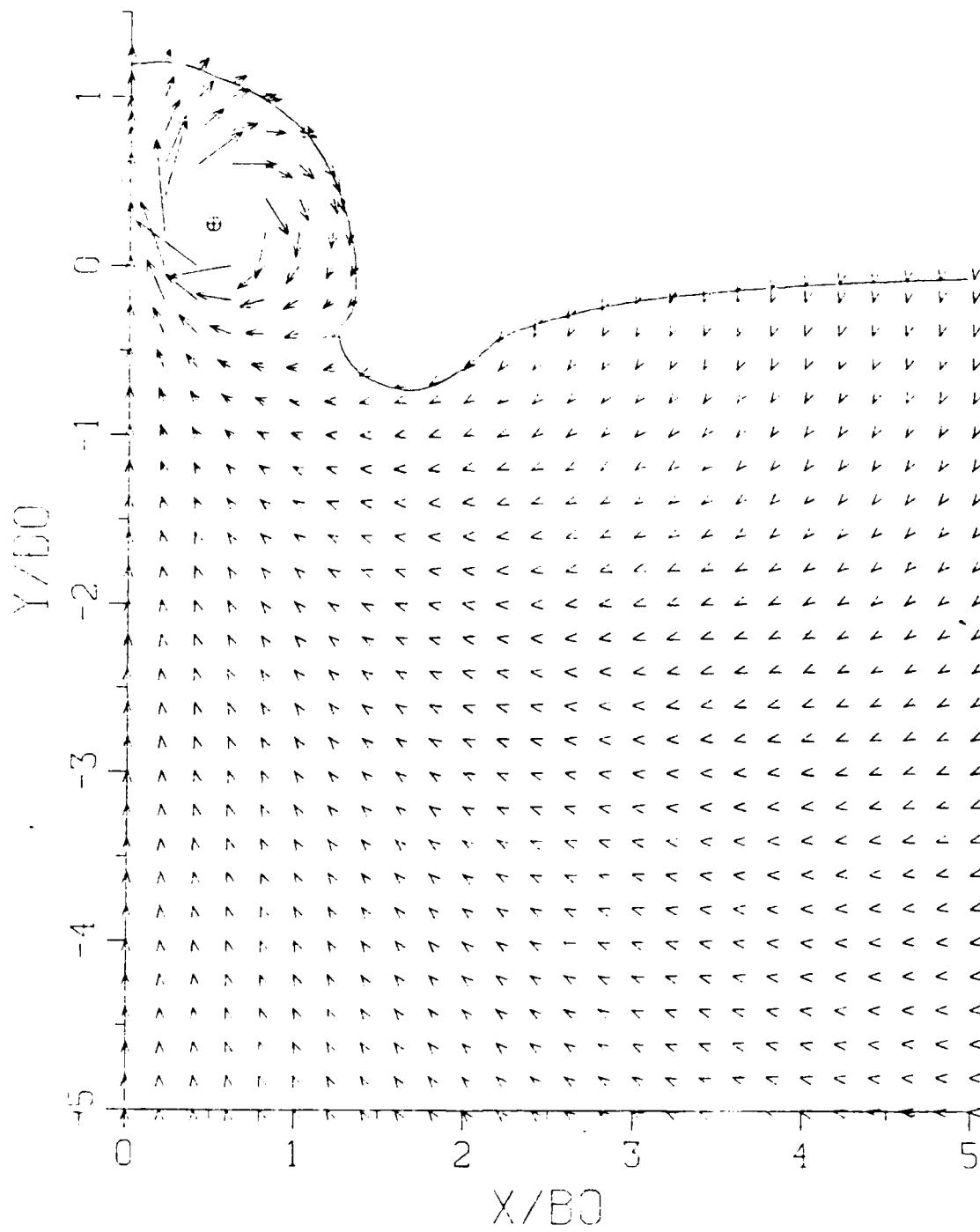
Figure 2.27 Velocity Field for T* = 0.20

93

SECT A

END VIEW

TOP VIEW

FRONT VIEW
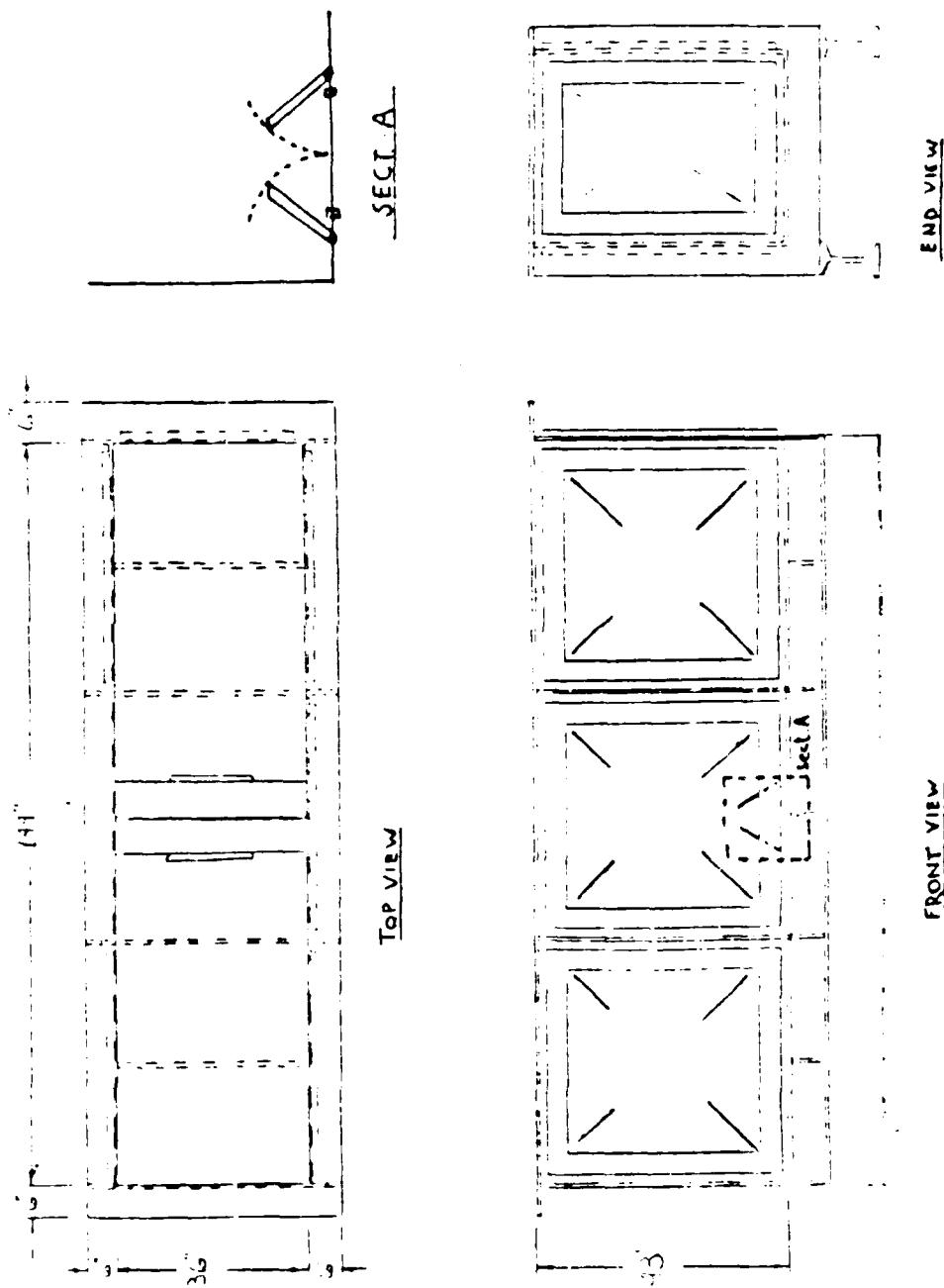
Figure 3.   Experimental Apparatus
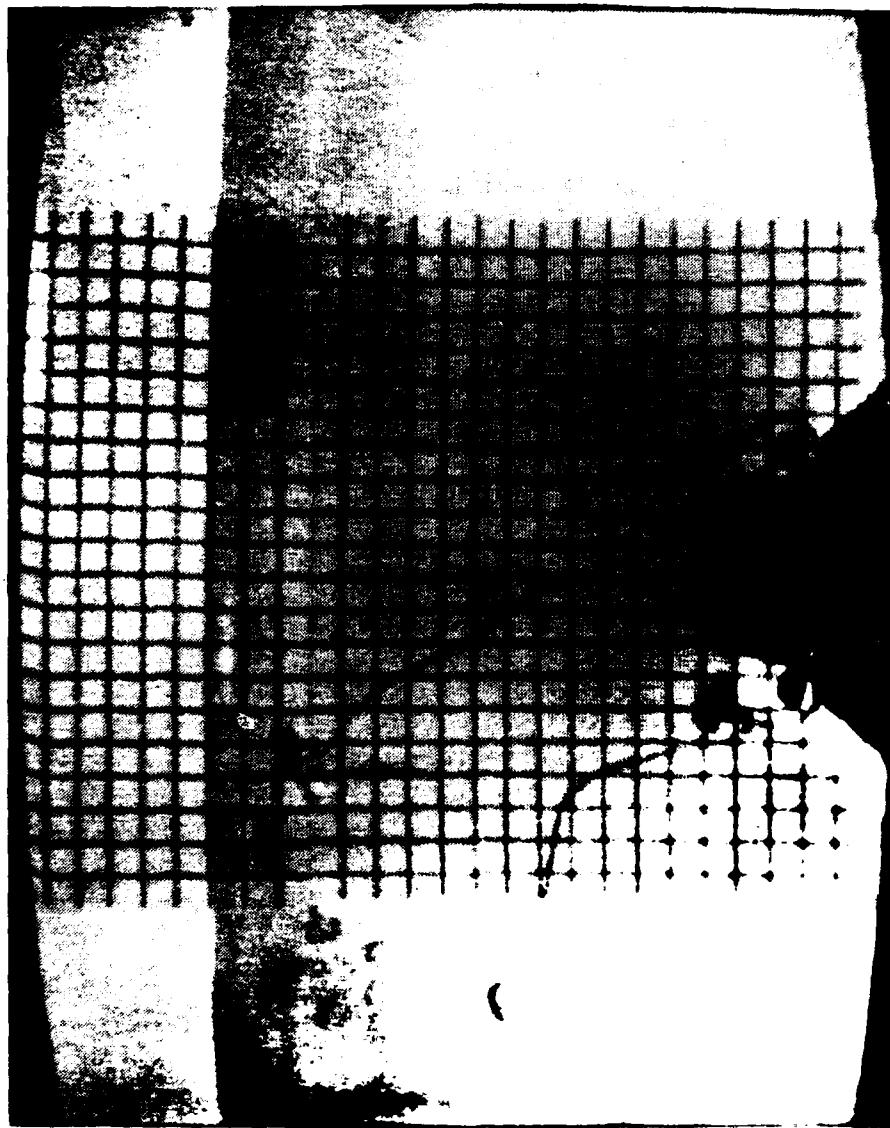
94
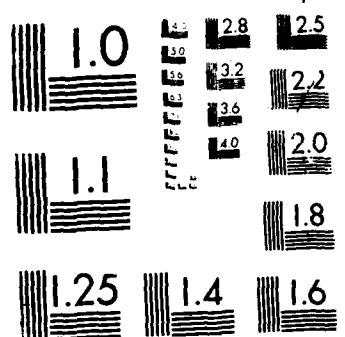
MICROCOPY RESOLUTION TEST CHART
NATIONAL BUREAU OF STANDARDS 1963
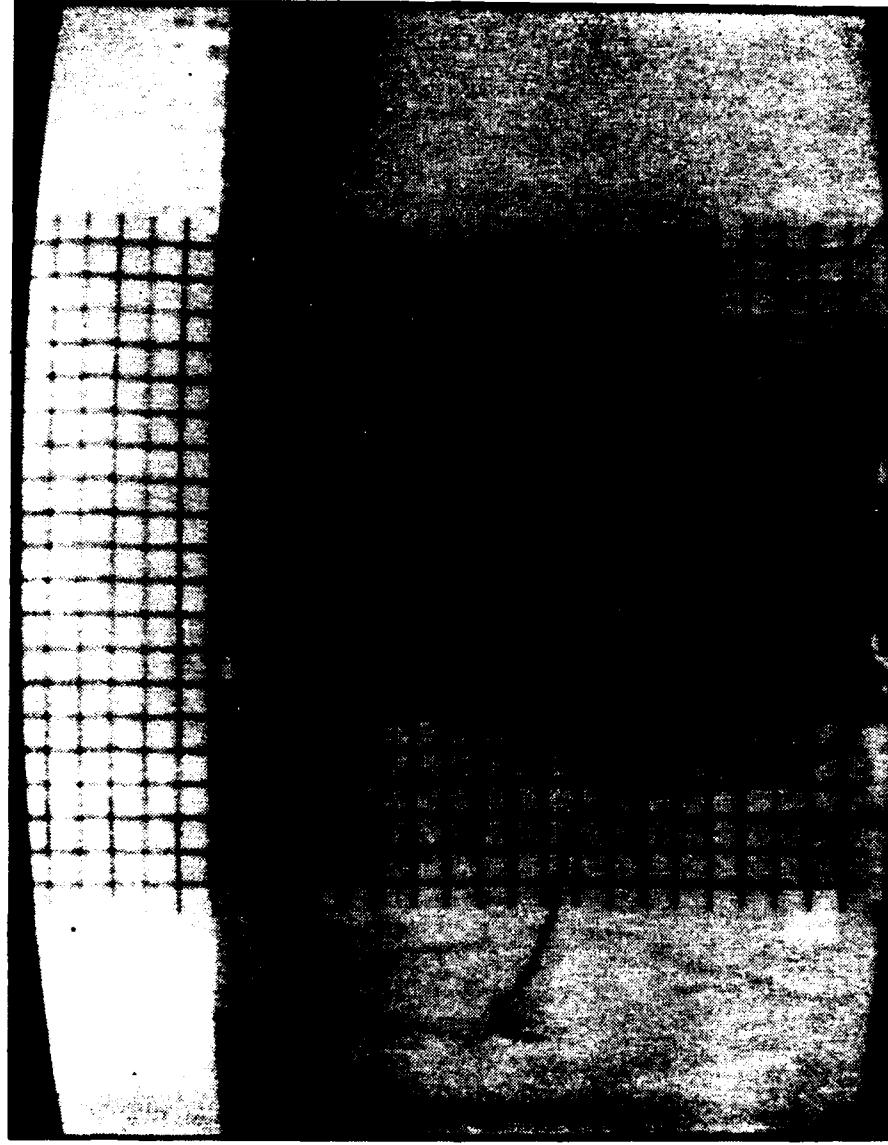
Figure 4.2   Vortex Motion at $T^* = -3.46$

Figure 4.3   Vortex Motion at T* = -3.00
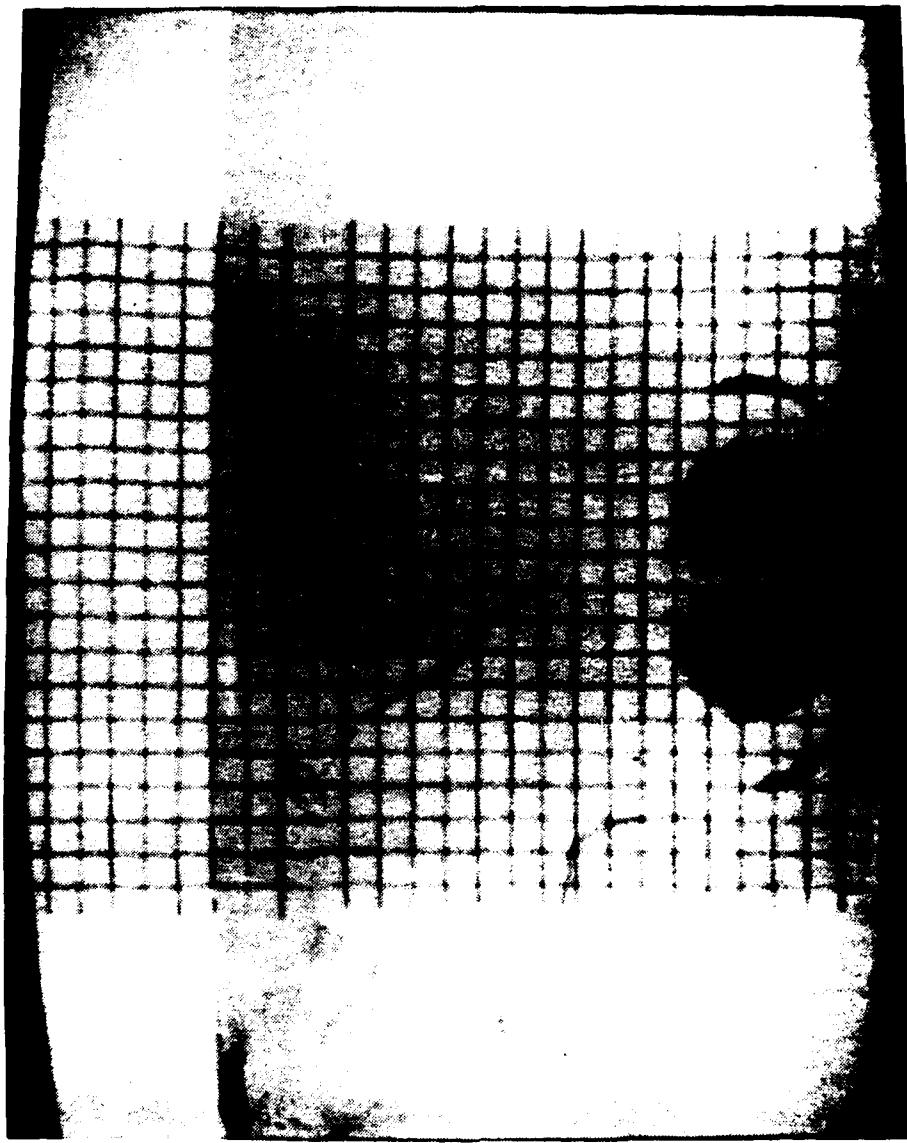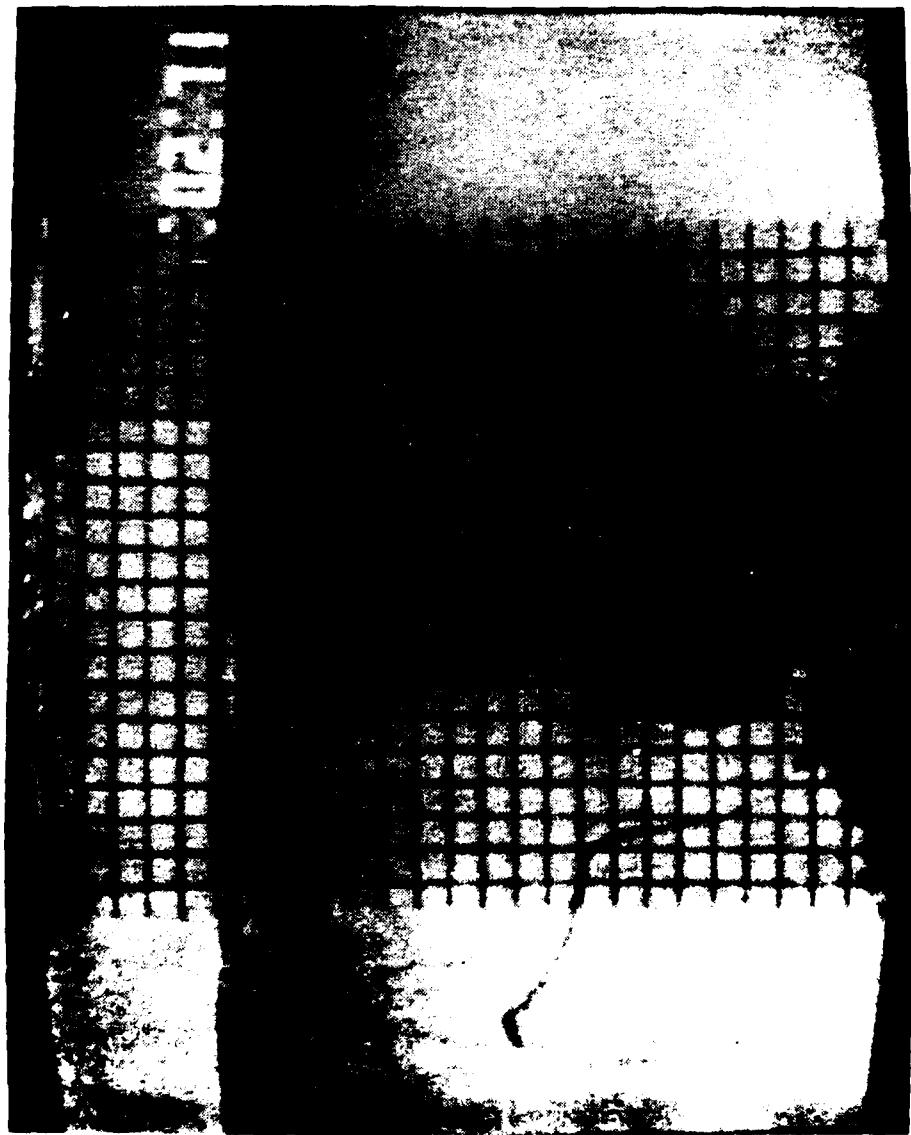
Figure 4.4   Vortex Motion at $\Gamma^* = -2.73$

Figure 4.5   Vortex Motion at $T^* = -1.63$
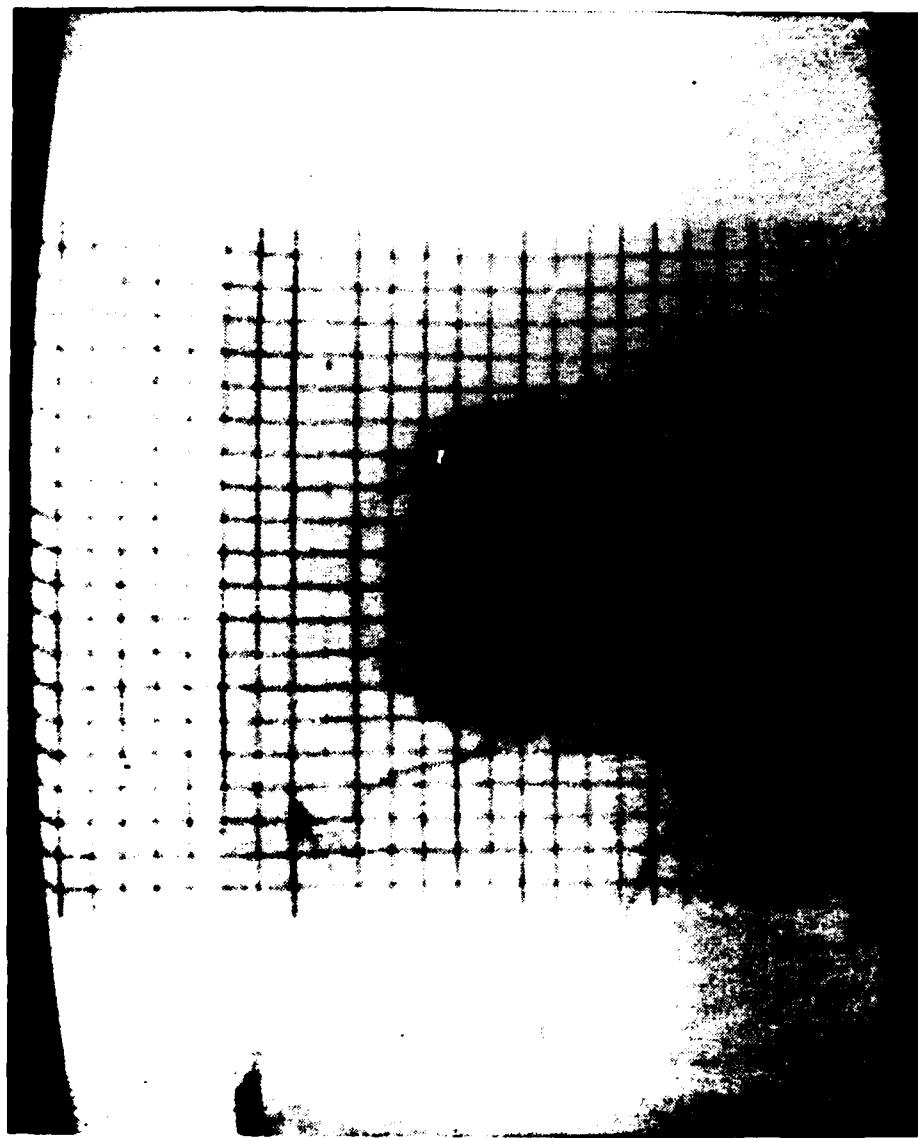
Figure 4.6   Vortex Motion at $T^* = -0.82$
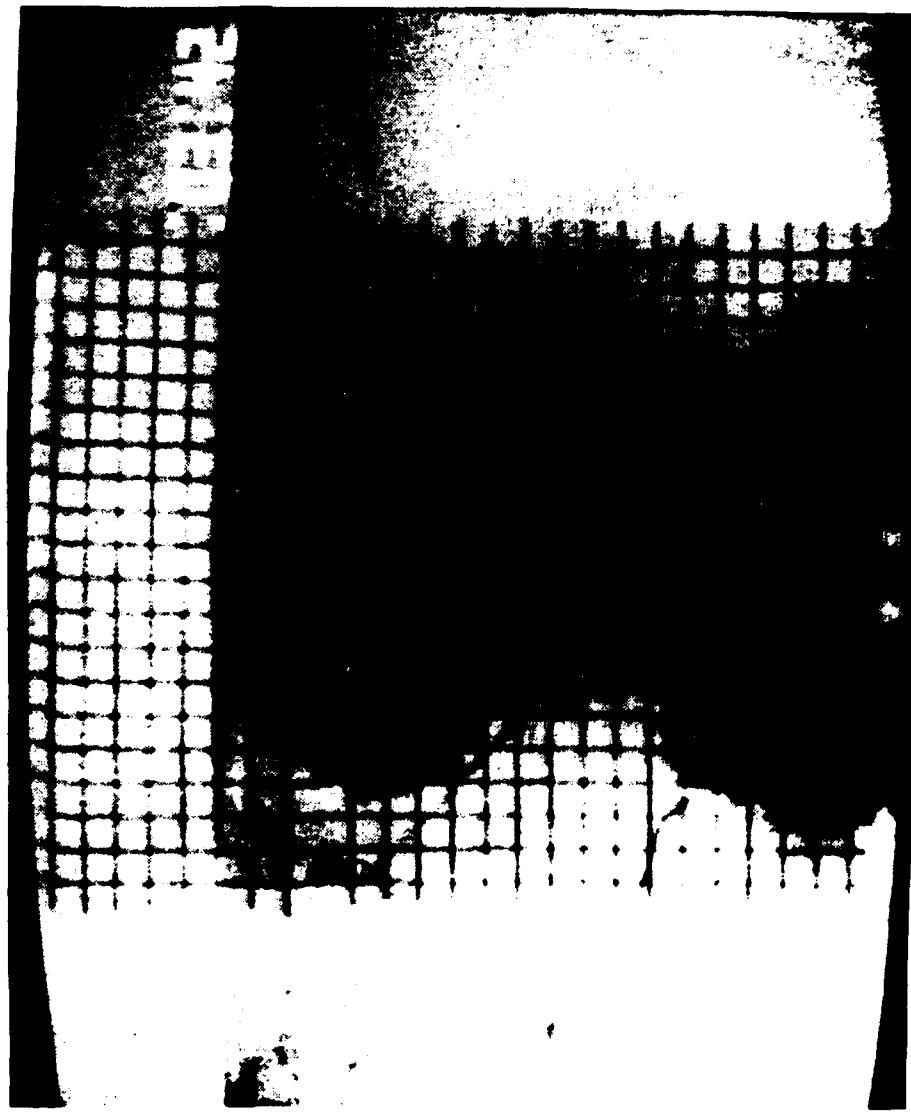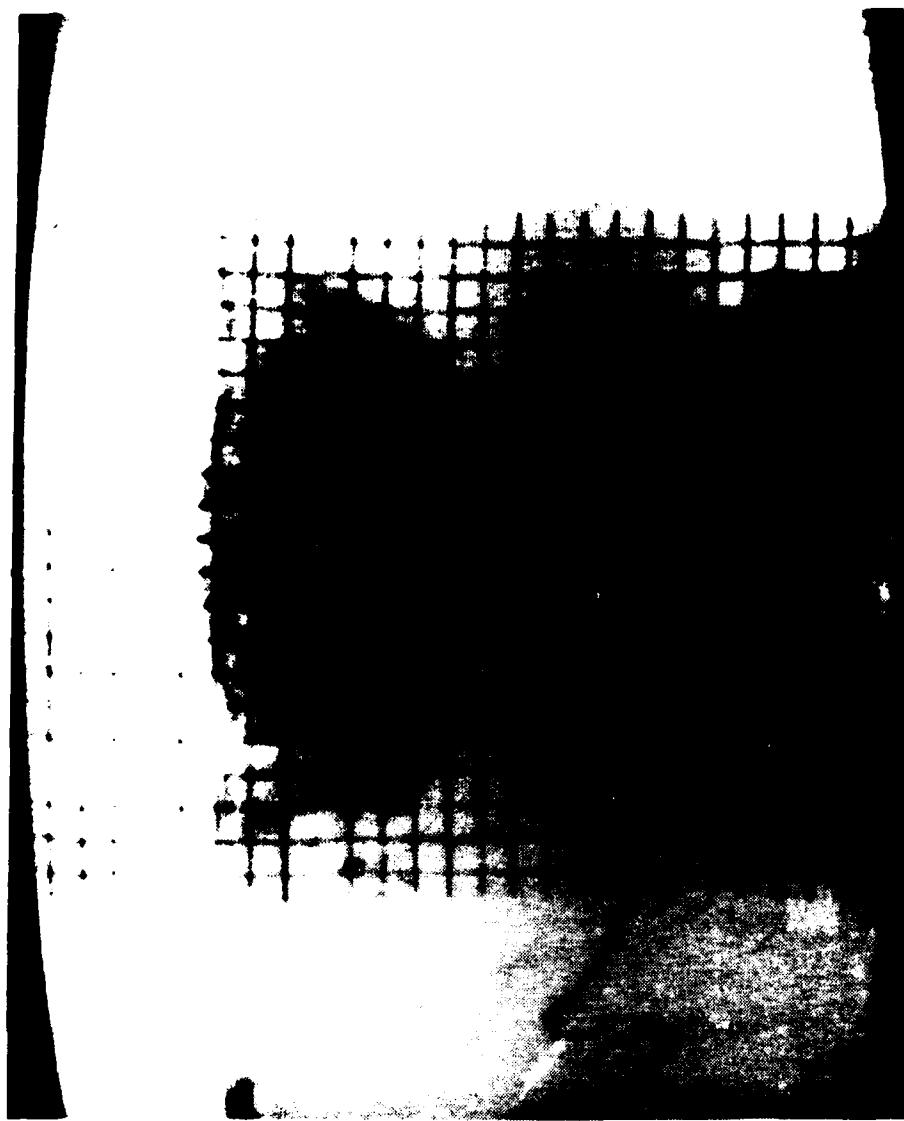
Figure 4.7   Vortex Motion at T* = -0.28
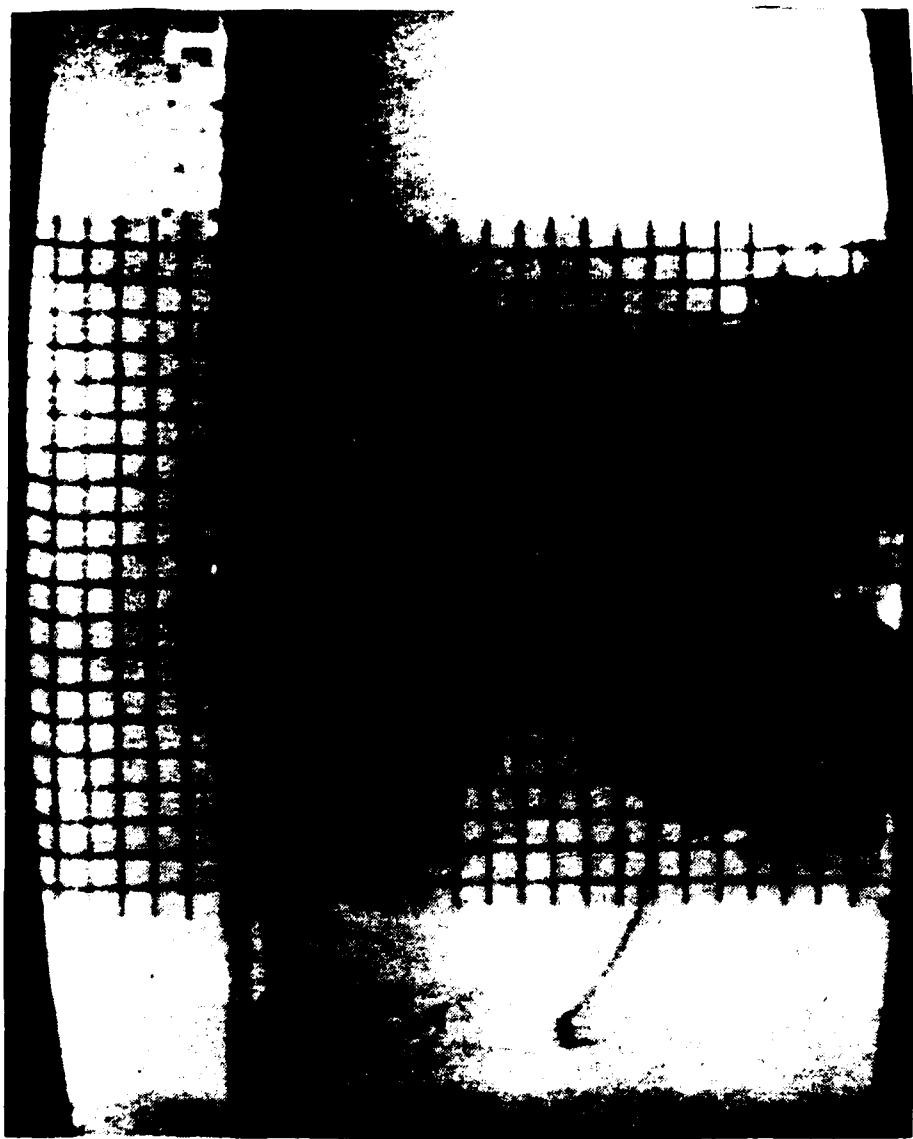
Figure 4.8   Vortex Motion at $T^* = -0.09$

Figure 4.9   Vortex Motion at $T^* = 0.09$
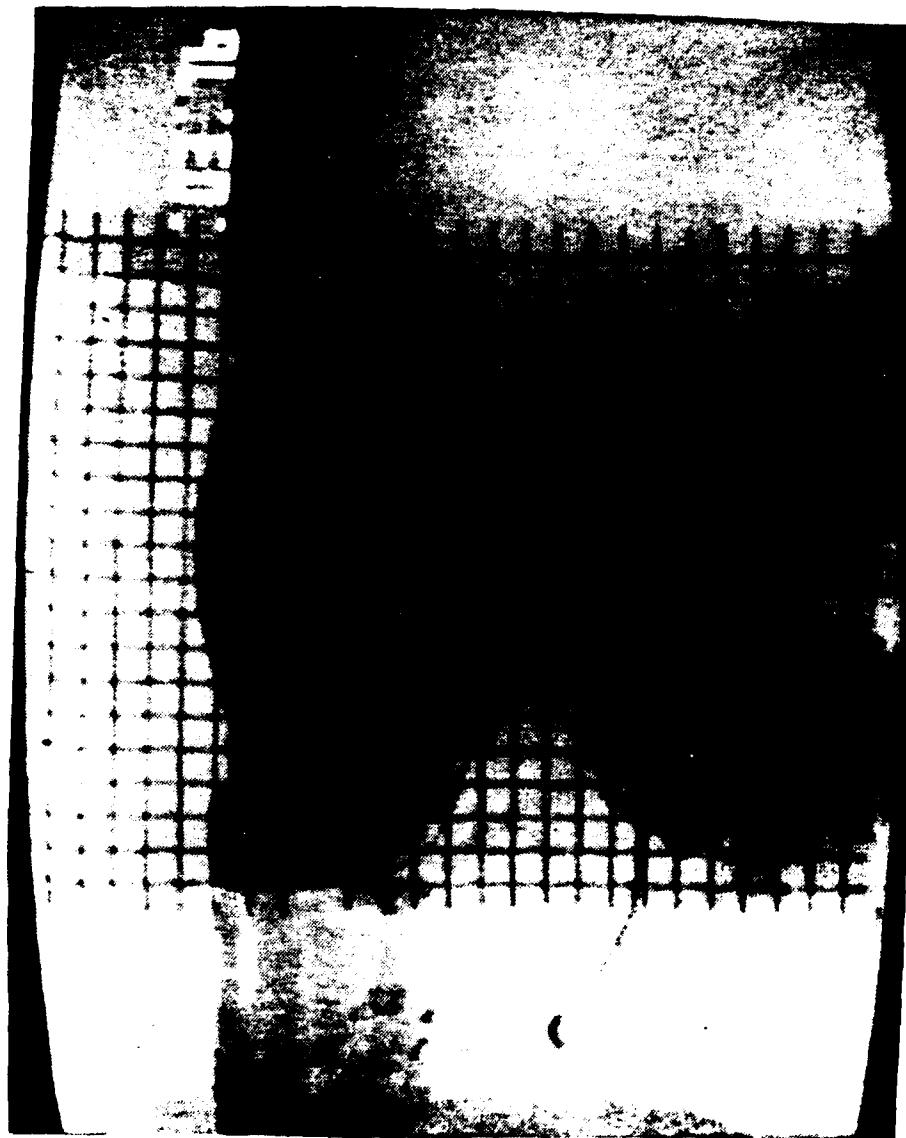
Figure 4.10 Vortex Motion at $T^* = 0.28$
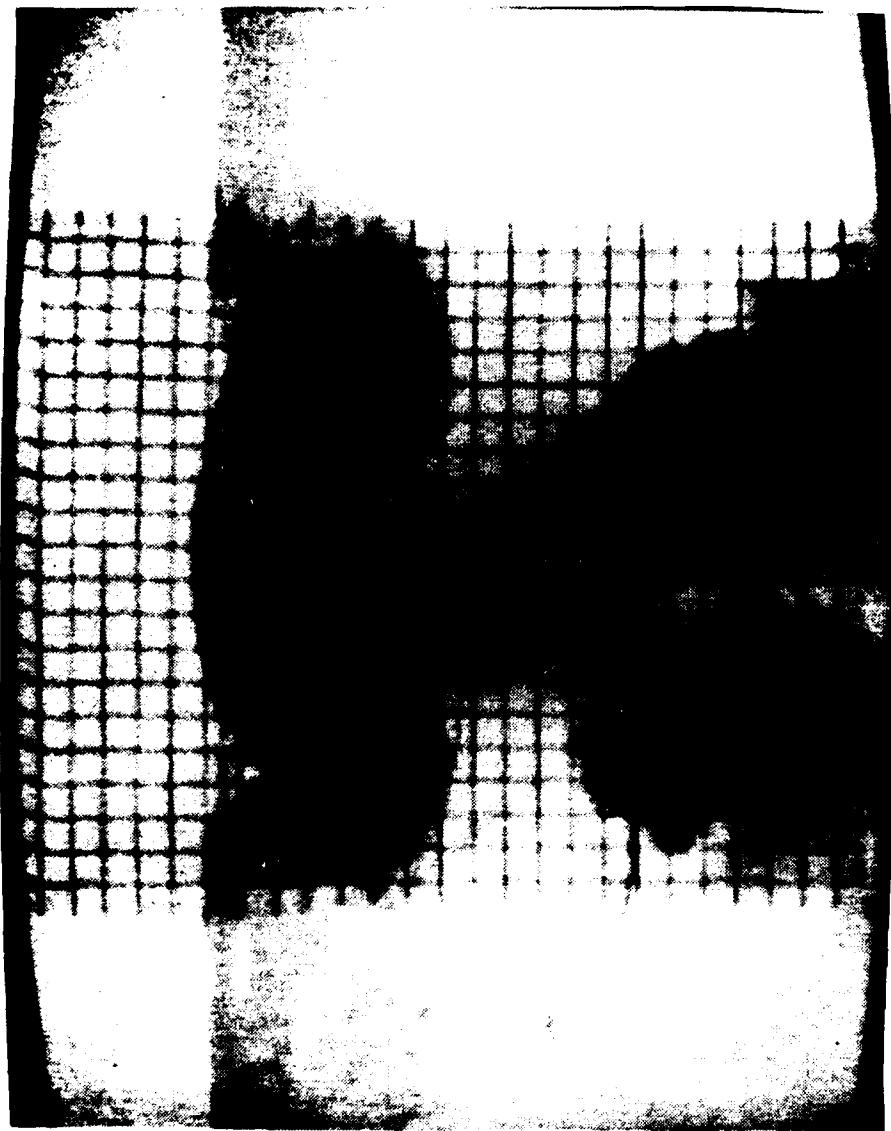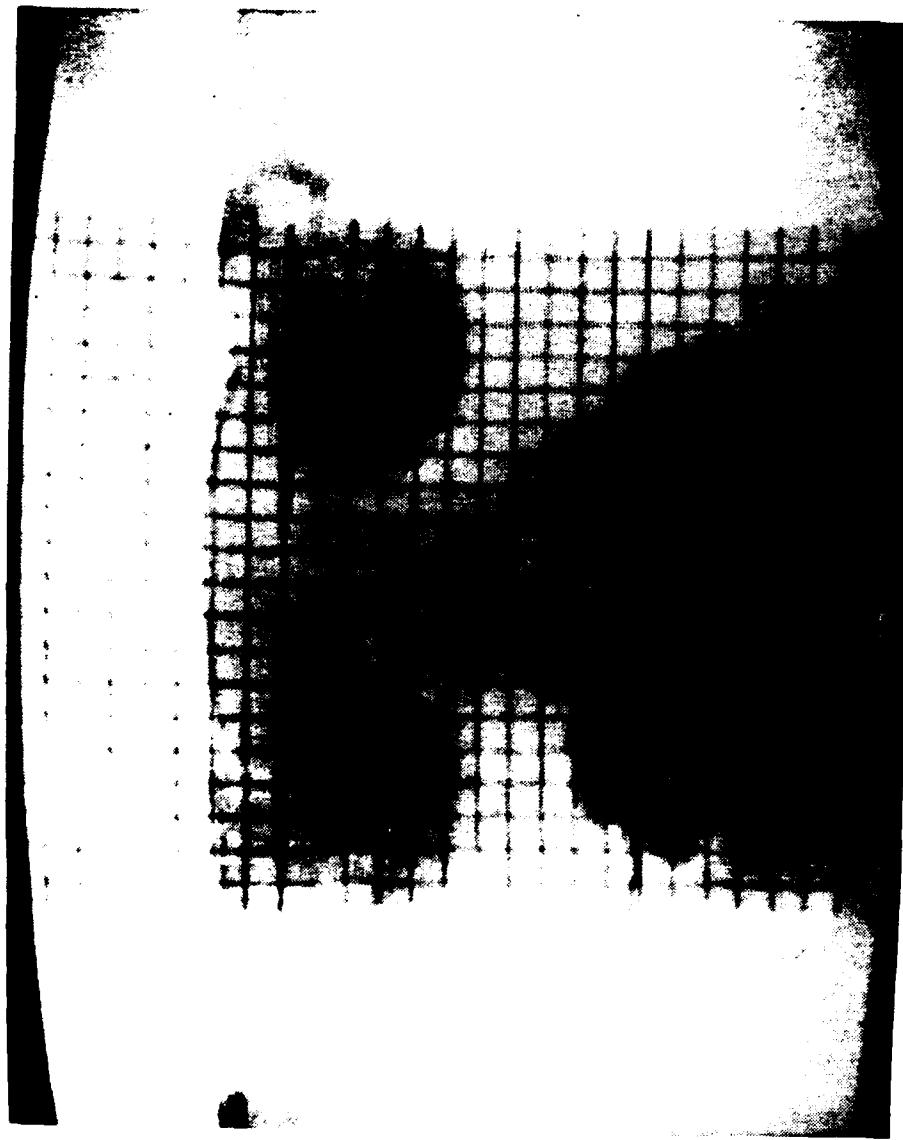
Figure 4.11 Vortex Motion at $T^* = 0.44$

Figure 4.12 Vortex Motion at T* = 0.82
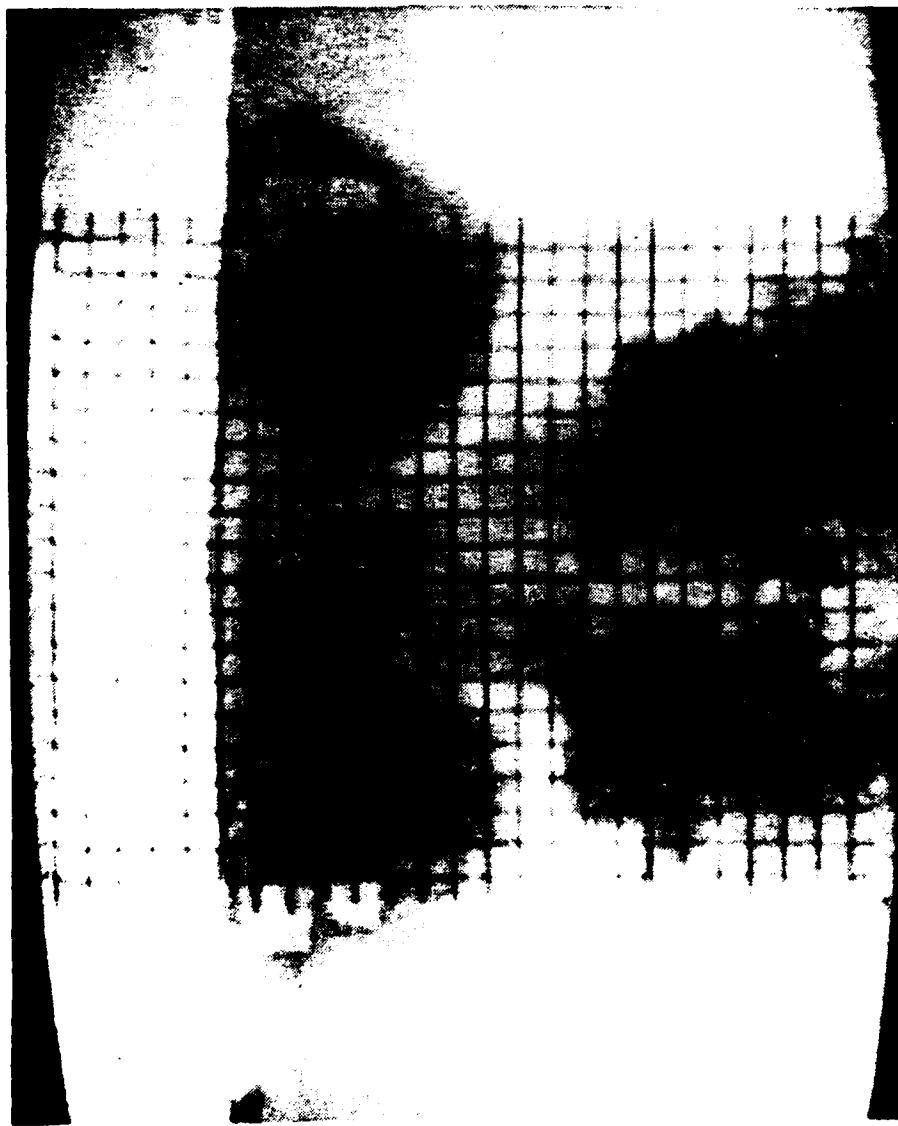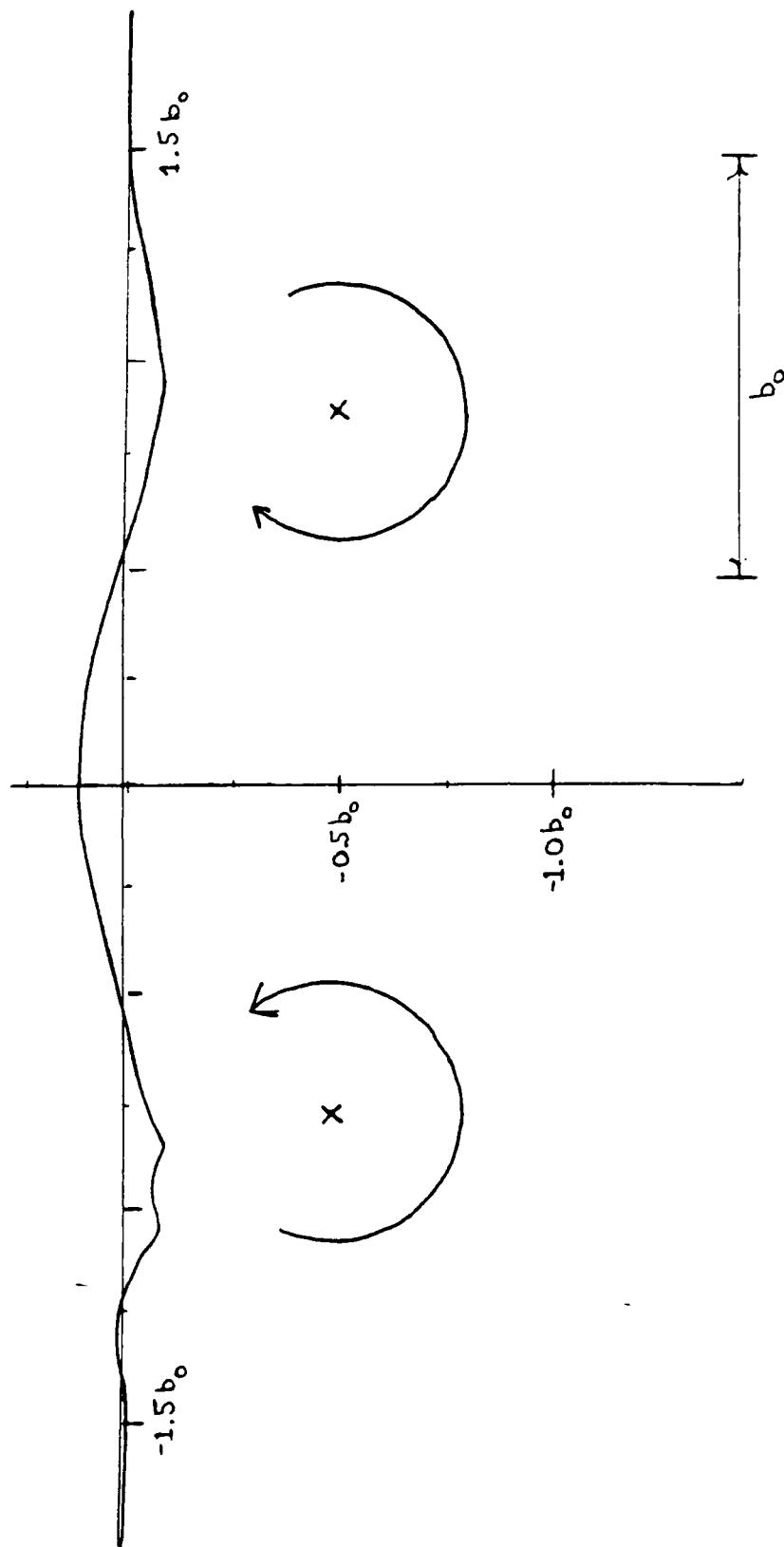
Figure 5. Free Surface Shape at Maximum Rise

LIST OF REFERENCES

1. Olsen, J. H., A. Goldburg, and M. Rogers, eds., Aircraft Wake Turbulence and Its Detection, Plenum Press, New York, 1971.

2. Hallock, J. N., ed., Proceedings of the Aircraft Wake Vortices Conference, 1977, National Technical Information Services, Springfield, VA 22161.

3. Donaldson, C. duP., and A. J. Bilanin, Vortex Wakes of Conventional Aircraft, AGARDograph AGARD-AG-204, 1975.

4. Widnall, S. E., "The Structure and Dynamics of Vortex Filaments," Annual Reviews of Fluid Mechanics, Vol. 7, 1975, pp. 141-165.

5. Hallock, J. N., and W. R. Eberle, eds., Aircraft wake Vortices A State-of-the-Art Review of the United States R&D Program, Transportation Systems Center, Cambridge, MA, Repot No. FAA-RD-77-23, 1977.

6. Sarpkaya, T., "Trailing Vortices in Homogeneous and Density-Stratified Media," Journal of Fluid Mechanics, Vol. 136, 1983, pp. 85-109.

7. Panton, R. L., W. L. Oberkampf, and N. Soskic, "Flight Measurements of a Wing Tip Vortex," Journal of Aircraft, Vol. 17, 1980, pp. 250-259.

8. Baker, G. R., S. J. Barker, K. K. Bofah, and P. G. Saffman, "Laser Anemometer Measurements of Trailing Vortices in Water," Journal of Fluid Mechanics, Vol. 65, pp. 325-336.

9. Crow, S. C., "Stability Theory for a Pair of Trailing Vortices," AIAA Journal, Vol. 8, 1970, pp. 2172-2179.

10. Tombach, I., "Observations of Atmospheric Effects on Vortex Wake Behaviors," Journal of Aircraft, Vol. 10, 1973, pp. G41-G47.

11. Peace, A. J., and N. Riley, "A Viscous Vortex Pair in Ground Effect," Journal of Fluid Mechanics, Vol. 129, 1983, pp. 409-426.

12. Barker, S. J., and S. C. Crow, "The Motion of a Two-Dimensional Vortex Pair in Ground Effect," Journal of Fluid Mechanics, Vol. 82, 1977, pp. 659-671.

13. Tombach, I. H., "Transport of a Vortex Wake in a Stably Stratified Atmosphere," Aircraft Wake Turbulence and Its Detection, ed. J. H. Olsen, et al., Plenum Press, New York, 1971, pp. 41-57.

14. Naval Postgraduate School, Monterey, CA, NPS-69-82-003, Trailing Vortices in Stratified Fluids, by T. Sarpkaya and S. K. Johnson, June 1982.

15. Johnson, S. K., Trailing Vortices in Stratified Fluids, M.S. Thesis, Naval Postgraduate School, Monterey, CA, June 1982.

16. Turkmen, C., Trailing Vortices in Stratified and Unstratified Fluids, M.S. Thesis, Naval Postgraduate School, Monterey, CA, December 1982.

17. Gray, W. E., Scars on Striations Due to Trailing Vortices, M.S. Thesis, Naval Postgraduate School, Monterey, CA, March 1985.

18. Daly, J. J., Effects of Ambient Turbulence and Stratification on the Demise of Trailing Vortices, M.S. Thesis, Naval Postgraduate School, Monterey, CA, March 1986.

19. Noble, W. D., Characteristics of Vortices in Stratified Media, M.S. Thesis, Naval Postgraduate School, Monterey, CA, September 1986.

20. Miller, B. S. L., Vortex Motion in a Stratified Medium, M.S. Thesis, Naval Postgraduate School, Monterey, CA, December 1986.

21. Striftos, C., Vortex Motion in Stratified Fluids, M.S. Thesis, Naval Postgraduate School, Monterey, CA, March 1982.

22. Sarpkaya, T., and P. O. Henderson, Free Surface Scars and Striations due to Trailing Vortices Generated by a Submerged Lifting Surface, AIAA Paper No. AIAA-85-0445, January 1985.

23. Sarpkaya, T., and M. Issacson, Mechanics of Wave Forces on Offshore Structures, Van Nostrand Reinhold Company, 1981, pp. 21-22.

24. Haussling, H. J., and R. M. Coleman, "Nonlinear Water Waves Generated by an Accelerated Circular Cylinder," Journal of Fluid Mechanics, Vol. 92, 1979, pp. 767-781.

25. Yeung, R. W., "Numerical Methods in Free Surface Flows," Annual Review of Fluid Mechanics, 1982, pp. 395-442.

26. Brandt, A., J. E. Dendy, and H. Ruppel, "The Multigrid Method for Semi-Implicit Hydrodynamic Codes," Journal of Computational Physics, Vol. 34, 1980, pp. 348-370.

27. Theodossiou, V. M., and A. C. M. Sousa, "An Efficient Algorithm for Solving the Incompressible Fluid Flow Equations," International Journal for Numerical Methods in Fluids, Vol. 6, 1986.

28. Ohring, S., "A Fast Fourth-Order Laplace Solver for Application to Numerical Three-Dimensional Water Wave Problems," Proceedings of the First International Conference on Numerical Ship Hydrodynamics, Gathersburg, MD, 1975, pp. 641-663.

29. Ohring, S., and J. Telste, "Numerical Solution of Transient Three-Dimensional Ship-Wave Problems," Proceedings of the Second International Conference on Numerical Ship Hydrodynamics, Berkeley, CA, 1977, pp. 88-103.

30. Zienkiewicz, O. C., The Finite Element Method in Engineering, McGraw-Hill, Third Edition, 1977.

31. Dhatt, G., and G. Touzot, The Finite Element Method Displayed, John Wiley, 1977.

32. Hiriart, G. L., A Theoretical Analysis of Jet Deflection From Plane and Axisymmetric Curved Obstacles, Ph.D. Thesis, Naval Postgraduate School, Monterey, CA, December 1983.

33. Larock, B. E., and C. Taylor, "Computing Three-Dimensional Free Surface Flows," International Journal for Numerical Methods in Engineering, Vol. 10, 1976, pp. 1143-1152.

34. Bai, K. J., and R. W. Yeung, "Numerical Solutions to Free-Surface Flow Problems," Tenth Symposium Naval Hydrodynamics, Cambridge, MA, pp. 609-647.

35. Brebbia, C. A., The Boundary Element Method for Engineers, John Wiley and Sons, 1978.

36. Hunt, B., "The Mathematical Basis and Numerical Principles of the Boundary Integral Method for Incompressible Potential Flow over 3-D Aerodynamic Configurations," Conference on Numerical Methods in Applied Fluid Dynamics, Academic Press, 1980.

37. Longuet-Higgins, M. S., and E. D. Cokelet, "The Deformation of Steep Surface Waves on Water," Proceedings of the Royal Society of London, Vol. 350, 1976, pp. 1-26.

38. Faltinsen, O. M., "Numerical Solutions of Transient Nonlinear Free Surface Motion Outside or Inside Moving Bodies," <u>Proceedings of the Second International Conference on Numerical Ship Hydrodynamics</u>, Berkeley, CA, 1977, pp. 347-357.

39. Chang, M.S., and P. C. Pien, "Hydrodynamic Forces on a Body Moving Beneath a Free Surface," <u>Proceedings of the First International Conference on Numerical Ship Hydrodynamics</u>, Gathersburg, MD, 1975, pp. 530-560.

40. Fink, P.T., and W. K. Soh, "Calculation of Vortex Sheets in Unsteady Flow and Applications in Ship Hydrodynamics," <u>Tenth Symposium Naval Hydrodynamics</u>, Cambridge, MA, 1974.

41. Sarpkaya, T., and R. L. Shoaff, "Inviscid Model of Two-Dimensional Vortex Shedding by a Circular Cylinder," <u>AIAA Journal</u>, Vol. 17, No. 11, 1979, pp. 1193-1200.

INITIAL DISTRIBUTION LIST

END
DATE
FILMED

JAN

1988